Aerodynamics and near-field acoustics of a subsonic cylindrical cavity flow by parallel CFD

Marco Grottadaurea

Department of Engineering

University of Leicester

A thesis submitted for the degree of

Doctor of Philosophy

December 2009

Aerodynamics and near-field acoustics of a subsonic cylindrical cavity flow by parallel CFD

Marco Grottadaurea

Department of Engineering
University of Leicester

A thesis submitted for the degree of
Doctor of Philosophy

December 2009

Two cylindrical cavities of diameter to depth ratio $L/D = 0.71$ and $L/D = 2.5$ were investigated by numerical modelling. The flow was modelled using three different approaches at free-stream Mach numbers 0.235 and 0.3. These models were an inviscid flow prediction, a viscous flow prediction, where the dissipation was given only by the laminar viscosity and by the numerical dissipation, and a turbulent flow prediction, where the energy dissipation at the small scales of turbulence was modelled by Detached Eddy Simulation (DES). Single domain decomposition (SDD) and recursive domain decomposition (RDD) MPI parallelization algorithms were developed along with the DES model to run mesh refined tests. The parallelization efficiency of the two methods was investigated and the advantages and disadvantages of these were shown. The mesh-converged results of the $L/D = 0.71$ cylindrical cavity have been compared to experiment. Two counter-rotating convective vortices at the cavity downstream edge were found. The vortex core locations at various streamwise planes were located using streamlines of the spanwise and flow-normal time mean velocity components. The radiating pressure field directivity in the $L/D = 0.71$ and $L/D = 2.5$ was investigated at a $5L$ radial distance from the cavity centre. The two L/D configurations are characterized by a similar upstream directivity. The $L/D = 0.71$ cavity is louder and displays a secondary downstream peak. In the spanwise plane, the acoustic wave from the $L/D = 2.5$ cavity is asymmetric whereas it is symmetric in the $L/D = 0.71$ cavity. “Rossiter modes” and duct modes are found to co-exist in the cylindrical cavity. The Power Spectral Density (PSD) of the wall pressure from experiment and computation over the Mach number range 0 to 0.235 show an amplification of these modes at coincidence for the $L/D = 0.71$ cavity.

Acknowledgements

I wish to thank foremost my loving parents. Their constant help and support made this work possible. Over the years, they help me like no other and provide me with confidence and self-esteem. They gave me the opportunity to travel as well as study a subject that I was passionate about, without regrets and without questioning my choice.

I must thank my supervisor, Dr. Aldo Rona, for his support and suggestions over the past three and a half years of my PhD studies. He gave me the insight of some of the result and his knowledge to interpret them in a meaningful way. The good collaboration we developed over this time will outlast this PhD.

I cannot forget my colleagues and friends at the University of Leicester, above all Mohammed Fekry Farah El-Dosoky, Ivan Spisso, Manuele Monti, Davide Di Pasquale, and Pietro Ghillani. Useful discussions took place in front of a nice Italian coffee or just over my desk. Mohammed and Manuele have been unbelievably calm and patient towards my loud tone of voice in the study room and have always been supportive towards my work. Pietro is integrating the outcome of my work and that of Ivan, to overcome some of the limitations of the flow solver. Over the years and thanks to several house changes, I made new friends, among whom I wish to acknowledge Milena, Carson, Tom, Clara, Emmanouela, Massimiliano, Andrea, Serena, Cecilia, Matias, Dalia, Francesca and Omar .

This research project has been supported by a Marie Curie Early Stage Research Training Fellowship of the European Community's Sixth Framework Programme under contract number MEST CT 2005 020301. The grant offered me the opportunity to network at international conferences and find new friends and colleagues among the AeroTraNet Marie Curie Early Stage Training fellows.

The test cases were suggested by Airbus France. I wish to thank Alois Sengissen, Airbus France, for his helpful discussions during the AeroTraNet network meetings.

I wish to thank Andrea Tarsi and Ivan Girotto, Cineca, Casalecchio di Reno, Italy, who provided me with useful suggestions that made possible to improve the parallelization algorithm. This work was supported by the HPC-EUROPA project RII3-CT-2003-506079, financed by the European Community - Research Infrastructure Action "Structuring the European Research Area" of the Sixth Framework Programme. This gave me access to the SP6 and BCX High Performance Computing facilities at Cineca.

I thank also Sarfraz Nadeem and Themos Tsikas at NAG, who helped me in porting the code on HECToR, the UK's national high-performance computing service, which is provided by the UoE HPCx Ltd at the University of Edinburgh, Cray Inc and NAG Ltd, and funded by the Office of Science and Technology through EPSRC's High End Computing Programme.

Finally, I would like to acknowledge the support of Consorzio inter-universitario per le Applicazioni di Supercalcolo Per l'Università e la Ricerca (CASPUR), Rome, for access to the High Performance Computing platform Matrix, in the closing stages of my PhD work. The help of Carlo Maria Serio and Federico Massaioli in setting up this access is gratefully acknowledged. The Matrix computational time was supported by the Standard Proposal scheme of CASPUR.

Contents

List of Figures

List of Tables

Nomenclature

Roman Symbols

c	Speed of sound
D	Cylindrical cavity depth
d	Distance from the nearest wall
e	Internal energy
$\mathbf{F}$	Inviscid fluxes
f	Characteristic frequency
$f = 0$	Function describing the integration surface
$H(f)$	Heaviside function, $H(f) = 0$ for $f < 0$ and $H(f) = 1$ for $f \geq 0$
$\mathbf{I}$	Identity matrix
k	Turbulent kinetic energy
k_T	thermal conductivity
L	Cylindrical cavity diameter
M	Mach number
$\mathbf{n}$	Unit outward normal vector to $f = 0$
$nprocs$	Number of processors

p	Pressure
p'	Pressure fluctuation, $p' = p - p_\infty$
Pr	Prandtl number
$\mathbf{q}$	Heat flux vector
$\mathbf{q}_t$	Turbulent heat flux vector
Re	Reynolds number
s	Entropy
S_p	Speed-up
St	Stroual number $St = fL/u_\infty$
$\mathbf{t}$	Reynolds stress tensor
T	Absolute temperature
T	Temperature
T_0	Scalar time to perform one time step
$\mathbb{T}$	Lighthill stress tensor with component
T_p	Time to perform one time step using more than one processor
$\mathbf{U}$	Conservative variable vector
$\mathbf{u}$	Fluid velocity vector
$\mathbf{v}$	Source surface velocity vector

Greek Symbols

$\delta(f)$	Dirac delta function
Δ	Filtering length, $\Delta = \sqrt[3]{\delta V}$
γ	Specific heat ratio and $k - \omega$ – SST model constant

ν Kinematic viscosity

ω Specific dissipation rate of turbulent kinetic energy

ρ Density

ρ' Acoustic density fluctuation

τ viscous stress tensor

θ Momentum thickness

Superscripts

$\cdot$ Time derivative of

T Transpose operator

Subscripts

b Boundary cell or ghost cell

i Variable number

∞ Free stream condition

phy First interior cell

ret Quantity evaluated at retarded time

0 Stagnation condition

x Observer reference system

y Source reference system

Other Symbols

$\Box^2$ Wave or D'Alembert operator

$\frac{\mathrm{D}}{\mathrm{D}t}$ Material derivative of, $\frac{\mathrm{D}}{\mathrm{D}t} = \frac{\partial}{\partial t} + \mathbf{u} \cdot \nabla$

δV Cell volume

: Tensor scalar product

$\otimes$ Dyadic product

μ_l Dynamic viscosity

μ_t Eddy viscosity

∇ Gradient operator

u^+ Normalized velocity, $u^+ = u/u_\tau$

u_τ Friction velocity, $u_\tau = \sqrt{\tau_{wall}/\rho}$

Acronyms

CFD Computational Fluid Dynamics

CGNS CFD General Notation System

DES Detached Eddy Simulations

DNS Direct Numerical Simulation

HPC High Performance Computing

LES Large Eddy Simulation

MPI Message Passing Interface

OpenMP Open Multi-Processing

PDE Partial Differential Equations

PSD Power Spectral Density

PSD Power Spectral Density

RANS Reynolds-Averaged Navier-Stokes

RDD Recursive domain decomposition

SDD Single domain decomposition

SGS Subgrid Scale model

SPL Sound Pressure Level

Chapter 1

Introduction

1.1 Context

Advances in jet noise reduction have considerably increased the importance of noise from the engine fan and the airframe as a significant contribution to the overall aircraft noise, especially during landing (McPike, 1993). Civil airframes often feature recesses or grooves to accommodate service hatches and other ancillary equipment. The flow in these cavity-shaped recesses is unsteady and, at typical landing speeds, may feature large-scale instabilities. The most acoustically active airframe components in a civil aircraft are the high lift systems and the landing gear. Nonetheless, other components, such as fuel vents and the ailerons, also contribute to the overall noise emissions.

In an aircraft fuel tank, as fuel is supplied to the engines, air is let in through a vent to balance the tank internal pressure. This avoids any vacuum in the fuel tank that could stop the fuel flow or cause the tank to implode. The design and location of fuel vents vary among aircraft. Fuel vents are often cut in the underside wing skin. Alternatively, these are located on the wing trailing edge, as in Cessna 210s. Although the amplitude of fuel vent noise is relatively low, it happens to be over a frequency range higher than the one of high lift systems noise, therefore it is perceived by a ground observer as louder with respect to what its amplitude in decibel would suggest, due to the dB(A) weighting (Cambiano *et al.*, 2006). The fuel vent represents a niche of the broader subject of cylindrical cavity flows.

A cylindrical open cavity placed one metre downstream of the wing leading edge is herein investigated as an initial low fidelity fuel vent model of a wide-body civil air-

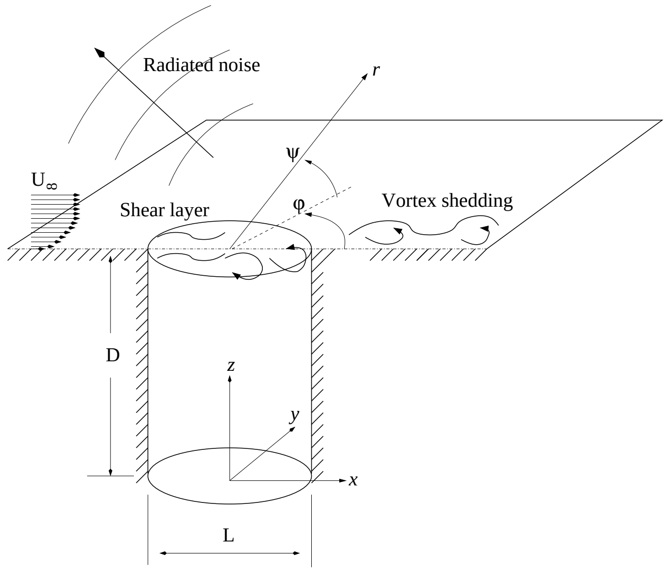

Figure 1.1: Cylindrical cavity flow.

craft. Past cavity aeroacoustic investigations mainly focussed on rectangular enclosures, due to the savings in computational time that can be achieved by the use of a Cartesian mesh. This study contributes to the literature by considering the cylindrical cavity flow. Figure 1.1 shows a schematic of the cylindrical cavity subject of the present study and the geometrical parameters.

1.2 Aims

The body of work of this thesis aims to extend the current understanding of the mechanisms that drive the unsteadiness in cylindrical cavity flow by a numerical approach. It aims to identify the instabilities that are likely to develop in such a cavity at typical aircraft landing speeds. The experimental work by Gaudet & Winter (1973), Hiwada *et al.* (1983) and Hering *et al.* (2006) on cylindrical cavity has shown that non-symmetric vortex structures can be found in this flow. The focus is to identify possible driving mechanisms that are responsible for the observed asymmetric flow pattern.

To achieve such knowledge, the existing in-house CFD code at the University of Leicester is developed to use high performance computing clusters. Such development represents a strong attractor for industry, as it offers the opportunity to reduce the time-scales of a typical industrial design.

The small body work on cylindrical cavity flow as compared to rectangular cavity flow over the past 30 years drives the interest of this research. The outcomes of the research will help future studies in terms of reliability and accuracy.

1.3 Methodology

An existing time-dependent in-house CFD flow solver is used to model the cylindrical cavity flow. The code is an explicit finite-volume solver that implements a Detached Eddy Simulation turbulent model validated and developed by El-Dosoky (2009). The author developed the MPI recursive domain decomposition algorithm to use the code on high performance computing clusters to allow numerically expensive simulations to run.

The flow solver linearises the convective flux vector by the Godunov method. The interface fluxes normal to the finite-volume unit cell boundaries are estimated by the approximate Riemann solver based on Roe (1981). The Monotone Upwind Scheme for Conservation Laws (MUSCL) interpolation of Van Leer *et al.* (1987) is used to achieve up to a third-order accurate spatial reconstruction.

The velocity vector gradients are computed by the Gauss divergence theorem using a staggered grid built across the cell interfaces.

The turbulent closure model is by a hybrid RANS/LES model. The RANS model consists on the $k - \omega$ model proposed by Menter (1992). The Yoshizawa (1986) one-equation SGS model is used to solve the LES turbulent closure as proposed by Dahlström & Davidson (2003). A blending function proposed by Menter (1992) is used at the RANS/LES interface. The present model is driven by a mesh-based eddy viscosity μ_t and $\rho k/\omega$ by the blending function.

The author developed the RDD parallelization algorithm and deployed the flow solver on HPC distributed-memory clusters.

1.4 Thesis outline

This thesis is divided into eight chapters. The first chapter gives the context of this work in terms of industrial and scientific interests driving the research. It then gives the the aims and objectives of this work and the expected outcomes.

The second chapter present the geometrical and the flow parameters that are given both in dimensional and non-dimensional form. It also proposed a literature review on cavity flow from the available literature. A classification based on geometrical and physical parameters is given to put the present study in the context of the open literature. The instability driving mechanisms and the modelling approaches of cylindrical cavity flows are reviewed.

The third chapter explains the different numerical models used to study the cylindrical cavity flow. The time-marching scheme used in the simulation and the relation between the Reynolds Averaged Navier-Stokes and Large Eddy Simulation variables is also given in this chapter. A brief discussion is presented on the standard data format and its post-processing.

The fourth chapter describes the code parallelization algorithms developed to run the code in the High Performance Computing (HPC) facilities. The performances of two algorithms is tested in terms of speed-up and parallelization efficiency.

In the fifth chapter, the physical domain discretization approach is explained for the selected cylindrical cavity flow configuration of chapter three. The mesh skewness is evaluated as a controlling parameter to the finite volume discretization. The free-stream boundary conditions used in the simulation are defined in this chapter.

The sixth chapter presents the results from the numerical models of the cylindrical cavity flow. The numerical data are divided into the time-averaged flow, the time-dependent aerodynamic flow, and the radiating near-field pressure. The latter is investigated in terms of time-dependent data (dynamic pressure fluctuation) and time-averaged data (near-field Sound Pressure Level). The numerical results from a 9.6 million cells mesh of the 0.71 aspect ratio deep cavity configuration are compared with available experimental data. The time-averaged velocity components and time-dependent pressure are investigated to characterize the cylindrical cavity instability as a function of the free-stream velocity. The predicted approaching boundary layer is compared with experiment.

Chapter seven, the conclusions, reports the achievements and the implications of the research for the scientific community. Finally, chapter eight deals with the future of cylindrical cavity flow research and the ways to overcome some of the limitations of this study.

Chapter 2

Cylindrical cavity test case description and background

2.1 Introduction

This chapter gives the geometry of the test case of this study as well as the flow parameters. These variables are organized into non-dimensional quantities that described the cavity flow as proposed by Colonius (2001).

This chapter aims to give background information about the cylindrical cavity flow presented in the available literature. A classification of the cylindrical cavity flow is proposed based on the existing rectangular cavity flow classification proposed by Roeck *et al.* (2004). The flow instability and the flow acoustic interaction as influenced by the cavity geometry and inflow conditions are herein described. The flow modelling of the cavity flow is herein briefly described by means of the different approaches to study the acoustic near-field and the source region. Finally a brief description to study the acoustic far-field is given.

2.2 Geometry and flow parameters

Figure 1.1 shows the schematic of a cylindrical cavity flow. The cylindrical cavity has a diameter L and a depth D, and it is fabricated as a recess into a flat plate. The air flow is characterized by the free-stream velocity u_∞, the free-stream speed of sound c_∞ and

the free-stream kinematic viscosity ν_∞. The boundary layer that develops on the flat plate is characterized by a boundary layer of thickness δ and momentum thickness θ. In figure 1.1, the Cartesian coordinates (x, y, z) are centred at the bottom of the cavity. The x axis coincides with the streamwise direction of the flow, the y axis coincides with the spanwise direction and the z with the wall normal direction. The aerodynamic instability is discussed in chapter 6 with respect to this system of coordinates.
To discuss the near-field acoustic predictions, a more convenient auxiliary reference system in spherical coordinates (ψ, ϕ, z) is used. The origin of the spherical reference system (ψ, ϕ, r) is the centre of the cavity open end.
The following coordinate transformations relate the two coordinate systems:

$$\begin{cases} x = r\cos\psi\cos\phi \\ y = r\cos\psi\sin\phi \\ z = r\sin\psi + D \end{cases} \tag{2.1}$$

$$\begin{cases} r = \sqrt{x^2 + y^2 + (z-D)^2} \\ \phi = \arctan\left(\frac{y}{x}\right) \\ \psi = \arcsin\left(\frac{z}{\sqrt{x^2+y^2+(z-D)^2}}\right) \end{cases} \tag{2.2}$$

Two cylindrical cavities are modelled in this thesis. In a cylindrical cavity, the characteristic length L and width W are both equal to the diameter. Block (1976) showed that in rectangular cavities where $L = W$, the flow is characterized by important spanwise structures. The three dimensionality of the flow structures adds to the modelling effort. The cavity diameter $L = 100$ mm and two cavity depth are chosen, $D = 40$ mm and $D = 140$ mm. These geometrical parameters were selected in consultation with Airbus France to be representative of a low fidelity model of a aircraft fuel vent. The different configurations are selected to evaluate the influence of the cavity depth on the flow instability.
Two free-stream flow velocities are analysed, $u_\infty = 80$ m/s and $u_\infty = 102$ m/s. These correspond to typical landing speeds of a wide-body civil aircraft. The flow is considered at International Standard Atmosphere (ISA) ground conditions. These are: a free-stream temperature $T_\infty = 288.15$ K, a free-stream pressure $p_\infty = 101325$ Pa, an

air density $\rho_\infty = 1.225$ kg/m^3, a free-stream speed of sound $c_\infty = 340.3$ m/s, and a kinematic viscosity $\nu_\infty = 1.461 \times 10^{-5}$ m^2/s.
A fully turbulent boundary layer approaches the cavity. The boundary layer momentum thickness θ is 1.35 mm at $u_\infty = 80$ m/s and is 1.29 mm at $u_\infty = 102$ m/s. It is assumed that the growth rate upstream of the cavity is not affected by any pressure gradient.
The cavity wall and the flat plate around it are modelled as impermeable adiabatic walls. It is assumed that the flow is not subject to any external heat source nor to external forces and it is a non-reactive flow.

2.3 Non-dimensional parameters

Colonius (2001) rearranged the dimensional flow parameters in section 2.2 into the corresponding non-dimensional parameters: L/W, L/D, L/θ, $Re_\theta = u_\infty\theta/\nu_\infty$, M_∞.
By definition, the characteristic length to width ratio $L/W = 1$ as the cavity is cylindrical. The two different diameter to cavity depth ratios are $L/D = 2.5$ and $L/D = 0.71$, to resolve the changes in the fuel vent pattern associated to the cavity depth at the given test conditions. Block (1976) and Ahuja & Mendoza (1995) showed that, for rectangular cavities, $L/W = 1$ represents a limit that separates a three-dimensional cavity from a two-dimensional ones.
To account for the influence of the incoming boundary layer thickness on the cavity flow instability, two different Re_θ are selected, $Re_\theta = 8850$ and $Re_\theta = 10750$. The remaining two non-dimensional quantities, L/θ and the Mach number M_∞, are selected in the simulation as $L/\theta = 65$ at $M_\infty = 0.3$, and $L/\theta = 62$ at $M_\infty = 0.235$.
Charwat *et al.* (1961) studied a wide range of non-dimensional parameters L/D, L/θ, Re_θ, M_∞ in a rectangular cavity flow. He showed that in the range of non-dimensional parameters selected in this study, the cavity flow is open and it is characterized by a major recirculation zone within the cavity and by an unsteady stagnation point on the downstream cavity wall.

2.4 Cylindrical cavity unsteady aerodynamics

Cavities can be classified into different types depending on their length to depth L/D or length to width L/W ratios. These types differ from each other in the way the aeroacoustic noise is generated and radiated. A classification of cavity flow is given in Roeck *et al.* (2004) for rectangular cavities and it is used in this thesis to classify the cylindrical cavity flow.

2.4.1 Classification on L/D: deep cavity and shallow cavity flow

In shallow cavities, $L/D > 1$, there can be more than one recirculation zone. For longer cavities $L/D > 5$, there can be a reattachment of the flow to the bottom of the cavity. Due to this flow pattern, the broadband noise dominates the acoustic field. Periodic components are present in the acoustic field but are of relatively small amplitude. To model such cavity flow, Direct Numerical Simulations (DNS) or Large Eddy Simulations (LES) can capture the broad-band spectrum of acoustically active flow structures. Other modelling approaches, such as Reynolds Averaged Navier Stokes (RANS) methods, are likely to give rather approximate predictions, due to the lack of information on the small scales of turbulence (Wang *et al.*, 2004).

Shallow cylindrical cavities may display a complex azimuthal recirculation in the enclosure, as shown experimentally by Gaudet & Winter (1973), Hiwada *et al.* (1983) and by Dybenko *et al.* (2006). Hiwada *et al.* (1983) show by wall pressure measurements that, for $1.5 < L/D < 2.5$, a cylindrical cavity may feature a diagonal outflow, in which mass ejection is uneven about the cavity mid-span. The preferential side of mass ejection switches from left to right of the mid-span, leading Hiwada *et al.* (1983) to define this regime as a switch flow. For $2.5 < L/D < 5$, Hiwada *et al.* (1983) identify a different flow regime that they refer to as flapping flow, due to fluctuations in the shear layer that spans the cavity open end.

Deep rectangular cavities are characterized by one or two recirculation zones that take part in a flow-resonant feed-back loop the tonal contributions from which dominate over the broad-band noise. The most dominant tones in the noise spectrum are typically the second and third cavity feed-back resonances. The radiated acoustic field has a directivity peak around $50°$ azimuth with respect to the inflow direction.

The flow in deep cylindrical cavities $L/D < 1.5$ is generally stable and symmetric with respect to the streamwise direction. Gaudet & Winter (1973) identified this behaviour using oil flow visualization and by streamline tracing over the cavity walls.

2.4.2 Classification on L/W: two-dimensional and three-dimensional flow

Early experimental work by Maull & East (1963) highlighted the presence of spanwise structures in cavity flows. A classification based on length to width ratio was first made by Block (1976). Based on her experimental research, she made a distinction between cavities where the acoustic field is two-dimensional, at $L/W < 1$, or three-dimensional, at $L/W > 1$. These findings were confirmed by the extensive research of Ahuja & Mendoza (1995). They found also that changing the width of the rectangular cavity does not affect the resonance frequencies but the overall sound pressure level decreases by up to 15 dB in three-dimensional cavities. The main conclusion from this research is that, for rectangular cavities of $L/W < 1$, it is possible to compare two-dimensional computational aeroacoustic results with experimental ones. For $L/W > 1$ geometries, the directivity and noise spectrum from two-dimensional numerical models can be used by an appropriate amplitude scaling factor to predict the acoustic far-field.

2.4.3 Classification on mean flow pattern: open and closed cavity flow

Figure 2.1(a) and 2.1(b) show a schematic of the open cavity flow and of the closed cavity flow respectively.

An open cavity flow is characterized by a main recirculation within the enclosure and possibly one or two secondary recirculations on the cavity floor. The flow separates at the cavity leading edge and reattaches at the cavity trailing edge, as shown in figure 2.1(a). In a closed cavity flow, the flow separates at the cavity leading edge and reattaches on the cavity floor. It then separates from the cavity floor further downstream and reattaches on the downstream wall. The upstream separation and reattachment points are the ends of a finite streamline that delimits an upstream flow recirculation

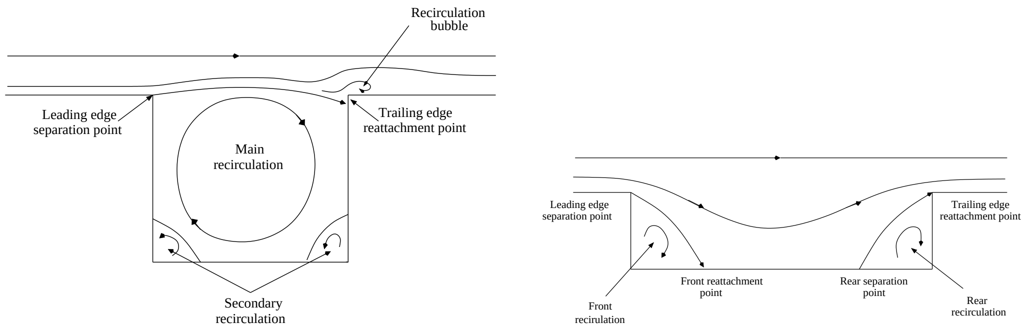

(a) Open cavity flow. (b) Closed cavity flow.

Figure 2.1: Two-dimensional sketch of mean cavity flow pattern.

region, close to the upstream cavity corner. Similarly, a larger recirculation is found near the downstream cavity wall.

The transition between the open and closed cavity regimes is generally associated to the length to depth ratio (Heller *et al.*, 1971; Rockwell & Naudascher, 1978). At low subsonic speeds, the critical L/D that separates the open and closed cavity regimes is shown by Sarohia (1977) to be $d_{crit} = L/D \approx 7-8$ for rectangular cavities. In practice, d_{crit} varies depending on a number of factors, among which the most influential ones are the free stream Mach number, M_∞, and the width to depth ratio, W/D (Atvars *et al.*, 2009; Plentovich *et al.*, 1993; Stallings Jr. & Wilcox Jr., 1987). At $L/D \sim d_{crit}$, a cavity can display intermittently both the open and closed flow patterns. When the cavity flow is closed for the majority of time, the enclosure is defined as transitionally closed. When the cavity flow is open for the majority of time, this is defined as transitionally open. The transition between open and closed regimes for cylindrical cavities is not readily documented in the open literature, possibly because the three-dimensional and unsteady nature of this flow prevents an analogous simple two-dimensional description of the flow spanning the open end.

Stallings Jr. & Wilcox Jr. (1987) studied the effect of the width to length ratio, W/L, on the flow over a cavity. They studied the centreline pressure distribution on the floor of a cavity of constant length and depth and variable width. As the cavity width decreases, the flow switches from transitionally open to transitionally closed at $W/D = 5$ when $d_{crit} = 13$. In cavities where $3 < W/D < 4$ the transition corresponds to a $d_{crit} = 12$. A further decrease in width gives a closed cavity flow. As the cavity width decreases, the

value of d_{crit} decreases. These studies illustrate the importance of taking into account the three-dimensional character of cavity flows.
Stallings Jr. & Wilcox Jr. (1987) and later Crook *et al.* (2007) investigated the three-dimensionality by measuring the lateral pressure gradients across the rear face of a rectangular cavity at supersonic flow speeds and using oil flow visualization techniques. It was found that, in a closed cavity, the pressure gradients are caused by the formation of vortices along the side walls as the flow expands into the cavity near the leading edge.
In open cavities, large lateral pressure gradients occur, although their magnitude is considerably less than that in closed cavity flow. The results of Stallings Jr. & Wilcox Jr. (1987) indicated that the side wall vortices are absent in open cavities, while a more recent investigation by Atvars *et al.* (2009) shows longitudinal shoulder vortices running along the floor of an open subsonic compressible cavity. Still, the effects of cavity width on the pressure distribution for open cavities are smaller compared to those in closed cavities. Increasing the width in open cavities generally results in an increase in wall pressure on the cavity rear face and on the rear portion of the cavity floor.

2.5 Cylindrical cavity noise

The frequency content of cavity noise contains both broad-band components, introduced by the turbulence in the shear layer that separates at the upstream cavity corner, and tonal components due to a feed-back coupling between the flow field and the acoustic field. Rossiter (1964) was one of the first researchers who described this feedback mechanism based on shadowgraphic observations on a number of different rectangular cavities. He concluded that the periodic flow pattern in the cavity can be described by a four step procedure:

I Vortices shed from the leading edge of the cavity are convected downstream along the shear layer until they reach the trailing edge of the cavity.

II At the trailing edge, the vortices interact with the downstream wall of the cavity and this causes the generation of acoustic waves. A part of these acoustic waves radiate above the cavity to the acoustic far-field.

III Pressure waves radiate inside the cavity in the upstream direction until they reach the leading cavity edge.

IV When reaching the upstream wall of the cavity, the pressure waves cause the shedding of a new vortex at the leading edge. The pressure waves influence the spacing between the different vortices and thus also determine the frequency of this feedback phenomenon.

Based on experimental results, Rossiter (1964) derived the following semi-empirical formula for the Strouhal number St of this periodic phenomenon:

$$St = \frac{fL}{u_\infty} = \frac{n - \alpha}{M_\infty + u_\infty/u_{conv}} \tag{2.3}$$

where f is tonal frequency, L is the length of the cavity, $n \in N$ the mode number, M_∞ the free stream Mach number, u_∞ the free stream velocity, u_{conv} the convection velocity of the vortices, and α a factor to account for the lag time between the passage of a vortex and the emission of a sound pulse at the cavity trailing edge. The model proposed by Rossiter (1964) does not provide numerical values for α and the ratio u_∞/u_{conv}. They are treated as empirical constants, depending on the length L to depth D ratio of the cavity. They are determined by Rossiter (1964) by a best fit to the measured data. The flow-acoustic resonance frequencies obtained from evaluating (2.3) with $n \geq 1$ are not an harmonic sequence, although some harmonics may be found in experimental spectra (Samimy *et al.*, 2004).
Equation (2.3) was subject to several empirical improvements for rectangular cavity flow over the years by several authors (Alvarez *et al.*, 2004; Bilanin & Covert, 1973; Block, 1976; Colonius, 2001; Covert, 1970; Grace, 2001; Grace *et al.*, 2004; Heller & Bliss, 1975; Heller *et al.*, 1971; Howe, 1997; Rockwell & Naudascher, 1978; Rowley & Williams, 2006; Tam & Block, 1978).
The formula of Block (1976) accounts for the effect of the bottom reflected acoustic wave and it is given by:

$$St = \frac{fL}{u_\infty} = \frac{n}{M_\infty\left(1 + \frac{0.514}{L/D}\right) + u_\infty/u_{conv}} \tag{2.4}$$

Czech *et al.* (2006) propose a correction that accounts for the circular edge shape in cylindrical cavities, which replaces the characteristic length L in (2.3) with L_{corr}, that is a function of the cavity diameter L:

$$L_{corr} = \frac{\sqrt{\pi}}{2} L \tag{2.5}$$

The formula of Block (1976) with the correction by Czech *et al.* (2006) is used in this thesis. Czech *et al.* (2006) use the original formulation of Rossiter (1964) in their work to fit experimental data on cylindrical cavity wall pressure fluctuations.

Cylindrical cavities can feature purely acoustic modes in addition to the Rossiter type flow-acoustic resonance. These takes the form of Helmholtz (1895) resonances and duct modes (Rayleigh, 1894). It is expected that high-amplitude tones are generated when the natural frequency of the flow-acoustic feed-back loop coincides with an acoustic mode (Marsden *et al.*, 2008).

The duct modes are the acoustic resonance of a pipe open at one end and closed at the other end. Rayleigh (1894) gives an expression for this configuration that includes the length of the pipe (H) and its radius (r). For a pipe closed at one end, the acoustic resonant modes are given by:

$$f = n \frac{c}{4\,(H + \alpha r)} \tag{2.6}$$

$n = 1, 3, 5, ..., 2k + 1,\ k \in N$ is an odd integer number that identifies the harmonic of each acoustic resonant mode in a pipe with one open end. α is a constant parameter. Rayleigh (1894) defined by asymptotic arguments the range $\pi/4 < \alpha < 8/(3\pi)$ and proposed $\alpha = 0.82$ for the real case of a finite length pipe. Nomura *et al.* (1960) and later Norris & Sheng (1989) found in different ways a more accurate value for α. Nomura *et al.* (1960) proposed $\alpha = 0.8217$ and Norris & Sheng (1989) proposed $\alpha = 0.82159$. The value from Norris & Sheng (1989) is used in this thesis.

From equation (2.6), the Strouhal number of the acoustic resonant modes is:

$$St = \frac{fL}{u_\infty} = \frac{n}{M_\infty} \frac{1}{4D/L + 2\alpha} \tag{2.7}$$

Rona (2007) solved the Helmholtz equation within a rectangular and within a cylindrical cavity to seek the acoustic resonant modes in these two configurations. For a

Table 2.1: Cylindrical cavity natural circular wavenumbers, $\xi_{l,m}R$.

m	0	± 1	2	3
$l = 0$	–	0	0	0
$l = 1$	1.2556	2.4048	3.5180	4.6123
$l = 2$	4.0793	5.5201	6.8661	8.1576

cylindrical cavity, Rona (2007) found that symmetric and anti-symmetric modes can be encountered in this geometry, in addition to axial acoustic modes. The Helmholtz equation is taken as having the general trial solution:

$$p_\theta = A_\theta \cos(m\theta - \alpha_m) + B_\theta \cos(-m\theta - \beta_m) \tag{2.8}$$

Rona (2007) seeks a particular form of equation (2.8) that satisfies the solid wall boundary condition at the cavity barrel and finds $p_r = A_r J_m(\xi r)$, where A_r is the amplitude of the radial acoustic pressure fluctuation, independent from r, and J_m is the m^{th} order Bessel function of the first kind. This is solved using the following relation for the Bessel functions:

$$\frac{J_m(\xi R)}{J_{m+1}(\xi R)} = \frac{\xi R}{m+1} \tag{2.9}$$

Equation (2.9) can be solved numerically for ξ, to determine the wavenumbers that satisfy the radial component of the Helmholtz equation with a cylindrical rigid wall as boundary condition. Rona (2007) gives numerical solutions of the first three radial and azimuthal mode wavenumbers, which is reported in table 2.5.

The acoustic mode frequencies are given by the following formula (Rona, 2007):

$$f_{l,m,n} = \frac{c}{2\pi}\left[\xi_{l,m}^2 + \left(\frac{n\pi}{D}\right)^2\right]^{1/2} \tag{2.10}$$

where l, m and n are integers ≥ 0 and $\xi_{l,m}$ is obtained from table 2.5 by dividing the stated values by the cylinder radius $R = 0.5L$.

Equation (2.10) shows mathematically that non-symmetric azimuthal instabilities can be supported in a cylindrical cavity geometry, extending the original principal component analysis of Rayleigh (1894) that is limited to axial modes only.

2.6 Aerodynamic field

Gaudet & Winter (1973) investigated the cylindrical cavity flow at different L/D ratios using oil flow visualization. The experiments were done at constant $M_\infty = 0.118$, $Re_L = 400000$ and inflow boundary layer to diameter aspect ratio $\delta/L = 0.24$. L/D varied from 0.746 to 25. $L/D > 4$ results in a closed cavity flow regime characterized by a symmetric recirculation upstream the reattachment line. Decreasing L/D changes the flow into the open cavity flow shown in figures 2.2 and 2.3. $L/D = 3.45$ in figure 2.2(a)-(a) is representative of the flapping condition also described by Hiwada *et al.* (1983). The switch flow condition is reached at $L/D = 2.13$ as shown in figure 2.2(c), where an asymmetric recirculation is found in the enclosure and results into a asymmetric convection on one side of the cavity. Hiwada *et al.* (1983) and Dybenko & Savory (2008) recently studied extensively the flow that result from a $L/D = 2.13$ cylindrical cavity. As the aspect ratio reduces further, a symmetric recirculation is found in the enclosure, as shown in figure 2.2(d). Although a $L/D = 0.746$ oil flow visualization is reported in Gaudet & Winter (1973), it is not reported in this thesis. The oil flow visualization was limited by the effect of gravity on the oil and a deeper cylindrical cavity flow was not studied.

Hiwada *et al.* (1983) also studied the effect of a cylindrical hole on the drag coefficient and on the heat transfer coefficient at various L/D at constant free-stream velocity and boundary layer thickness. Figure 2.4 shows the wall pressure fluctuation sampled over 20 second using a pressure probe. The resulting pressure coefficient of the symmetric and asymmetric flow is shown in figure 2.5. Hiwada *et al.* (1983) used H for the cavity depth and D for the cavity diameter. The aspect ratio L/D in this thesis is related to the work by Hiwada et al. by $L/D = 1/(H/D)_{Hiwada}$. Different regimes are responsible for the resulting wall pressure fluctuation. $L/D = 10$ is the statistically steady condition that correspond to a closed cavity with a symmetric recirculation in the upstream wall. $L/D = 2.5$ and $L/D = 3.33$ correspond to the flapping open cavity flow. $L/D = 2.5$ and $L/D = 1.67$ are switch asymmetric open cavity flows and $L/D < 1.25$ is a symmetric open cavity flow. In this experiment, the asymmetric recirculation was found at $L/D = 2.5$, as shown in figure 2.5(b). The switch between a symmetric recirculation and an asymmetric one happened at $L/D \approx 3$ as it was inferred by the pressure coefficient (C_p) in figure 2.5(a). $L/D = 1$ resulted into a symmetric

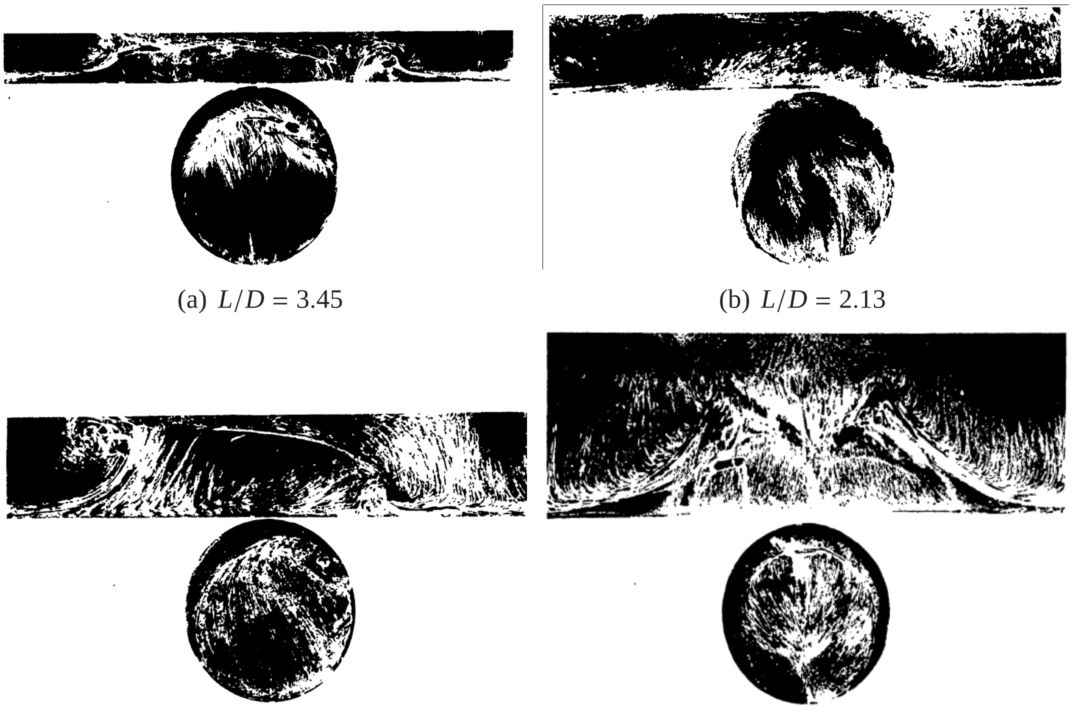

(a) $L/D = 3.45$ (b) $L/D = 2.13$

(c) $L/D = 1.67$ (d) $L/D = 0.93$

Figure 2.2: Oil-film flow visualization of cylindrical cavity at various L/D at $M_\infty = 0.118$, $Re_L = 400000$ and $\delta/L = 0.24$ (Gaudet & Winter, 1973). Cavity inner domain.

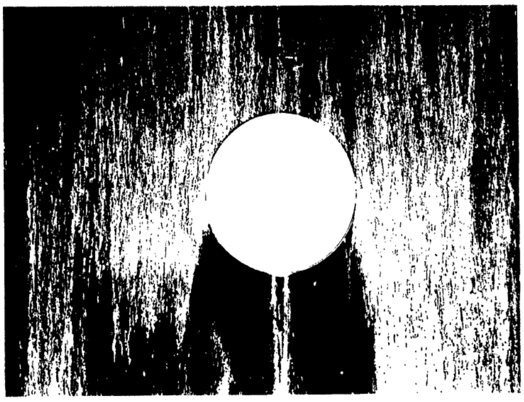

(a) $L/D = 3.45$

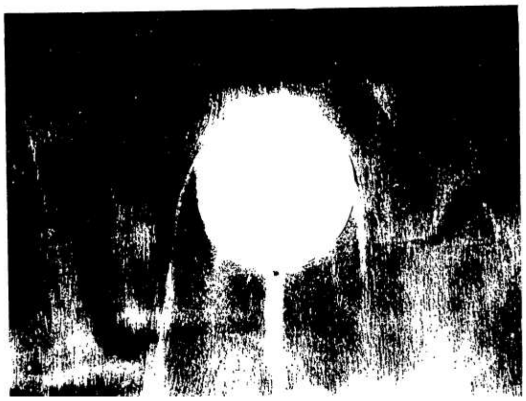

(b) $L/D = 2.13$

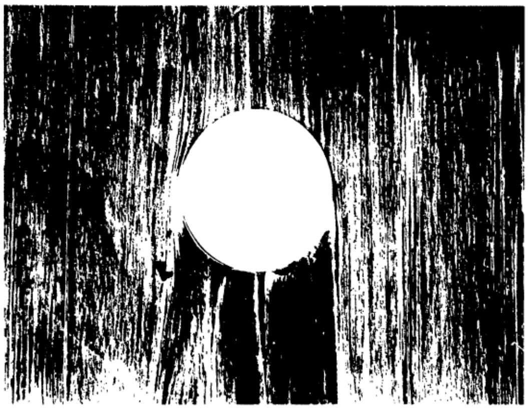

(c) $L/D = 1.67$

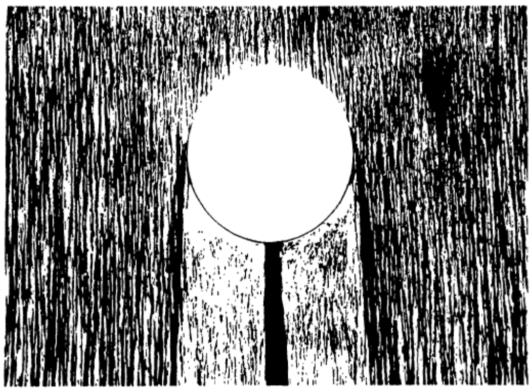

(d) $L/D = 0.93$

Figure 2.3: Oil-film flow visualization of cylindrical cavity at various L/D at $M_\infty = 0.118$, $Re_L = 400000$ and $\delta/L = 0.24$ (Gaudet & Winter, 1973). Cavity outer domain.

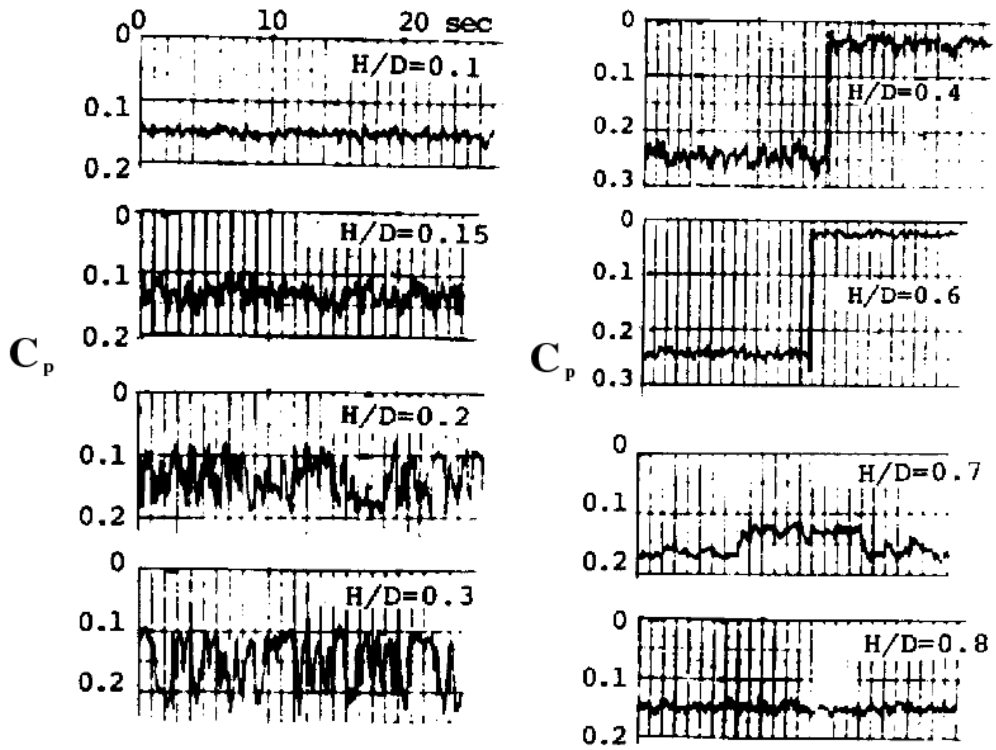

Figure 2.4: Wall pressure fluctuation varying $1.25 < L/D < 10$ from Hiwada *et al.* (1983). $M_\infty = 0.074$, $Re_L = 111300$ and $\delta/L = 0.72$. $L/D = 1/(H/D)_{Hiwada}$.

patter of C_p due to the symmetric flow recirculation at this flow regime. This result was confirmed by Marsden *et al.* (2008) at $L/D = 1$ and $M_\infty = 0.235$.

Dybenko & Savory (2008) recently repeated the experiment by Hiwada *et al.* (1983) and studied the Power Spectral Density (PSD) that results from the wall pressure fluctuation at three aspect ratios $(h/D)_{Dybenko} = 0.2$, 0.47 and 0.7 that correspond to $L/D = 5$, 2.13 and 1.43 by $L/D = (h/D)^{-1}_{Dybenko}$. In figure 2.6, a vertical shift by 20dB is applied to each PSD. The loudest cylindrical cavity flow corresponds to the deepest cavity configuration at $L/D = 1.43$. The experiments were done in a close circuit wind tunnel where the PSD of the background noise was comparable among the three test cases. The results were therefore not conclusive due to this limitation. Comparing the PSD of the $L/D = 2.13$ shallow cavity with the PSD from $L/D = 1.43$, it can be inferred that in a deeper cavity tonal components are more dominant in the spectrum compared to a shallower cavity. Dybenko & Savory (2008) did not find any evidence of concurrent hydrodynamic and acoustic instabilities as the frequency peak does not correspond to

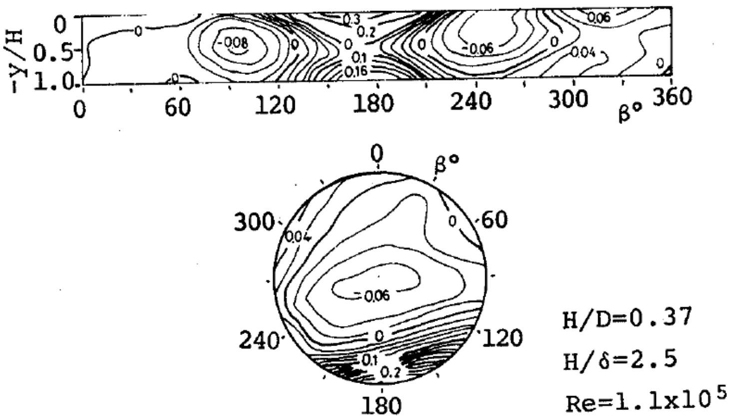

(a) $L/D = 2.7$

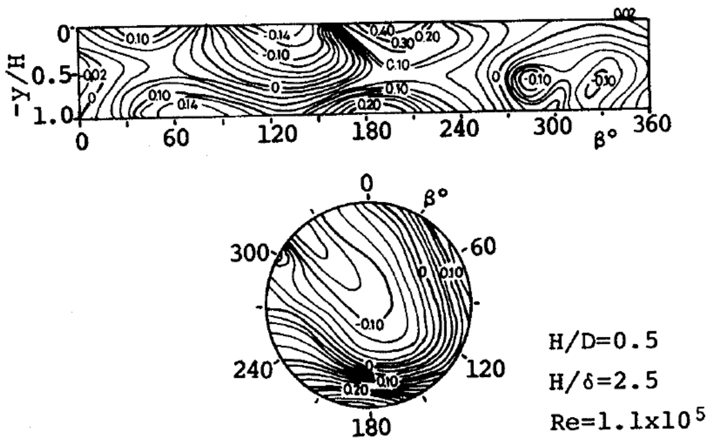

(b) $L/D = 2$

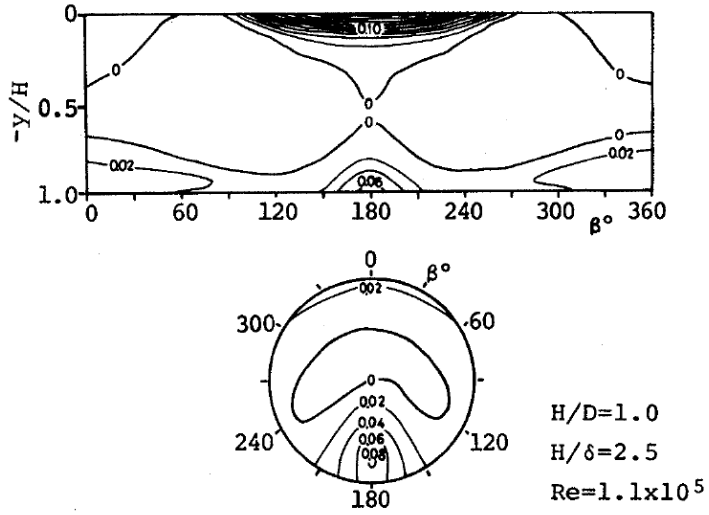

(c) $L/D = 1$

Figure 2.5: Pressure coefficient at varying L/D from Hiwada *et al.* (1983). $M_\infty = 0.074$, $Re_L = 111300$ and $\delta/L = 0.72$.

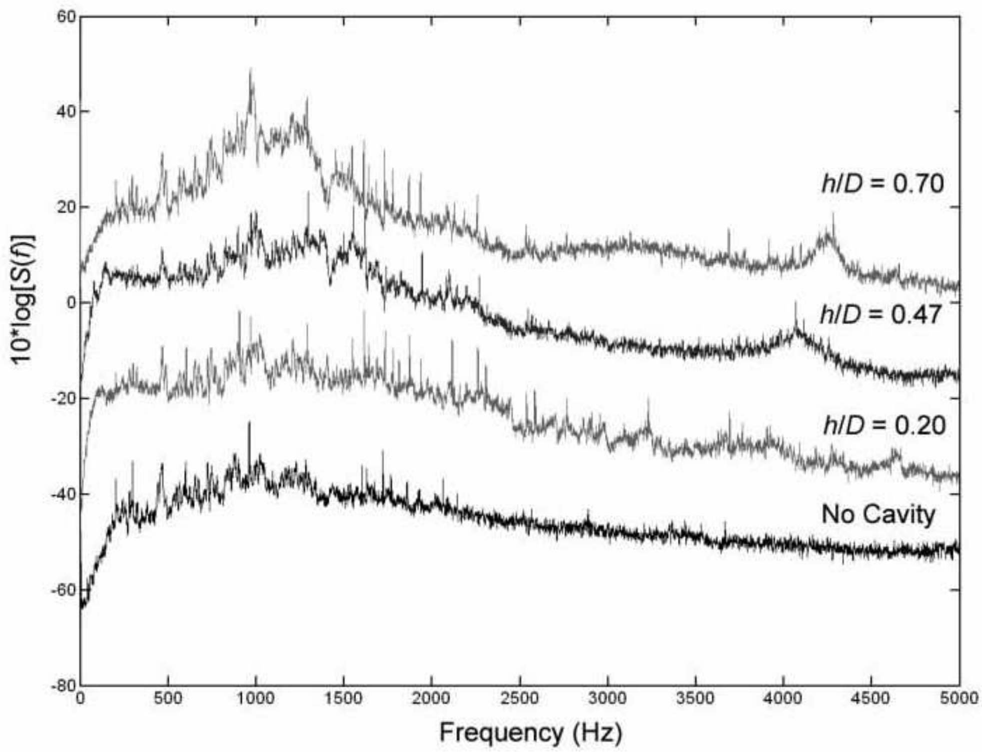

Figure 2.6: Wall pressure fluctuation PSD from Dybenko & Savory (2008). $M_\infty = 0.08$, $Re_L = 130000$ and $\delta/L = 0.72$. $h/D = 0.2$, 0.47 and 0.7 in the legend corresponds to $L/D = 5$, 2.13 and 1.43 respectively.

any of the instability modes described in section 2.5

2.7 Modelling cavity flows and parallelization

The experimental work by Dybenko *et al.* (2006) and by Hering *et al.* (2006) and the numerical work by Grottadaurea & Rona (2007a,b) shows that cylindrical cavities develop a rather unique flow instability that is fundamentally different from the well-documented Rossiter (1964) mechanism. The presence of cylindrical cavity geometries on airframes motivates the investigation and characterization of this peculiar instability mechanism.

From the available literature on rectangular cavities (Colonius & Lele, 2004), it is known that the momentum thickness θ at the cavity leading edge plays an important role in the selection of the modes and in governing the shear layer growth rate that spans an open cavity (Charwat *et al.*, 1961; Colonius & Lele, 2004; Rowley *et al.*, 2002; Tam, 2004). The importance of θ on the mode selection of rectangular cavities is shown by Colonius *et al.* (1999) on a mode map.

Direct numerical simulation (DNS) of compressible flow is still limited to low Reynolds number and high Mach number models. For a fully three-dimensional simulation, the total number of floating point operations to resolve all the relevant scales of motion in the flow and to cover at least one wavelength of the radiated sound in the computational domain is of the order of $Re_{\infty}^{3}/M_{\infty}^{4}$ (Crighton, 1975). DNS is more suitable to validate an aeroacoustic method that includes a turbulence closure model than to perform a full-scale simulation.

A Large Eddy Simulation (LES) (Chow & Gao, 2004; Piomelli *et al.*, 1997; Schröder & Ewert, 2005; Seror *et al.*, 2001) is an attractive choice to model flows of industrial interest. It provides good information on the noise sources to compute both the broadband spectrum and the single tones in the radiated noise. However, the computational effort due to the stringent near-wall grid resolution required by a high-Reynolds number flow is a major obstacle to the routine use of LES in these types of flow (Wang *et al.*, 2004).

Time-dependent numerical prediction used in geometries of industrial interest can be obtained by hybrid RANS/LES, as in Arunajatesan & Sinha (2003). A Detached Eddy Simulation (DES) was performed by Hedges *et al.* (2002) and an Unsteady-RANS (URANS) by Singer & Guo (2004). A careful choice of the turbulent closure model can be done a priori if the instability mechanism driving the flow of interest is known. The URANS approach provides the lowest level of flow detail and accuracy (Wang *et al.*, 2004), though it is the least computationally demanding approach among URANS, DES and LES and it can be effective in capturing the large-scale fluid motion and its associated sound (Rona, 2006).

Spalart (2000) offered an overview of the methods available in CFD to model the flow at different regimes and their advantages and limitations in terms of computational cost and numerical mesh requirements. In spite of recent advantages in LES wall boundary closures (Li & Hamed, 2008), the lower computational cost of DES for modelling geometry-induced flow separation motivates the development of this technique. The complexity associated with modelling the RANS-LES interface in DES is counter-balanced by the reduction in close-walls mesh resolution required by this model. This makes the DES suitable for the simulations presented in this thesis and makes the code suitable for future industrial applications.

High performance computing allows to simulate larger systems than what can be done on a scalar machine (Long *et al.*, 2004). Specifically, mesh-refined test cases of the order of 10 million cells were recently used to simulate three-dimensional rectangular cavity flows, to obtain predictions with a greater spectral breadth in both frequency and wave-number space (Atvars *et al.*, 2009; Brès & Colonius, 2008). The main driver is to better render in the simulation the process of dissipation of the energy from the dominant scales of motion inside the enclosure. These large scales are the ones that are selectively amplified by the open cavity fluid dynamic instability mechanism. The early models for such a kinetic energy dissipation process relied simply on numerical viscosity. A better representation of this process involves resolving, at least in part, some of the cascading of the modal energy to the smaller scales of motion.

Advances in code parallelization and in multi-processor hardware development allow nowadays the modelling of representative industrial geometries by conventional Computational Fluid Dynamics (CFD) (Chen *et al.*, 2004; Long *et al.*, 2004). Different challenges are nonetheless posed by computational aeroacoustics. A larger computational domain with respect to conventional CFD is required to resolve a full wavelength of the radiated noise. A more accurate, less dissipative and efficient non-reflective boundary condition needs to be applied to correctly evaluate the amplitude of the pressure fluctuations in the near-field acoustic domain. High-order low dissipation and dispersion schemes have lowered the cost of aeroacoustic models to a more affordable level.

Simulations that resolve the flow-turbulence interactions that characterize a turbulent cavity flow cannot be run on a single processor or on a small shared memory cluster.

Nowadays, large shared memory clusters are less popular and more expensive as compared to large distributed memory clusters, where thousands of processors are interconnected, or to vector machines, where vectorization of the operations further reduces the computational time. For instance, to resolve the relevant large scales of motion with a Detached Eddy Simulation approach, a refined mesh of 6 to 8 million cells is required. This mesh simply cannot fit in 4 GB of RAM of a single processor and, even if it did, the computational time would exceed 460 days. Therefore, to perform the numerical modelling within a suitable time-scale, it is essential to port the numerical work on a High Performance Computing (HPC) cluster, using Message Passing Interface (MPI).

Open Multi-Processing (OpenMP) is more user-friendly as compared to MPI, but it can be used only in a shared memory cluster and reduces the freedom in parallelization allowed to the user. Over the past few years, these limitations have prompted the scientific community to move to MPI, to exploit the Tera-flops performance of such systems.
MPI enhances the scaling performance of CFD codes and allows to perform production runs on the largest computer facilities in the world. It generates numerical predictions of significantly larger spectral resolution than from using other currently available parallelization methods.

2.8 Aeroacoustic approaches

The flow above and within the cavity enclosure is generally divided into three regions to simplify its modelling: a source region, the acoustic near-field and the acoustic far-field. The source region coincides with the cavity and its surrounding extending radially outwards from the enclosure by up to one wavelength of the radiated noise lowest significant frequency. The acoustic near-field extends up to five wavelengths, beyond which lies the acoustic far-field. The source region can only be modelled by the methods described in section 2.7.
In the acoustic near-field, a Ffowcs Williams & Hawkings (1969) acoustic analogy does not decouple acoustic refraction and reflection effects from the noise generation process. Alternative approaches to predict aerodynamic noise in the non-homogeneous acoustic near-field are by solving the discrete Euler equations, either the linear LEE proposed by Bogey *et al.* (2002) or the non-linear NLEE (Schröder & Ewert, 2005), or the Acoustic Perturbation Equation (APE) proposed by Ewert & Schröder (2004). These approaches are not being pursued in the current work as they are more appropriate for near-field noise predictions from acoustically compact sources in an underlying steady mean flow, whereas this investigation focuses on resolving the flow unsteadiness that is producing aerodynamic noise.
The acoustic far-field correspond to a region where the wave equation fully describes the flow.

2.9 Conclusion

The cylindrical cavity geometry and inflow conditions to be studied by numerical modelling have been defined. These are stated in terms of the non-dimensional parameters proposed by Colonius (2001) that are relevant to identify the cavity flow unsteadiness. A literature review on cylindrical cavity flow has been conducted to identify the flow regime of the test cases. Following the classification proposed by Roeck *et al.* (2004) on rectangular cavities, the cylindrical cavities subject of this study are open. A symmetric flow organization is expected in the $L/D = 0.71$ cavity whereas an asymmetric one is expected in the $L/D = 2.5$ cavity. The flow is three-dimensional. To model such complex cavity flow, a parallel three-dimensional flow solver that includes a DES turbulent model is used, to achieve mesh converged result in a shorten time-scale as compare to Direct Numerical Simulation.

Chapter 3

Methodology

3.1 Introduction

This chapter explains the numerical model of the Euler equation, the Navier-Stokes equations and the DES turbulence model equations used to study the cylindrical cavity. The boundary conditions used in the different simulation are also described in this chapter. The validation of the flow solver done by El-Dosoky (2009) is analysed with respect to the flow instability that characterize the flow subject of this study. A brief description of the data format and post-processing is also proposed in this chapter.

3.2 Inviscid numerical model

3.2.1 Euler equations

The conservative form of the time-dependent Euler equations is:

$$\frac{\partial}{\partial t}\mathbf{U} + \nabla \cdot \mathbf{F}_c = 0 \tag{3.1}$$

where **U** is the conservative variable vector and **F** are the inviscid flux vector. They are defined as:

$$\mathbf{U} = \begin{pmatrix} \rho \\ \rho\mathbf{u} \\ \rho e \end{pmatrix} \quad \mathbf{F} = \begin{pmatrix} \rho\mathbf{u} \\ \rho\mathbf{u}\otimes\mathbf{u} + p\mathbf{I} \\ \rho\mathbf{u}\,(e + p/\rho) \end{pmatrix} \tag{3.2}$$

where $\mathbf{u}$ is the fluid velocity vector with components u_i, e is the specific internal energy, p is the static pressure and $\mathbf{I}$ is the identity matrix. In equation (3.2), the rows relate to the conservation of mass, momentum, and energy, respectively.
e is related to the fluid temperature T and velocity $\mathbf{u}$ by

$$e = \frac{1}{\gamma - 1}RT + \frac{1}{2}\mathbf{u}\cdot\mathbf{u} \tag{3.3}$$

where R is the specific gas constant. Temperature, pressure and density are related by the equation of state for a perfect gas. This is:

$$p = \rho RT \tag{3.4}$$

In this work, air is assumed a perfect gas.
Subtracting the divergence of the conservation of momentum from the time derivative of the conservation of mass, Lighthill (1961) obtained an inhomogeneous wave equation where the sources of noise are on the right hand side:

$$\Box^2\rho' = \nabla\cdot\nabla\cdot\mathbb{T} \tag{3.5}$$

where $\mathbb{T}$ is the Lighthill stress tensor, defined as

$$\mathbb{T} = \rho\mathbf{u}\otimes\mathbf{u} + \left(p - c_\infty^2\rho\right)\mathbf{I} \tag{3.6}$$

and c_∞ is the speed of sound in the unperturbed medium at rest.

3.2.2 Finite-volume flux vector discretization

The physical domain is discretized by an assembly of topologically rectangular control volumes V_i, where subscript i indicates the i^{th} control volume in the non-uniform mesh.

Integrating equation (3.1) over each control volume V_i gives

$$\int_{V_i} \frac{\partial \mathbf{U}}{\partial t} \mathrm{d}V + \int_{V_i} \nabla \cdot \mathbf{F}_c \mathrm{d}V = 0 \tag{3.7}$$

Assuming a stationary computational domain and applying the Gauss divergence theorem, equation (3.7) can be written as:

$$\frac{\partial}{\partial t} \int_{V_i} \mathbf{U} \mathrm{d}V + \oint_{S_i} \mathbf{F}_c \cdot \mathbf{n} \mathrm{d}S = 0 \tag{3.8}$$

Let

$$\mathbf{U}_i = \frac{1}{V_i} \int_{V_i} \mathbf{U} \mathrm{d}V \tag{3.9}$$

$$\oint_{S_i} \mathbf{F}_c \cdot \mathbf{n} \mathrm{d}S = \sum_{k=1}^{N_{faces}} \mathbf{F}_{c,k} \cdot \mathbf{n}_{i,k} S_{i,k} \tag{3.10}$$

where N_{faces} is the number of faces in the control volume V_i, $S_{i,k}$ is the k^{th} face of V_i and $\mathbf{n}_{i,k}$ is its inwards normal.
Equation (3.7) can be written in a compact form as:

$$V_i \frac{\partial \mathbf{U}_i}{\partial t} + \mathbb{R}_i = 0 \tag{3.11}$$

where $\mathbf{U}_i$ is the mean value of the conservative variable vector over the cell volume V_i and $\mathbb{R}_i$ is the residual generated from the discretized terms and it is equal to

$$\mathbb{R}_i = \sum_{k=1}^{N_{faces}} \mathbf{F}_{c,k} \cdot \mathbf{n}_{i,k} S_{i,k} \tag{3.12}$$

To solve the Euler equations, the residual operator $\mathbb{R}_i$ in equation (3.12) needs to linearise the flux vector $\mathbf{F}_c$. The Godunov method, or Flux Difference Splitting, is used. Interface fluxes normal to the finite-volume unit cell boundaries are estimated by the approximate Riemann solver based on Roe (1981). The Roe (1981)'s approximate Riemann solver is first-order accurate in space, since the solution is projected on each cell as a piecewise constant state (Hirsch, 1988). To reduce the excessive artificial dissipation of the first order method, Van Leer *et al.* (1987) replaced the piecewise constant

state assumption with a quadratic reconstruction, leading to a higher order spatial reconstruction, the Monotone Upwind Scheme for Conservation Laws (MUSCL) interpolation. Following Manna (1992), the coefficients in the reconstruction are chosen to give a third-order accurate reconstruction of the spatial gradients in regions of smooth flow. This reconstruction uses four contiguous cells in the direction of the reconstruction, thus to connect two computational blocks a minimum of two layers of ghost cells are required to make the flow solver block independent. Sweby (1984) proved that a Total Variation Diminishing (TVD) scheme is sufficient to achieve numerical stability. As a monotonic scheme is TVD, then the MinMod limiter is introduced to achieve a monotonic behaviour in regions of model flow discontinuities. Details of the implementation of these schemes are given in El-Dosoky (2009).
At the computational domain boundaries, a frame of one ghost cell deep is used to preserve the second-order accurate reconstruction in the domain interior.

3.2.3 Boundary Conditions

The computational domain is divided into independent computational blocks. Each block is surrounded by ghost cells. The ghost cells along the computational domain outer boundaries are generated in the code by mirroring the first interior cell about the boundary plane along the external boundaries of the computational domain. Along inter-block boundaries, the first and the second interior cell geometries of the abutting block define the ghost cell rind, which is two cells deep along an inter-block boundary. The flow states of the first and second interior cell of the abutting block are copied into the newly defined ghost cells. Boundary flow states are imposed in the ghost cells.

Inviscid Wall

An impermeability condition is imposed at the physical wall boundaries. This corresponds to $\mathbf{u} \cdot \mathbf{n} = 0$ at the boundary S between the first interior cell and the ghost cell, where $\mathbf{n}$ is the inward normal vector to S. This is numerically achieved imposing

$$\mathbf{u}_b = \mathbf{u}_{phy} - 2\left(\mathbf{u}_{phy} \cdot \mathbf{n}\right)\mathbf{n} \tag{3.13}$$

where the subscript *phy* denotes the flow state at the first interior cell and b the flow state at the ghost cell.
The flow state in the boundary cell is:

$$\mathbf{U}_b = \begin{pmatrix} \rho_{phy} \\ \rho_{phy}\mathbf{u}_b \\ \rho_{phy}e_{phy} + \rho_{phy}/2\left(\mathbf{u}_b \cdot \mathbf{u}_b - \mathbf{u}_{phy} \cdot \mathbf{u}_{phy}\right) \end{pmatrix} \tag{3.14}$$

Non-reflective far-field

The far-field condition switches between a subsonic inflow condition and a subsonic outflow condition, depending on the value of the inner flow velocity component normal to the surface boundary, according to CFD General Notation System standard as described in chapter 3.7. Robust and accurate Non-Reflective Boundary Conditions (NRBC) are crucial in computational aeroacoustic applications (Hu, 2004). To obtain a non-reflective boundary condition, a 3D extension of the characteristic based boundary condition of Giles (1990) is used as in Givoli (1991). To limit the non-physical reflections caused by the numerical scheme, the following procedure is followed, depending on whether the flow is entering or exiting the computational domain boundary. At the far-field, the mean flow parameters need to satisfy a reference free stream condition:

$$\begin{pmatrix} p \\ T \\ \mathbf{u} \end{pmatrix} = \begin{pmatrix} p_\infty \\ T_\infty \\ \mathbf{u}_\infty \end{pmatrix} \tag{3.15}$$

Consider the one-dimensional flow in the direction of the boundary outward unit normal $\mathbf{n}$. The incoming Riemann invariant R^- is defined from the free-stream condition as:

$$R^- = \mathbf{u}_\infty \cdot \mathbf{n} - \frac{2c_\infty}{\gamma - 1} \tag{3.16}$$

where c_∞ is the free stream speed of sound, $c_\infty = \sqrt{\gamma R T_\infty}$.
The outgoing Riemann invariant R^+ is defined from the first interior cell towards the

surface of the computational domain boundary as:

$$R^{+} = \mathbf{u}_{phy} \cdot \mathbf{n} + \frac{2c_{phy}}{\gamma - 1} \tag{3.17}$$

where c_{phy} is the speed of sound at the computational domain interior, $c_{phy} = \sqrt{\gamma R T_{phy}}$. The speed of sound ($c_S$) and the normal velocity component ($\mathbf{u}_S \cdot \mathbf{n}$) of the incoming wave at the boundary interfaces are defined as:

$$c_S = \frac{\gamma - 1}{4}\left(R^{+} - R^{-}\right) \tag{3.18}$$

$$\mathbf{u}_S \cdot \mathbf{n} = \frac{R^{+} - R^{-}}{2} \tag{3.19}$$

Consider the sign of the surface normal velocity component $\mathbf{u}_S \cdot \mathbf{n}$. This can be either positive or negative. This determines whether an outflow or an inflow condition is to be used locally at the far-field boundary.
The outflow condition is used where $\mathbf{u}_S \cdot \mathbf{n} > 0$ is:

$$\mathbf{u}_b = \left[\mathbf{u}_{phy} - \left(\mathbf{u}_{phy} \cdot \mathbf{n}\right)\mathbf{n}\right] + \left(\mathbf{u}_S \cdot \mathbf{n}\right)\mathbf{n} \tag{3.20}$$

$$\rho_b = \left(\frac{\rho_{phy}^{\gamma} c_S^2}{\gamma p_{phy}}\right)^{\frac{1}{\gamma-1}} \tag{3.21}$$

$$p_b = \frac{\rho_b c_S^2}{\gamma} \tag{3.22}$$

The inflow condition is used where $\mathbf{u}_S \cdot \mathbf{n} \leq 0$ is:

$$\mathbf{u}_b = \left[\mathbf{u}_{\infty} - \left(\mathbf{u}_{\infty} \cdot \mathbf{n}\right)\mathbf{n}\right] + \left(\mathbf{u}_S \cdot \mathbf{n}\right)\mathbf{n} \tag{3.23}$$

$$\rho_b = \left(\frac{\rho_{\infty}^{\gamma} c_S^2}{\gamma p_{\infty}}\right)^{\frac{1}{\gamma-1}} \tag{3.24}$$

$$p_b = \frac{\rho_b c_S^2}{\gamma} \tag{3.25}$$

The conservative variable vector that is imposed at the ghost cell is:

$$\mathbf{U}_b = \begin{pmatrix} \rho_b \\ \rho_b \mathbf{u}_b \\ \frac{1}{\gamma-1} p_b + \frac{1}{2}\rho \mathbf{u}_b \cdot \mathbf{u}_b \end{pmatrix} \tag{3.26}$$

Subsonic inflow

The subsonic inflow boundary condition is formulated following the same characteristics based approach as for the far-field boundary condition for a three-dimensional flow. Four characteristic waves (λ_2 to λ_5) move towards the domain interior. It is therefore necessary and sufficient to impose four conditions at a subsonic inflow boundary. It is common practice to impose the flow density ($\rho_S = \rho_\infty$) and the flow velocity vector ($\mathbf{u}_S = \mathbf{u}_\infty$). The subscript ∞ is used in this section to identify the reference inflow state. A similar approach to the non-reflective far-field condition is followed. In equation (3.16), the speed of sound is estimated using the remaining outgoing characteristics λ_1 for which:

$$p_\infty \equiv p_{phy} \tag{3.27}$$

and consequently

$$c_\infty = \sqrt{\gamma \frac{p_{phy}}{\rho_\infty}} \tag{3.28}$$

Equations (3.18) and (3.19) define c_S and $\mathbf{u}_S \cdot \mathbf{n}$. Then equations (3.23), (3.24) and (3.25) are used with equation (3.27) to estimate $(\rho_b, \mathbf{u}_b, p_b)$, from which the conservative variable vector $\mathbf{U}_b$ is obtained by equation (3.26).

Subsonic outflow

In the subsonic outflow condition, only one characteristic wave is moving towards the domain interior (λ_1), therefore only one condition is applied. The domain back-pressure is imposed. In an Euler model and for zero pressure gradient boundary layers, this pressure coincides with the free-stream one.

Equation (3.18) reduces to:

$$c_S = \sqrt{\frac{\gamma}{\rho_{phy}} \frac{\left(\sqrt{p_\infty} + \sqrt{p_{phy}}\right)}{2}} \tag{3.29}$$

Equation (3.19) reduces to:

$$\mathbf{u}_S \cdot \mathbf{n} = \mathbf{u}_{phy} \cdot \mathbf{n} + \sqrt{\frac{\gamma}{\rho}} \frac{\sqrt{p_\infty} + \sqrt{p_{phy}}}{\gamma - 1} \tag{3.30}$$

equations (3.20), (3.21) and (3.22) are then used to specify $\mathbf{u}_b$, ρ_b and p_b. Equation (3.26) is now fully defined and it is used to specify the conservative variable vector in the subsonic outflow condition at the ghost cells.

3.2.4 Validation

The three-dimensional Euler flow solver was validated by El-Dosoky (2009) with three test cases of progressing level of difficulty: a shock-tube problem, a supersonic flow on a wedge and a spherical expansion. The shock-tube problem consists on the development of a normal shock wave propagating from left to right due to pressure and density difference imposed at the starting condition. The computational domain was divided into four zones to test the inter-block boundary communication. The result shows a good agreement with respect to the analytical solution and displays only 2.5% error close to the sharp discontinuities (El-Dosoky, 2009) comparing to the analytical solution by Hirsch (1988). The supersonic flow on the wedge is characterized by an inflow condition at $M_\infty = 2$ that approaches a 10° wedge and results into a supersonic flow at the outlet. The analytical solution is obtained by solving the Rankine-Hugoniot equations. The oblique shock is well-captured by the numerical model with only a 0.3% error in the degree angle and its reflection on the no-slip flow and interaction with the expansion wave is also captured correctly, as shown by El-Dosoky (2009). The spherical expansion is a three-dimensional equivalent of the the shock-tube problem, where a small sphere of a high density and pressure is let to expand in a cube of lower density and pressure. Non-dimensional energy and density plots are compared to the reference analytical solution in Toro (1999) and show similar result to those of a shock tube problem (El-Dosoky, 2009). No spurious reflection is found across the internal boundary of the multi-block computational domain, neither where this is crossed by the advancing shock wave, nor where this is crossed by the contact discontinuity. The cylindrical cavity model is characterized by a circular sharp edge, where a contact discontinuity is given by the difference in the velocity above and below the separation point. Pressure waves expand in a domain where the direction of the propagation is not normal to any computational cell face. The test cases studied by El-Dosoky (2009) show the ability of the numerical method to perform well in the presence of contact discontinuities or non-normal pressure waves, indicating that the method is adequate for modelling the flow past a cylindrical cavity, where similar flow features are present.

3.3 Direct numerical simulation

3.3.1 Navier-Stokes equations

The time-dependent Navier-Stokes equations for a non-reactive adiabatic flow under no external force are:

$$\frac{\partial}{\partial t}\mathbf{U} + \nabla \cdot (\mathbf{F}_c + \mathbf{F}_v) = 0 \tag{3.31}$$

Equation (3.31) contains the conservative variables vector $\mathbf{U}$ and the inviscid flux vector $\mathbf{F}_c$ defined in equation (3.2). The viscous flux vector $\mathbf{F}_v$ is defined as:

$$\mathbf{F}_v = \begin{pmatrix} 0 \\ \tau \\ \tau \cdot \mathbf{u} - k_T \nabla T \end{pmatrix} \tag{3.32}$$

The viscous stress tensor $\tau = \mu_l (\nabla \mathbf{u} + \mathbf{u} \otimes \nabla - 2/3\mathbf{I}\nabla \cdot \mathbf{u})$, μ_l is the molecular viscosity, k_T the thermal conductivity and T is the absolute temperature. If $\mathbf{F}_v = 0$, equation (3.31) becomes equation (3.1).

The system of second-order partial differential equations (3.31) requires auxiliary algebraic relations for the molecular viscosity and the thermal conductivity that are modelled as:

$$\mu_l = 1.458 \times 10^{-6} \frac{T^{3/2}}{(T + 110.4)} \quad [\text{kg/ms}] \tag{3.33}$$

$$k_T = \frac{\gamma R \mu_l}{(\gamma - 1)\, Pr_l} \quad [\text{W/mK}] \tag{3.34}$$

where γ is the specific heat ratio, R is the specific gas constant and Pr_l is the Prandtl number.

3.3.2 Finite-volume viscous flux vector discretization

Applying the finite-volume approximation given in equation (3.7), the viscous flux vector $\mathbf{F}_v$ is modelled as

$$\oint_{S_i} \mathbf{F}_v \cdot \mathbf{n} \mathrm{d}S = \sum_{k=1}^{N_{faces}} \mathbf{F}_{v,k} \cdot \mathbf{n}_{i,k} S_{i,k} \tag{3.35}$$

Following the same discretization procedure as in section (3.2.2), the finite-volume discretized Navier-Stokes equations is equation (3.11) where the residual $\mathbb{R}_i$ is given by the sum of the two terms:

$$\mathbb{R}_i = \sum_{k=1}^{N_{faces}} \mathbf{F}_{c,k} \cdot \mathbf{n}_{i,k} S_{i,k} + \sum_{k=1}^{N_{faces}} \mathbf{F}_{v,k} \cdot \mathbf{n}_{i,k} S_{i,k} \tag{3.36}$$

To discretize the viscous fluxes, an estimate of the velocity vector gradients is required. To compute this, a staggered grid is built across the cell interfaces where these gradients are estimated. The flow state at the surface boundary of the new control volume and its normals are obtained from the mesh geometry and then the velocity vector gradient is estimated using the Gauss divergence theorem. This gives up to a second-order accurate reconstruction of the gradients (El-Dosoky, 2009).

3.3.3 Boundary conditions

In the direct numerical simulations, a no-slip condition is imposed at the physical wall boundaries and a subsonic non-reflective far-field boundary condition at the domain outer boundaries. At the inflow boundary of the cavity flow simulations, the laminar inflow profile of appendix A is used.

No-slip wall

The no-slip condition corresponds to $\mathbf{u} = \mathbf{0}$ at the boundary $S_{i,k}$ between the most interior cell and its ghost cell. This is numerically achieved by imposing $\mathbf{u}_b = -\mathbf{u}_{phy}$ in the ghost cell. The flow state at the ghost cell is:

$$\mathbf{U}_b = \begin{pmatrix} \rho_{phy} \\ -\rho\mathbf{u}_{phy} \\ \rho e_{phy} \end{pmatrix} \tag{3.37}$$

3.4 Detached Eddy Simulation

3.4.1 Governing equations

To reduce the computational effort in modelling high Reynolds number flows, the flow variables of DNS $\mathbf{u}$, that are varying in time and space, are split into two components, an averaged one $\overline{\mathbf{u}}$ and a fluctuating one $\mathbf{u}'$.

$$\mathbf{u} = \overline{\mathbf{u}} + \mathbf{u}' \tag{3.38}$$

Depending on the form of averaging adopted, two main-stream methods are developed to solve the Navier-Stokes equations: the Large Eddy Simulation (LES) method and the Reynolds-Averaged Navier-Stokes (RANS) method. In LES, the average is formally given by the convolution of the continuous variable $\mathbf{u}(\mathbf{y}, t)$ with a filtering kernel $\mathbf{G}(\mathbf{x}_i - \mathbf{y})$:

$$\overline{\mathbf{u}}(\mathbf{x}_i, t) = \int \mathbf{G}(\mathbf{x}_i - \mathbf{y})\, \mathbf{u}(\mathbf{y}, t)\, \mathrm{d}\mathbf{y} \tag{3.39}$$

To model the effects of the small eddies $\mathbf{u}'$ on the averaged flow, most industrial application in CFD use a sub-grid scale model (SGS) in which the filtering kernel is matched to the computational grid. The Yoshizawa (1986) one-equation LES model is based on this assumption to solve the large scales of motion. In such case, $\mathbf{G}$ is defined as the top-hat filter (Liu *et al.*, 2008) and is given by:

$$\mathbf{G}(\mathbf{x}_i - \mathbf{y})(\mathbf{x}) = \frac{1}{\Delta_i} H\left(\frac{\Delta_i}{2} - |\mathbf{x}_i - \mathbf{y}|\right) \tag{3.40}$$

where H is the heavy-side function, Δ_i is the filtering width of cell i, $\mathbf{x}_i$ is the cell centre position and $\mathbf{y}$ is the position vector. In the Yoshizawa one-equation LES model, Δ_i is the cubic root of the cell volume V_i, $\Delta = \sqrt[3]{V_i}$.
In RANS, the average $\bar{\mathbf{u}}$ is taken with respect to time. The short-time average Navier-Stokes equations are obtained by averaging in time τ over time interval Δt that is longer than the turbulent flow fluctuations and shorter than the flow variation not related to turbulence. This gives:

$$\bar{\mathbf{u}}(\mathbf{x}, n\Delta t) = \frac{1}{\Delta t}\int_{(n-1/2)\Delta t}^{(n+1/2)\Delta t} \mathbf{u}(\mathbf{x}, \tau)\,\mathrm{d}\tau \tag{3.41}$$

where $n \in \mathbb{N}$ and $\mathbb{N}$ is the set of all natural numbers.
Applying the average in equation (3.38) to the Navier-Stokes equations, given in section 3.3.1, they reduce to:

$$\frac{\partial\bar{\rho}}{\partial t} + \nabla\cdot\left(\overline{\rho\mathbf{u}}\right) = 0 \tag{3.42}$$

$$\frac{\partial\left(\overline{\rho\mathbf{u}}\right)}{\partial t} + \nabla\cdot\left(\overline{\rho\mathbf{u}}\otimes\bar{\mathbf{u}} + \bar{p}\mathbf{I} + \overline{\rho\mathbf{u}'\otimes\mathbf{u}'} - \bar{\tau}\right) = 0 \tag{3.43}$$

$$\frac{\partial\left(\overline{\rho e}_0 + \frac{1}{2}\overline{\rho\mathbf{u}'\cdot\mathbf{u}'}\right)}{\partial t} + \nabla\cdot\left(\overline{\rho\mathbf{u}}\bar{h}_0 + \bar{\mathbf{u}}\otimes\frac{1}{2}\overline{\rho\mathbf{u}'\cdot\mathbf{u}'}\right) = \nabla\cdot\left[\bar{\mathbf{u}}\cdot\left(\bar{\tau} - \overline{\rho\mathbf{u}'\otimes\mathbf{u}'}\right) - k_T\nabla\bar{T} - \overline{\rho\mathbf{u}'h'}\right] \tag{3.44}$$

In equation (3.44), $1/2\overline{\mathbf{u}'\cdot\mathbf{u}'}$ is the average turbulent kinetic energy $\bar{k}$. In equations (3.43) and (3.44), $\overline{\rho\mathbf{u}'\otimes\mathbf{u}'}$ is the Reynolds stress tensor. This is modelled by the Boussinesq approximation (Townsend, 1976) with analogy to viscous stress tensor as:

$$\bar{\mathbf{t}} = -\overline{\rho\mathbf{u}'\otimes\mathbf{u}'} = \mu_t\left(\nabla\bar{\mathbf{u}} + \bar{\mathbf{u}}\otimes\nabla - \frac{2}{3}\mathbf{I}\nabla\cdot\bar{\mathbf{u}}\right) - \frac{2}{3}\mathbf{I}\bar{\rho}\bar{k} \tag{3.45}$$

In equation (3.44), $\overline{\rho\mathbf{u}'h'}$ is the turbulent heat flux vector and it is modelled to be proportional to the temperature gradient (Wilcox, 2002):

$$\bar{\mathbf{q}}_t = \overline{\rho \mathbf{u}' h'} = -\frac{\mu_t C_p}{Pr_t} \nabla \bar{T} \tag{3.46}$$

The system of equations (3.42)-(3.44) is not closed due to the presence of the extra variables $\bar{k}$ and μ_t. To close this system, an additional equation is required that relates $\bar{k}$ to the other averaged variables. The derivation for $\bar{k}$ is obtained from the scalar product of the Navier-Stokes conservation of momentum vector equations multiplied by the fluctuating velocity vector $\mathbf{u}'$. Averaging this equation, the transport equation for $\bar{k}$ is:

$$\begin{aligned} \frac{\partial \left(\bar{\rho}\bar{k}\right)}{\partial t} + \nabla \left(\bar{\rho}\bar{\mathbf{u}}\bar{k} - \overline{\mathbf{t} \cdot \mathbf{u}'} + \frac{1}{2}\overline{\rho \mathbf{u}'\mathbf{u}' \cdot \mathbf{u}'} + \overline{p'\mathbf{u}'}\right) &= \\ -\overline{\rho \mathbf{u}' \cdot \mathbf{u}'}\nabla \cdot \bar{\mathbf{u}} - \overline{\mathbf{t} : \mathbf{u}' \otimes \nabla} - \overline{\mathbf{u}' \cdot \nabla p} + \overline{p' \nabla \cdot \mathbf{u}'} & \end{aligned} \tag{3.47}$$

The Yoshizawa (1986) one-equation SGS model is used to solve equation (3.47) in the LES model. Dahlström & Davidson (2003) proposed the following equations to model the transport equation of the kinetic energy:

$$\frac{\mathrm{D}\left(\bar{\rho}\bar{k}_{SGS}\right)}{\mathrm{D}t} = \bar{\mathbf{t}} : \bar{\mathbf{u}} \otimes \nabla - C_d \frac{\bar{\rho}\bar{k}_{SGS}^{3/2}}{\Delta} + \nabla \cdot \left[\left(\mu_l + \sigma_k \mu_{t,LES}\right) \nabla \bar{k}_{SGS}\right] \tag{3.48}$$

where $\mathrm{D}/\mathrm{D}t$ is the material operator $\mathrm{D}/\mathrm{D}t = \partial/\partial t + \bar{\mathbf{u}} \cdot \nabla$ and $\bar{\mathbf{t}}$ is the turbulent stress tensor, given by:

$$\bar{\mathbf{t}} = \mu_{t,LES} \left(\nabla \bar{\mathbf{u}} + \bar{\mathbf{u}} \otimes \nabla - \frac{2}{3} \nabla \cdot \bar{\mathbf{u}} \mathbf{I}\right) - \frac{2}{3} \bar{\rho} \bar{k}_{SGS} \mathbf{I} \tag{3.49}$$

The eddy viscosity $\mu_{t,LES}$ is given by:

$$\mu_{t,LES} = \bar{\rho} C_s \Delta \sqrt{\bar{k}_{SGS}} \tag{3.50}$$

In equations (3.48) and (3.50), C_s and C_d are the Yoshizawa constants and are related to the Smagorinsky constant by:

$$C_{smag} = \left(\frac{C_s^3}{C_d}\right)^{0.25} \tag{3.51}$$

The Smagorinsky constant ranges from 0.065 to 0.2 and in this work is taken $C_{smag} = 0.1$. The corresponding Yoshizawa constants used in this model are $C_s = 0.046$, $C_d = 1.0$, and $\sigma_k = 1.0$.

In the RANS model used in this work, two equations are defined to close equations (3.42)-(3.44) and (3.47). Two mainstream closure models are used in RANS, these are the $k-\epsilon$ and the $k-\omega$ models, depending on the equation that is used to solve equation (3.47). In this equation, the viscous dissipation of turbulent shear stress $\overline{\mathbf{t} : \mathbf{u}' \otimes \nabla}$ is proportional to the average dissipation rate per unit mass $\overline{\epsilon}$:

$$\overline{\mathbf{t} : \mathbf{u}' \otimes \nabla} = \overline{\rho\epsilon} = \mu_l \overline{\nabla\mathbf{u}' : \nabla\mathbf{u}'} \tag{3.52}$$

The same term can also be written in terms of the average specific turbulence dissipation rate ω and the average turbulent kinetic energy $\overline{k}$ as:

$$\overline{\mathbf{t} : \mathbf{u}' \otimes \nabla} = \beta^* \overline{\rho}\overline{k}\overline{\omega} \tag{3.53}$$

Menter (1992) developed a shear stress transport model (SST) that combined the qualities of the two RANS models into the $k-\omega$-SST model, which is the RANS model used in this work. Its derivation is reported in El-Dosoky (2009). This model gives more accurate results in regions of separated flow and it is more suitable to model cavity flow than the standard $k-\omega$ model of Wilcox (2002).

The $k-\omega$-SST closure model is given by:

$$\frac{\mathrm{D}\left(\overline{\rho}\overline{k}_{RANS}\right)}{\mathrm{D}t} = \overline{\mathbf{t}} : \overline{\mathbf{u}} \otimes \nabla - \beta^* \overline{\rho}\overline{k}_{RANS}\overline{\omega} + \nabla \cdot \left[\left(\mu_l + \sigma_k \mu_{t,RANS}\right) \nabla\overline{k}_{RANS}\right] \tag{3.54}$$

$$\frac{\mathrm{D}\left(\overline{\rho}\overline{\omega}\right)}{\mathrm{D}t} = \gamma\overline{\rho}\overline{\mathbf{t}} : \overline{\mathbf{u}} \otimes \nabla - \beta^* \overline{\rho}\overline{\omega}^2 + \nabla \cdot \left[\left(\mu_l + \sigma_\omega \mu_{t,RANS}\right) \nabla\overline{\omega}\right] \quad +$$

$$\left(1 - F_1\right) \underbrace{2\overline{\rho}\sigma_{\omega 2}\frac{1}{\overline{\omega}}\nabla\overline{k}_{RANS} \cdot \nabla\overline{\omega}}_{\text{Cross-diffusion term}} \tag{3.55}$$

	σ_k	σ_ω	β	β^*	γ
$k-\omega$, 1	0.85	0.5	0.075	0.09	$\frac{\beta_1}{\beta^*} - \frac{\sigma_{\omega 1}\kappa^2}{\sqrt{\beta^*}}$
$k-\epsilon$, 2	1.0	0.856	0.0828	0.09	$\frac{\beta_2}{\beta^*} - \frac{\sigma_{\omega 2}\kappa^2}{\sqrt{\beta^*}}$

Table 3.1: Turbulence closure model coefficients.

where $\overline{\mathbf{t}}$ is given by equation (3.49) substituting $\overline{k}_{SGS}$ with $\overline{k}_{RANS}$. The blending function F_1 is used to couple the constants used in the $k-\omega$ and the $k-\epsilon$ models:

$$\begin{pmatrix} \sigma_k \\ \sigma_\omega \\ \beta \\ \gamma \end{pmatrix} = F_1 \begin{pmatrix} \sigma_{k1} \\ \sigma_{\omega 1} \\ \beta_1 \\ \gamma_1 \end{pmatrix} + (1-F_1) \begin{pmatrix} \sigma_{k2} \\ \sigma_{\omega 2} \\ \beta_2 \\ \gamma_2 \end{pmatrix} \tag{3.56}$$

The constants are given in table 3.1 and $\kappa = 0.41$ is the Von Kármán constant. The compound subscript in the constants designates the model in table 3.1, for instance, $\sigma_{k1} = 0.85$.
The blending function F_1 is given by:

$$F_1 = \tanh\left\{\min\left[\max\left(\frac{\sqrt{\overline{k}_{RANS}}}{0.09\overline{\omega}y}, \frac{500\mu_l}{\overline{\rho}\overline{\omega}y^2}\right), \frac{4\overline{\rho}\sigma_{\omega 2}\overline{k}_{RANS}}{CD_{k\omega}y^2}\right]\right\}^4 \tag{3.57}$$

$$CD_{k\omega} = \max\left(2\overline{\rho}\sigma_{\omega 2}\frac{1}{\overline{\omega}}\nabla\overline{k}_{RANS} \cdot \nabla\overline{\omega}, 10^{-20}\right) \tag{3.58}$$

where y is the distance from the closest wall to the cell center.
The turbulent eddy viscosity $\mu_{t,RANS}$ is given by:

$$\mu_{t,RANS} = \frac{\overline{\rho}\alpha_1\overline{k}_{RANS}}{\max\left(\alpha_1\overline{\omega}, \left|\mathbf{S}_{ij}\right| F_2\right)} \tag{3.59}$$

where $\alpha_1 = 0.31$ and $\left|\mathbf{S}_{ij}\right|$ is the magnitude of the strain rate tensor $\mathbf{S}_{ij} = 1/2\left(\nabla\overline{\mathbf{u}} + \overline{\mathbf{u}} \otimes \nabla\right)$.

The function F_2 is defined as:

$$F_2 = \tanh\left[\max\left(2\frac{\sqrt{k_{RANS}}}{0.09\overline{\omega}y}, \frac{400\mu_l}{\overline{\rho}\overline{\omega}y^2}\right)\right] \tag{3.60}$$

Carefully considering the different averaging in the LES given by equation (3.39) and in the RANS models given by equation (3.41), it is possible to blend the two models into a Detached Eddy Simulation (DES). The aim is to overcome the constraint of the LES model in the near-wall region by switching to the less computationally expensive RANS model.

The transport equation for the turbulent kinetic energy can be written as:

$$\frac{\mathrm{D}\left(\overline{\rho}\overline{k}\right)}{\mathrm{D}t} = \overline{\mathbf{t}} : \overline{\mathbf{u}} \otimes \nabla - \left[\Gamma\beta^*\overline{\rho}\overline{k}\overline{\omega} + (1-\Gamma)\, C_d \frac{\overline{\rho}\overline{k}^{3/2}}{\Delta}\right] + \nabla \cdot \left[(\mu_l + \sigma_k\mu_t)\, \nabla\overline{k}\right] \tag{3.61}$$

where the eddy viscosity is obtained by blending the eddy viscosity from the LES model of equation (3.50) and the RANS model of equation (3.59):

$$\mu_t = \Gamma\mu_{t,RANS} + (1-\Gamma)\, \mu_{t,LES} \tag{3.62}$$

The blending function Γ is defined as:

$$\Gamma = \tanh\left[\max\left(\frac{\sqrt{k}}{0.09\overline{\omega}y}, \frac{500\mu_l}{\overline{\rho}\overline{\omega}y^2}\right)\right]^4 \tag{3.63}$$

Let $\Gamma(y \to 0) = \lim_{y\to 0} \Gamma$ be the value that the blending function takes in the close wall region. By applying De L'Hopital's theorem to equation (3.63), in the limit of $y \to 0$, $\tanh(\infty) \to 1$ and $\Gamma(y \to 0) \to 1$. Depending on the value of Γ, three regions are identified: a RANS region where $\Gamma \to 1$ and equations (3.54) and (3.55) are recovered and $\overline{k} \equiv \overline{k}_{RANS}$, a LES region where equation (3.48) is recovered and $\overline{k} \equiv \overline{k}_{LES}$, and finally a so-called interface-region where the two model contribute to solve equation (3.61).

The $\overline{\omega}$ transport equation (3.55) is solved in all three regions to guarantee continuity in the computation but its result is not used in the LES region.

Equations (3.42), (3.43), (3.44), (3.55) and (3.61) can be rearranged in the compact form:

$$\frac{\partial}{\partial t}\mathbf{U} + \nabla \cdot (\mathbf{F}_c + \mathbf{F}_v) + \mathbf{S} = 0 \tag{3.64}$$

where the conservative variable vector $\mathbf{U}$, the convective flux vector $\mathbf{F}_c$, the turbulent flux vector $\mathbf{F}_v$ and the turbulent source term vector $\mathbf{S}$ are given by Chen-Chuan Fan (2002) as:

$$\mathbf{U} = \begin{pmatrix} \bar{\rho} \\ \bar{\rho}\bar{\mathbf{u}} \\ \bar{\rho}\left(\bar{e} + \bar{k}\right) \\ \bar{\rho}\bar{k} \\ \bar{\rho}\bar{\omega} \end{pmatrix} \tag{3.65}$$

$$\mathbf{F}_c = \begin{pmatrix} \bar{\rho}\bar{\mathbf{u}} \\ \bar{\rho}\bar{\mathbf{u}} \otimes \bar{\mathbf{u}} + \bar{p}\mathbf{I} \\ \bar{\rho}\bar{\mathbf{u}}\left(\bar{e} + \bar{p}/\bar{\rho} + \bar{k}\right) \\ \bar{\rho}\bar{\mathbf{u}}\bar{k} \\ \bar{\rho}\bar{\mathbf{u}}\bar{\omega} \end{pmatrix} \tag{3.66}$$

$$\mathbf{F}_v = \begin{pmatrix} 0 \\ -\left(\bar{\mathbf{t}} + \bar{\tau}\right) \\ -\bar{\mathbf{q}} - \bar{\mathbf{q}}_t - \left(\bar{\mathbf{t}} + \bar{\tau}\right) \cdot \bar{\mathbf{u}} - \left(\mu_l + \sigma_k \mu_t\right) \nabla \bar{k} \\ -\left(\mu_l + \sigma_k \mu_t\right) \nabla \bar{k} \\ -\left(\mu_l + \sigma_\omega \mu_t\right) \nabla \bar{\omega} \end{pmatrix} \tag{3.67}$$

$$\mathbf{S} = \begin{pmatrix} 0 \\ \mathbf{0} \\ 0 \\ \Gamma\beta^* \bar{\rho}\bar{k}\bar{\omega} + \left(1 - \Gamma\right) C_d \rho \bar{k}^{3/2}/\Delta - \bar{\mathbf{t}} : \nabla\bar{\mathbf{u}} \\ \beta\bar{\rho}\bar{\omega}^2 + 2\left(1 - F_1\right)\left(\bar{\rho}\sigma_{\omega 2}\nabla\bar{k}_{RANS} \cdot \nabla\bar{\omega}\right)/\bar{\omega} - \gamma\bar{\rho}\bar{\mathbf{t}} : \bar{\mathbf{u}} \otimes \nabla \end{pmatrix} \tag{3.68}$$

3.4.2 Finite-volume source term vector discretization

Applying equation (3.7) to the source vector $\mathbf{S}$ in equation (3.64), it becomes

$$\mathbf{S}_i = \frac{1}{V_i} \int_{V_i} \mathbf{S} \mathrm{d}V \tag{3.69}$$

To solve the RANS/LES turbulent model, the residual $\mathbb{R}_i$ in equation (3.11) is given by the sum of the flux vectors in equation (3.10) and (3.35) and the source terms of equation (3.69):

$$\mathbb{R}_i = \sum_{k=1}^{N_{faces}} \mathbf{F}_{c,k} \cdot \mathbf{n}_{i,k} S_{i,k} + \sum_{k=1}^{N_{faces}} \mathbf{F}_{v,k} \cdot \mathbf{n}_{i,k} S_{i,k} + V_i \mathbf{S}_i \tag{3.70}$$

The gradients in equation (3.68) are computed with the same approach as in section 3.3.2. It is important to notice that the present model is driven by a mesh based eddy viscosity μ_t related to the cell volume by the definition of the averaging in equation (3.39). In the RANS region the turbulent production term $\overline{\mathbf{t} : \mathbf{u}' \otimes \nabla}$ is saturated with an upper-bound term equivalent to 20 times the destruction term $\beta^* \overline{\rho} \overline{\omega} \overline{k}$. Menter (1992) introduced this correction to prevent the unrealistic built-up of eddy viscosity during the computation.

3.4.3 Boundary Conditions

Wall model

Consider the following relation for the first interior cell *phy*:

$$u_n = \overline{\mathbf{u}}_{phy} \cdot \mathbf{n} \tag{3.71}$$

$$u_t = \left| \overline{\mathbf{u}}_{phy} - u_n \mathbf{n} \right| \tag{3.72}$$

where u_n is the signed normal of the velocity component normal to the solid wall and u_t is the norm of the tangential velocity component. The following relation are applied at the solid wall:

$$\bar{T}_{sw} = \bar{T}_{phy}\left(1 + Pr_t \frac{\gamma - 1}{2\gamma R\bar{T}_{phy}} \bar{\mathbf{u}}_{phy} \cdot \bar{\mathbf{u}}_{phy}\right) \tag{3.73}$$

$$\bar{\rho}_{sw} = \frac{\bar{p}_{phy}}{R\bar{T}_{sw}} \tag{3.74}$$

$$\mu_l = 1.458 \times 10^{-6} \frac{\bar{T}_{sw}^{3/2}}{\left(\bar{T}_{sw} + 110.4\right)} \tag{3.75}$$

where $\bar{T}_{sw}$ is the adiabatic wall temperature, $Pr_t = 0.89$ is the turbulent Prandtl number, $\bar{\rho}_{sw}$ is the corresponding wall adiabatic density and μ_l the corresponding molecular viscosity.

The third order approximate law of the wall by Spalding (1961) is used to estimate the friction velocity u_τ at the first interior point:

$$f\left(y^+, u^+\right) = u^+ - y^+ + \exp\left(-\kappa B\right)\left[\exp\left(\kappa u^+\right) - 1 - \kappa u^+ - \frac{\left(\kappa u^+\right)^2}{2} - \frac{\left(\kappa u^+\right)^3}{6}\right] \tag{3.76}$$

where $\kappa = 0.41$ and $B = 5.0$ are the Von Kàrmàn constants (Österlund, 1999).

It is assumed that the first interior cell satisfies equation (3.76), therefore the following relations are used:

$$y^+ \equiv y^+_{phy} = \frac{\bar{\rho}_{sw} y u_t}{\mu_l u^+_{phy}} \tag{3.77}$$

$$u^+ \equiv u^+_{phy} \tag{3.78}$$

These lead to the following equation:

$$f\left(u^+_{phy}\right) = 0 \tag{3.79}$$

Equation (3.79) is solved using the Newton-Raphson method (Householder, 1953) to estimate the value of u^+_{phy}. u_τ is given by:

$$u_\tau = \frac{u_t}{u^+_{phy}} \tag{3.80}$$

The value of y^+_{phy} is calculated using equation (3.77). Depending on the value of y^+_{phy}, the wall model boundary condition switches between a no-slip boundary condition region, and a law of the wall boundary condition. The limit between the two conditions is chosen to be $y^+_{phy} \leq 4.7$, that corresponds to the laminar sublayer thickness in a fully developed turbulent boundary layer under a zero pressure gradient (Schlichting, 1968). At $y^+_{phy} \leq 4.7$, in the no-slip condition the ghost cell flow state b is:

$$\bar{\rho}_b = \bar{\rho}_{sw} \tag{3.81}$$

$$\bar{\mathbf{u}}_b = -\bar{\mathbf{u}}_{phy} \tag{3.82}$$

$$\bar{k}_b = 0 \tag{3.83}$$

$$\bar{\omega}_b = \frac{60\mu_{l,phy}}{\beta y^2} \tag{3.84}$$

Menter (1992) gave the limit values for $\bar{k}$ and $\bar{\omega}$ as $y^+ \rightarrow 0$ of equations (3.83) and (3.84). $\bar{\rho}_{sw}$ is given from equation (3.74) and β from equation (3.56).
At $y^+_{phy} > 4.7$, the wall model by Rona & Brooksbank (2002) is used to evaluate the ghost cell tangential velocity correction $\widetilde{u}$:

$$\widetilde{u} = \widetilde{z} + \left(\frac{1-\widetilde{z}}{\kappa u^+}\right) \tag{3.85}$$

$$\widetilde{z} = \exp - \max\left[0, \left(\frac{y^+_{phy} - 5}{20}\right)\right] \tag{3.86}$$

From $\widetilde{u}$, the ghost cell flow state b in the wall model condition is:

$$\bar{\rho}_b = \bar{\rho}_{sw} \tag{3.87}$$

$$\bar{\mathbf{u}}_b = \left(\bar{\mathbf{u}}_{phy} - u_n\mathbf{n}\right)(1-2\widetilde{u}) - u_n\mathbf{n} \tag{3.88}$$

$$\bar{k}_b = \frac{u_\tau^2}{\sqrt{\beta^*}} \tag{3.89}$$

$$\bar{\omega}_b = \sqrt{\frac{\bar{T}_{phy}}{\bar{T}_{sw}}}\frac{u_\tau}{\beta^{*3/4}\kappa y} \tag{3.90}$$

where $\bar{k}_b$ and $\bar{\omega}_b$ are obtained from a compressible near wall approximation by Wilcox (2002), u_τ is from equation (3.80), and $\bar{T}_{sw}$ is from equation (3.73). κ is the Von Kàrmàn constant and β^* is given in table 3.1.
The wall distance of the first interior cell strongly affects the predicted boundary layer

velocity at the first interior cell, via equation (3.88). In an under-resolved mesh, where $y^+_{phy} \approx 30$, the resulting profile may lead to an under estimate of the velocity profile momentum thickness and its growth rate, leading to difficulties in estimating skin friction drag and surface heat transfer. To prevent such difficulties, a mesh refined test case, discussed in section 6.4, has a computational grid designed to a value of $y^+_{phy} \approx 10$. The small value of y^+_{phy} leads to $\widetilde{z} \approx 1$ and equation (3.88) returns $\bar{\mathbf{u}}_b = -\bar{\mathbf{u}}_{phy}$. This produces a non-physical flow re-laminarization. To avoid this condition a different model is implemented. This model estimates the value of the ghost cell tangential velocity to account for a second-order velocity gradient correction in the wall normal direction.
Let the tangential velocity vector $\mathbf{u}_t$ and its normal be defined as:

$$\mathbf{u}_t = \mathbf{u}_{phy,1} - u_n \mathbf{n} \tag{3.91}$$

$$\mathbf{e}_t = \frac{\mathbf{u}_t}{|\mathbf{u}_t|} \tag{3.92}$$

where index 1 indicates the first interior cells. Assuming that the tangential velocity satisfy the log law of the wall by Von Kármán (1954), a tangential velocity component u_{bt} is defined by

$$u_{target} = u_\tau \left(\frac{1}{\kappa} \ln \left(\frac{y^+_{phy,1} + y^+_{phy,2}}{2} \right) + B \right) \tag{3.93}$$

$$u_{bt} = u_{target} - u_\tau \frac{2}{\kappa} \frac{y^+_{phy,2} - y^+_{phy,1}}{y^+_{phy,2} + y^+_{phy,1}} \tag{3.94}$$

where index 2 indicates the second interior cells.
At $y^+_{phy} > 4.7$, equation (3.88) is replaced by

$$\mathbf{u}_b = u_{bt} \mathbf{e}_t - u_n \mathbf{n} \tag{3.95}$$

Non-reflective far-field extension

The non-reflective far-field boundary condition of section 3.2.3 is extended to include a condition for k and ω. A simple zeroth-order extrapolation is used. For the inflow condition ($\mathbf{u}_S \cdot \mathbf{n} \geq 0$), $k_b = k_\infty$ and $\omega_b = \omega_\infty$, whereas for the outflow condition ($\mathbf{u}_S \cdot \mathbf{n} < 0$), $k_b = k_{phy}$ and $\omega_b = \omega_{phy}$.

3.4.4 Validation

El-Dosoky (2009) validated the viscous flow solver against the three-dimensional complex flow that occurs near a wing-body junction. The flow exhibits large streamwise vortical structures that affect the wall boundary layers. A horseshoe vortex develops at the junction and grows further downstream. Detailed experimental data are available in the ERCOFTAC database (Devenport & Simpson (1990) and Fleming *et al.* (1993)) under case number 8. The measurements includes the mean velocity and all Reynolds stresses at several streamwise and flow-normal positions. This test case is a good candidate to validate the flow solver and its application to the present test case. The interaction between the approaching boundary layer and the wing-body results into a three-dimensional vortex that grows along the streamwise direction. Although the configuration results into a steady flow and conventional RANS model can be used, the time-dependent flow model gave predictions with a level of detail similar to the ones obtained using a full Reynolds stress model or second order moment closure, as stated by El-Dosoky (2009).
An unsteady horseshoe vortex can be found downstream of the circular cavity edge as found experimentally by Gaudet & Winter (1973) in a deep cylindrical cavity flow. A steady horseshoe vortex was also found in a shallow closed cylindrical cavity in the upstream corner. Gaudet & Winter (1973) also make the hypothesis that two counter-rotating vortices are shed corresponding to the cavity downstream edge. The numerical model needs to be able to capture the vortex growth rate as well as vortex core position with a suitable engineering accuracy. These aspects were tackled by El-Dosoky (2009) in the wing-body junction test case.

3.5 Time integration

To solve the discrete ordinary differential vector equation (3.11), an explicit multi-stage time step integration is used. This scheme is numerically cheap, requires a small computational memory and is designed to preserve the total variation diminishing properties of the spatial differentiation scheme. It is implemented as follows:

$$
\begin{aligned}
&\mathbf{U}_i^0 = \mathbf{U}_i^n \\
&\text{FOR } k = 1, m \\
&\quad \mathbf{U}_i^k = \mathbf{U}_i^0 - 1/\left(m-k+1\right)\Delta t / V \mathbb{R}^{k-1} \\
&\text{END} \\
&\mathbf{U}_i^{n+1} = \mathbf{U}_i^m
\end{aligned}
\tag{3.96}
$$

where m denotes the number of stages of the Runge-Kutta scheme and n the time level. The stability of this scheme is restricted by the Courant, Friedrichs & Lewy (1928) condition.

3.6 Combining the short-time RANS average and the LES average in the RANS/LES model

LES and RANS variables can be combined in hybrid schemes under certain conditions that relate to the scheme's spatial and temporal discretization.
Applying equation (3.9) to a flow state variable $f(\mathbf{y}, \tau)$ and taking the LES average of equation (3.39) gives:

$$
\begin{aligned}
&\frac{1}{V_i}\int_{V_i}\int \frac{1}{\Delta} H\left(\frac{\Delta}{2} - |\mathbf{x}_i - \mathbf{y}|\right) f(\mathbf{y}, \tau)\,\mathrm{d}\mathbf{y}\mathrm{d}V = \\
&\qquad \int_{V_i} \frac{1}{\Delta}\langle f\rangle \Delta \mathrm{d}V = \frac{1}{V_i}\left\langle \overline{f}\right\rangle V_i = \left\langle \overline{f}(\mathbf{x}_i, \tau)\right\rangle
\end{aligned}
\tag{3.97}
$$

Where $\left\langle \overline{f}\right\rangle$ is the volume average over $V_i = \Delta x \Delta y \Delta z$ of the filtered variable $\langle f\rangle$, $\langle f\rangle$ is $f(\mathbf{y}, \tau)$ filtered over the filtering length $\Delta = \sqrt[3]{V_i}$, and $\mathbf{x}_i$ is the cell center.
Let V_i be a near-cubic cell. The filtering length in this cell is

$$
\Delta = \sqrt[3]{\Delta x \Delta y \Delta z} \approx \Delta x \approx \Delta y \approx \Delta z \tag{3.98}
$$

In this cell, $\left\langle \overline{f} \right\rangle = \langle f \rangle$ if a top hat filter is used. Let

$$\hat{f}(\mathbf{x}_i, t) \stackrel{\text{def}}{=} \left\langle \overline{f}(\mathbf{x}_i, t) \right\rangle \approx \langle f(\mathbf{x}_i, t) \rangle \approx \overline{f}(\mathbf{x}_i, t) \tag{3.99}$$

Sampling at a generic time $n\Delta t$, where n is a natural number and Δt is a finite time step gives

$$\hat{f}(\mathbf{x}_i, n\Delta t) \stackrel{\text{def}}{=} \int \hat{f}(\mathbf{x}_i, \tau)\, \delta(n\Delta t - \tau)\, \mathrm{d}\tau \tag{3.100}$$

where δ is the Dirac delta function. $\hat{f}(\mathbf{x}_i, n\Delta t)$ is the finite-volume time-discrete LES average of $f(\mathbf{y}, \tau)$.
Applying equation (3.9) to a flow state variable $f(\mathbf{y}, \tau)$ and taking the RANS average of equation (3.41), it follows:

$$\begin{gathered} \frac{1}{V_i}\frac{1}{\Delta t}\int_{V_i}\int f(\mathbf{y}, \tau)\, \mathrm{d}t\mathrm{d}V = \\ \frac{1}{\Delta t}\int \left(\frac{1}{V_i}\int_{V_i} f(\mathbf{y}, \tau)\, \mathrm{d}V\right)\mathrm{d}\tau = \frac{1}{\Delta t}\int \overline{f}(\mathbf{x}_i, \tau)\, \mathrm{d}\tau \end{gathered} \tag{3.101}$$

where Δt in equation (3.101) coincides with the time step and is called short time average.
Substitute equation (3.99) into equation (3.101) at time $n\Delta t$.
Equations (3.100) and (3.101) can be applied to any conservative variable of the conservative variable vector $\mathbf{U}$ but the non-linear terms related to $\mathbf{u}'$ and its gradient are modelled in different ways. Keating *et al.* (2006) discussed the importance of the modelling of the interface RANS/LES region and its implication in favourable, adverse, and zero-pressure gradient turbulent boundary layer channel flow simulations. In the interface region, a controlled forcing mechanism was introduced to enhance the production terms in the computation of the shear-stress. The model used in this thesis does not implement such control.

3.7 Data format and post-processing

The CFD data are stored in a compact, binary file to facilitate the exchange of data between sites and applications, and to help stabilize the archiving of aerodynamic data.

The CFD General Notation System (CGNS) is an open source software. It is self-descriptive, well-documented, and administered by an international steering committee since 1999 (Bush *et al.*, 2007). This steering committee is made up of international representatives from government and private industry. It is also an American Institute of Aeronautics and Astronautics (AIAA) Recommended Practice.
Data stored in CGNS format are proven to be long lasting, easy to store, easy to share between sites and collaborators, and easily extensible to include almost any type of additional data.
CGNS data are generally associated with compressible viscous flow (i.e., the Navier-Stokes equations), but the standard is also applicable to sub-sets such as inviscid and potential flows. The CGNS standard includes the following types of data:

1. Structured, unstructured, and hybrid grids. This work uses structured grids.
2. Flow solution data, which may be nodal, cell-centred, face-centred, or edge-centred. This work uses cell-centred solution data.
3. Multi-zone interface connectivity, both one to one and over-set. This work uses the one to one connectivity.
4. Boundary conditions.
5. Flow model specification, including the equation of state, viscosity and thermal conductivity models, turbulence models, multi-species chemistry models, and electromagnetics. In this work, the equation of state, the viscous and thermal conductivity models, and the turbulence models are specified.
6. Time-dependent flow, including moving and deforming grids. This work uses the time-dependent flow option only.
7. Dimensional units and non-dimensionalization information. This work uses the standard international units and a dimensional model.
8. Reference states.
9. Convergence history.
10. User-defined data.

The CGNS standards have been recently extended to take advantage from a parallel input/output interface. Hauser (2008) proposes a new parallel interface and provides a prototype implementation of the CGNS libraries. He also provides some preliminary evaluation performance of the parallel output file system developed increasing the number of zones to be written. A beta version is available under the latest CGNS libraries version 2.5.
The in-house CFD code employs a scalar version of the CGNS libraries, version 2.4. It was therefore necessary to develop a parallel data distribution and gathering architecture within the CFD code for the parallel runs. This is documented in section 4.3.

3.8 Conclusion

This chapter described the numerical models used to study the cylindrical cavity flow. The validation of the flow solver done by El-Dosoky (2009) showed the ability of the numerical method to capture the contact discontinuities and pressure waves propagating oblique to the computational mesh. The method is found adequate to model the flow past a cylindrical cavity, where similar flow features are present. The horseshoe vortex found in the interaction between an approaching boundary layer and the wing-body in the DES simulation by El-Dosoky (2009) can also be found downstream the cylindrical cavity circular edge. The turbulent model herein proposed is expected to describe the flow unsteadiness in the cylindrical cavity test case.

Chapter 4

Code parallelization using MPI

4.1 Introduction

This chapter describes the parallelization algorithm used in the flow solver. Two different approaches have been implemented: a single domain decomposition and a recursive domain decomposition. The performance of the two algorithm are studied by means of the parallelization efficiency and the speed-up.

4.2 Single domain decomposition

The computational domain is built as an assembly of individual three-dimensional, curvilinear and topologically orthogonal in the (i, j, k) computational zones. A two cell deep layer of ghost cells surrounds each zone where outer zone connectivity information is updated at each Runge-Kutta time integration. Zones with updated ghost cells are independent and can be integrated in parallel.

As described in section 2.7, multi-processors HPC clusters are nowadays extensively used to solve CFD problems. Specifically medium $\left(\leq 20 \times 10^6 \text{cells}\right)$ and large $\left(> 30 \times 10^6 \text{cells}\right)$ CFD test cases cannot be run without modern HPC facilities. The two main stream parallelization methods are Message Passing Interface (MPI) and Open Multi-Processing (OMP). MPI for code parallelization is highly recommended with respect to OMP because it is more flexible and does not need a shared-memory cluster. The flow solver is parallelized using MPI and it was tested on two distributed-memory HPC clusters.

Considering a single zone of computational domain, given the number of processors available in the cluster, each zone is sliced into blocks along k, hence the name single domain decomposition (SDD). The k-direction is chosen as it coincides with the outermost variable pointer for a given zone in the FORTRAN programming language, such as for $U(i, j, k)$. Variables belonging to a k-slice are contiguous in memory and are faster to be sent and received among other processors, as they do not need buffering. During the initialization of a test-case, three MPI_TYPE arrays are defined to reduce the overhead related to exchanging data across the distributed memory architecture, respectively for k, j and an i planes. In the most general case, each processor sends and receives four k-planes during each Runge-Kutta time step as well as the relevant contour of j-plane and i-plane data. The latter originates from the multi-block connectivity.

SDD was implemented using MPI assuming the processor memory to be sufficient to include all the computational variables of all zones of the CFD problem during run time. SDD can also be implemented using OMP on shared-memory cluster but works for small CFD computations on the distributed memory platforms used in this work.

Figure 4.1 shows a simple 2D domain divided into three computational blocks. A blue dashed edge, a red continuous edge and a black dash-dot edge are used to identify these zones that are denoted as zone 1, 2 and 3. The k-direction coincides with the vertical direction in this example. The zones are evenly sized but have different aspect ratios, giving a different number of cells along the k-direction. In this example, only two processors, 0 and 1, are used. A dotted line separates the computational blocks computed by processors 0 and 1 respectively. To compute the convective fluxes using the flow solver, as described in paragraph 3.2.2, four contiguous cells are needed in all directions. Green hashing is used in figure 4.1 to highlight the data that are transferred from processor 0 to processor 1 at each Runge-Kutta step (see section 3.5). In this example, a symmetric situation characterizes the processor 1. All the cells of zone 1, computed by processor 0, are transferred to processor 1 and all the cell of processor 1 of zone 2 are transferred to processor 0. This is a bottleneck situation for the SDD implementation, as processors 0 and 1 spend more time in exchanging ghost cells information than in doing the computation.

SDD is generally representative of the best parallelization strategy for a low number of zones that are characterized by a large number of cells.

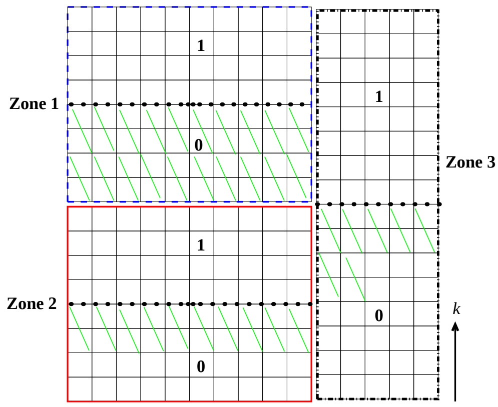

Figure 4.1: Exchanged cells between processor 0 and processor 1 in green.

4.3 Recursive domain decomposition

SDD required a large memory consumption and its inter-block communication overhead limits it to a small CFD computation. Recent HPC clusters are assembled to minimize the communication time among processors but computer cores do not have more memory than an ordinary home desktop. Nowadays shared memory cluster are also being replaced by large distributed memory HPC clusters. To use these clusters to their full potential a more complex parallelization strategy is implemented.

In a recursive domain decomposition (RDD), the computational domain is built by an assembly of three-dimensional, curvilinear and topologically orthogonal zones (i, j, k), like SDD. In RDD, each zone is a unit that is allocated to a selected group (or sub-cluster) of processors to compute it. Each unit is then sliced over k planes and thus distributed to each processor in this sub-cluster. The memory allocation benefits from the division of the computational domain in these units.

As described in paragraph 2.7, independent operations represent one of the enablers for code parallelization. If possible, it is important to implement asynchronous input and output interfaces to reduce the overall computational time.

To take advantage of the multi-zone division, the input to the computation is divided into three parts:

i Sequential reading of the size of each zone. The zone size is broadcast to all processors.

Table 4.1: RDD code variables

Communication Handler	MPI_COMM_WORLD	block_comm	master_comm
Identifier	*myproc*	*myproc_block*	*myproc_master*
Number of processors	*nprocs*	*nprocs_block*	*nprocs_master*

ii Asynchronous reading of the zone geometry and flow data. This data is shared only among the processors allocated to one or the other zone.

iii Sequential reading of the connectivity and the boundary conditions of all the zones.

Each sub-cluster of processors is defined by this procedure to optimize the load balance with respect to the ratio of the total number of cells over the total number of processors. Two communicators different from the default MPI_COMM_WORLD are defined to reduce the communication overhead: a block communicator and a master communicator. The communicators are block_comm and master_comm as stated in table 4.1.

The block communicator allows the information to be exchanged in the group dedicated to compute each zone. This causes the code to scale better with increasing number of blocks than SDD, within limits.

The master communicator is used to exchange the connectivity information among the zones. This is then simultaneously sent to all the processors of each group.

The solution is written in CGNS format and the writing is sequential in processor 0 only.

Let *nprocs* be the total number of processors allocated to the problem and *nzones* be the total number of computational zones that divide the computational domain. A processor cluster of size *nprocs_block* is allocated to each zone depending on its total number of cell to achieve load balance. In each group of blocks, the processor $myproc\_block \equiv 0$ define the block master and is univocally identified using *myproc_master* in master_comm. The following relations characterize the variables in table 4.1:

$$0 \leq myproc \leq nprocs - 1 \tag{4.1}$$

$$nprocs\_master \leq nzones \tag{4.2}$$

$$nprocs\_block \leq nprocs \tag{4.3}$$

Equation 4.1 is the standard relation that characterize the MPI standard communicator MPI_COMM_WORLD and it is extended also to block_comm and master_comm as:

$$0 \leq myproc\_block \leq nprocs\_block - 1 \tag{4.4}$$

$$0 \leq myproc\_master \leq nprocs\_master - 1 \tag{4.5}$$

Equation 4.2 reduces to $nprocs\_master = nzones$ if $nprocs > nzones$. This condition is generally satisfied for medium and large CFD problems, where the computational domain is divided into different zones but it is not required in the implemented RDD.
Equation 4.3 reduces to $nprocs\_block = nprocs$, only if $nzones = 1$. If the all computational domain is not divided into zones than RDD coincides with SDD.
Table 4.2 gives the code implementation of RDD. The variables are those in table 4.1. $left$ and $right$ are respectively the previous and the next processor to a generic processor $myproc\_block$ of a generic group.
As each zone is a separate from any other and no data are stored in the processors of a given cluster of the zone, a zone interface must be defined in all processor to gather the connectivity information of other zones. To minimize the time to create and exchange this zone interface array, the data are first exchanged across masters and then across the blocks as described in the pseudo-code of table 4.2 (lines 11-14).
Figures 4.2 (a-c) show how RDD is applied to the example described in section 4.2. The three computational zones are divided between six processors. Zone 1 is assigned to processors 0 and 3 only, zone 2 to processors 1 and 4 only and zone 3 to processors 2 and 5 only. Processors 0 and 3 do not have any geometry nor flow data of the zones 2 nor 3. A zone interface array is therefore needed to share inter-block boundary cell data among the processors. This zone interface array is made up by the hashed cells in figure 4.2(a) and is present in all processors. As each zone is independent from one

Table 4.2: RDD code implementation

```
!$   Exchange data across block interfaces (k_planes)
1:   left = myproc_block − 1
2:   right = myproc_block + 1
3:   SEND_RECV 2 k_planes from left to right on block_comm
4:   SEND_RECV 2 k_planes from right to left on block_comm

!$   Collect zone interface data from each block on block master
5:   IF myproc_block = 0
6:     FOR mype = 1, nprocs_block − 1
7:       RECV zone_interface_data from mype on block_comm
6:     END
8:   ELSE
9:     SEND zone_interface_data to 0 on block_comm
10:  ENDIF

!$   Broadcast zone interface data across all masters (non-master processors idle)
11:  FOR mype = 0, nprocs_master − 1
12:    BCAST zone_interface_data from mype on master_comm
13:  END

!$   Each block master broadcast received zone interface data across its block
14:  BCAST zone_interface_data from 0 on block_comm

!$   Run the flow solver on each block
15:  U_block= U0_block+RK δU_block
16:  GO TO 1
```

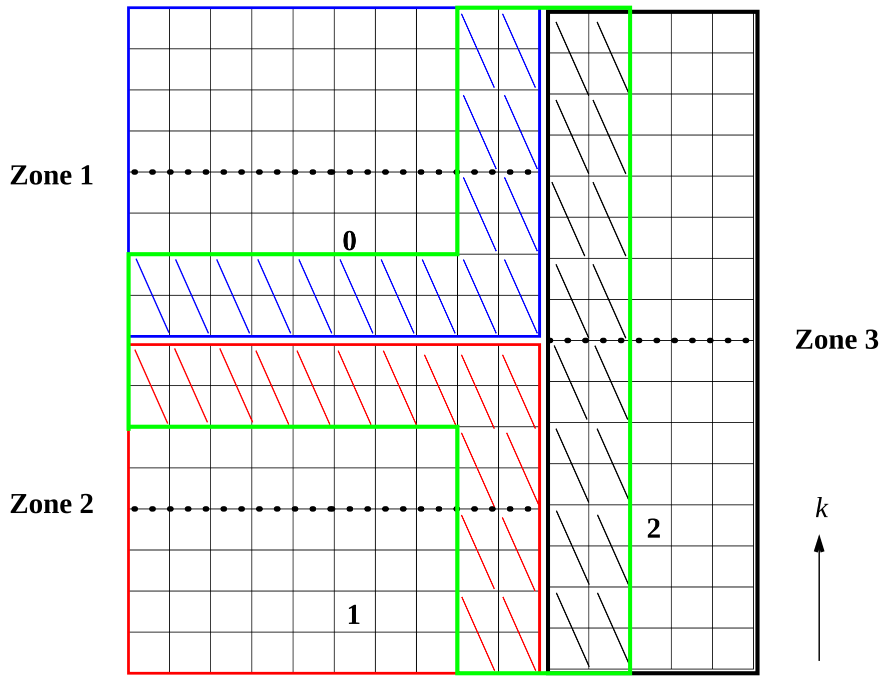

(a) Master boundary interface (green box)

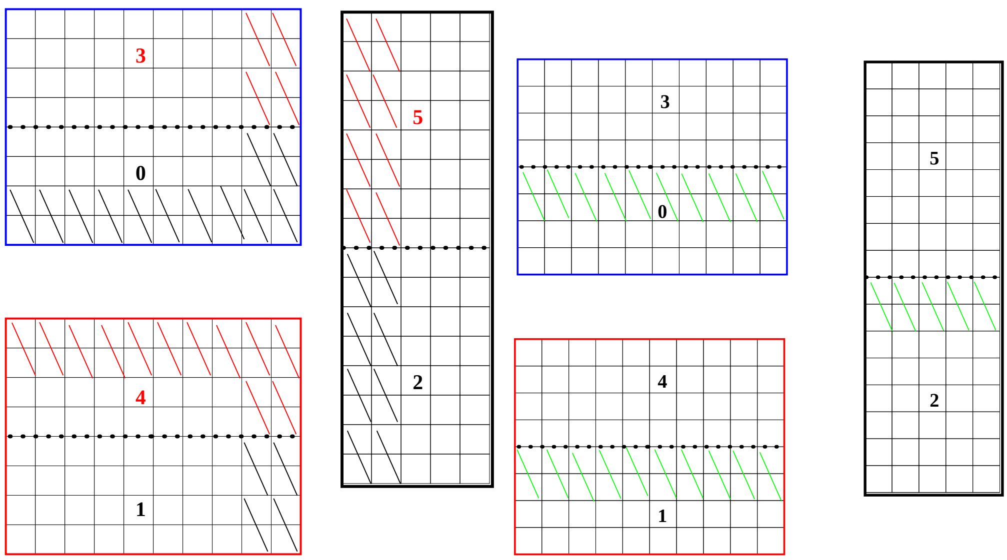

(b) Local exchange of boundary interface cells in red (3 → 0), (4 → 1), (5 → 2).

(c) Local boundary cells exchange in green (0 → 3), (1 → 4), (2 → 5).

Figure 4.2: Recursive domain decomposition.

another, the communication in figure 4.2(c) and within the same zone is happening simultaneously.
The data of the zone is mapped in memory of all the processors of a group therefore it can be sent and received in any of this processors without using a buffer, as it is in SDD implementation. A green hashing is used in figure 4.2(c) is used to identify the cell data sent from processor 0 to 3, from 1 to 4, and from 2 to 5. As . In figure 4.2(b), a red continuous line identifies the cells exchanged in each block that are needed to fill the interface block-let. All the information is gathered in the master processor of each block, namely 0, 1 and 2 in the example. After gathering the information in these processors, it is exchanged among master processors to update the zone interface data. Finally the zone interface data is asynchronously sent to the other processors of each group, 3, 4, and 5 in this example.
The data size of communication in RDD is larger than in SDD. However, a larger number of processors can be used with RDD, leading to a smaller memory requirement per processor compared to SDD.
The RDD parallelization is also more flexible in terms of applicability because it allows to even up the computational load among processors in the domain with uneven block sizes. Identifying the smaller zone in the multi-zone computational domain, it can be used as a base to divide the other zones along k so that roughly all processors compute a similar number of cells. A large part of the communication happens asynchronously and RDD is applicable to large computational domains. In the current implementation, RDD is limited by the extent of the zone interface data, which is a memory map that is allocated in the memory of all processors

4.4 Parallelization performance

For a given CFD problem, it is possible to evaluate the parallelization performance of the code on a given HPC cluster by using two parameters: the code speed-up and the parallelization efficiency. Let T_0 be the time needed to perform one time step that corresponds to two Runge-Kutta sub-iterations using the code on one processor of the HPC cluster, and T_p the time to perform the same time step by the parallelized code on

N_{procs}	T_0 [sec]	T_p [sec]	S_p	η [%]
1	90.19	90.19	1	100
2	90.19	45.53	1.98	99.04
4	90.19	23.69	3.81	95.18
8	90.19	13.55	6.66	83.2
16	90.19	9.23	9.77	61.07

Table 4.3: SSD performance on the CINECA cluster.

more than one processor. The speed-up $\left(S_p\right)$ is defined as

$$S_p = T_0/T_p \tag{4.6}$$

The parallelization efficiency $\left(\eta_p\right)$ of the algorithm is

$$\eta_p = S_p/nprocs \tag{4.7}$$

The ideal situation corresponds to $S_p = nprocs$ for any number of processors. A super-linear speed-up $S_p > nprocs$ can be achieved by parallelization due to cache aligning. The speed-up growth is limited by the communication time and by the load balance.
The performance of SSD, described in section 2.7 4.2, was tested at the HPC cluster at CINECA, Bologna, Italy. The performance of RDD was tested on two different HPC clusters at CINECA and at HECToR, Edinburgh, United Kingdom. The results are documented in tables 4.3 and 4.4.
The values in tables 4.3 and 4.4 are obtained with a computational mesh of 1.4 million cells divided into six zones.
The SDD parallelization performs well up to 8 processors, as shown in the value from table 4.3. The lower parallelization efficiency with 16 processors is due to the overhead related to the data exchanged versus the data computed by each processor. Essentially, there are not enough *k*-planes to distribute to each processor in the cavity model that was used to develop the MPI, which used a 1.4 million cells coarse computational mesh.
Comparing table 4.3 with table 4.4, the value T_0 is much smaller in the second table. The scalar code was extensively optimized before the new parallelization strategy was

	CINECA				HECToR			
N_{procs}	T_0 [sec]	T_p [sec]	S_p	η [%]	T_0 [sec]	T_p [sec]	S_p	η [%]
1	46.45	46.45	1	100	54.38	54.38	1	100
2	46.45	27.46	1.69	84.58	54.38	29.19	1.863	93.15
6	46.45	10.36	4.48	74.73	54.38	10.11	5.379	89.65
12	46.45	6.22	7.47	62.23	54.38	5.45	9.978	83.15
24	46.45	4.78	9.72	40.49	54.38	3.06	17.77	74.05
36	46.45	4.5	10.32	28.67	54.38	2.24	24.28	67.44
54	—	—	—	—	54.38	1.8	30.21	55.95
72	—	—	—	—	54.38	1.6	33.99	47.21

Table 4.4: RDD performance on CINECA and on HECToR clusters.

implemented. The computational time was reduced by 50% by eliminating recursive operation and simplifying memory access. The lower time per iteration on a scalar machine at the CINECA cluster can be explained by the aggressive optimization done by the Intel compiler.

Figures 4.3 (a,b) are obtaining using the values from tables 4.3 and 4.4. These show that using RDD enables to distribute the computation on a larger number of processors than with SDD, as stated in section 4.3. The code speed-up is close to linear for a low number of processor using SDD, as shown in figure 4.3(a). The efficiency of SDD rapidly decreases towards zero as the number of processors increases, as shown in figure 4.3(a). The faster communication system provided by the HECToR cluster gives a better performance with RDD than the BCX CINECA cluster.

Figure 4.3(a) shows that the SDD code on the CINECA cluster scales a little better than the RDD code for up to 16 processors. The parallelization efficiency advantage is about 10%, as shown in figure 4.3(b). This difference is due to the communication overhead of SDD. This is lower than RDD. The scalability of the code is better on HECToR, where the minimum bi-section bandwidth is 4.1 TB/s. This allows to absorb the extra communication overhead of RDD, leading to a more efficient parallel computation on $nprocs > 8$. Specifically, by sub-dividing a relatively small problem into more zones, the ratio of communication versus computation increases to a level where a further reduction in computational time by domain sub-division is not achieved.

The relatively small 1.4 million cells size of the problem limited the scalability test to 72 processors using RDD. RDD is designed for medium and large CFD problems,

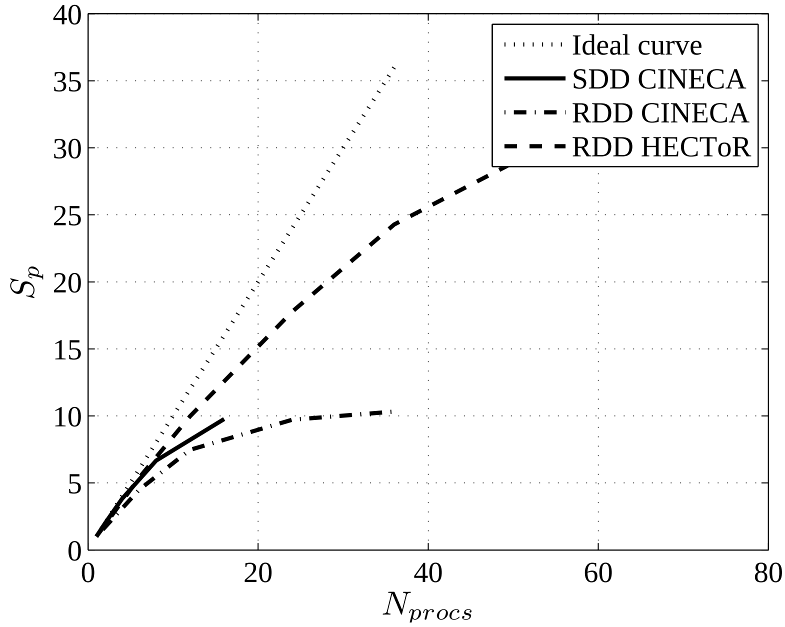

(a) Code speed-up.

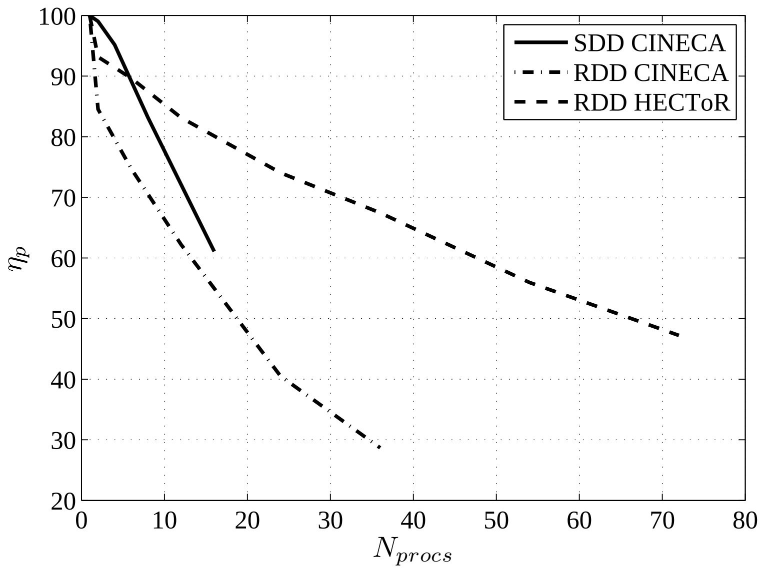

(b) Code parallelization efficiency.

Figure 4.3: Parallelization performance on different HPC clusters.

where each processors works on a block of adequate size of 10^4 to 10^5 cells. SDD cannot be tested on a problem larger than 2×10^6 cells due to high memory demand of the DES flow solver, described in paragraph 3.4. In the mesh-refined CFD test case, analysed in paragraph 6.4, that consists of 9×10^6 cells, a minimum of seven zones were used to satisfy the memory constrain of a single processor. The DES model of a three-dimensional computation requires a fine mesh in region of separated flow to describe the small eddies therein. This can be computed only using the RDD implementation. A low fidelity model, as the one used in this analysis, can give some information on trends and mean flow parameters but is not sufficient to describe the small structure interaction that is typical of turbulent flow simulations. RDD is the only applicable MPI implementation to solve medium and large CFD problems with the University of Leicester in-house code.

4.5 Conclusion

The algorithms used to parallelism the flow solver were herein described. The performances of the two algorithms shows that the RDD performs better when the number of processors used in the computation increases. The latter also advantage from a decrease in the memory consumption associated with it. Only a portion of the computational domain is needed in each processor in this later case.

Chapter 5

Computational domain

5.1 Introduction

At present a ‘black box’ grid generator able to produce acceptable mesh does not exist (Löhner, 2001). Commercial grid generators such as GAMBIT, that employ semi-automatic grid generation, are often used in industrial CFD. The author does not use such a generator, due to the relatively simple geometry of this study. The major advantage to generate the computational grid with in-house software is the ability to control the stretching ratio and the mesh skewness. In this chapter, the mesh used in the computation is described in terms of number of cells and computational domain size. The mesh skewness is also analysed. The flow parameters at the boundary conditions are given and the non-reflectivity of the boundaries is also studied.

5.2 Euler and DNS

The computational domains used in Euler and DNS simulations are identical. The aim of the simulations is to identify the instability mode that drives the cylindrical cavity flow. Different boundary condition are used in the two simulations. The resulting flow field is influenced by the introduction of a finite boundary layer thickness in the DNS as discussed in section 6.3.

The computational domain outside the cavity is $18.4L \times 18.4L \times 9.6L$, as shown in figure 5.1. A large domain of the order of 20 L is used to resolve at least one full acoustic

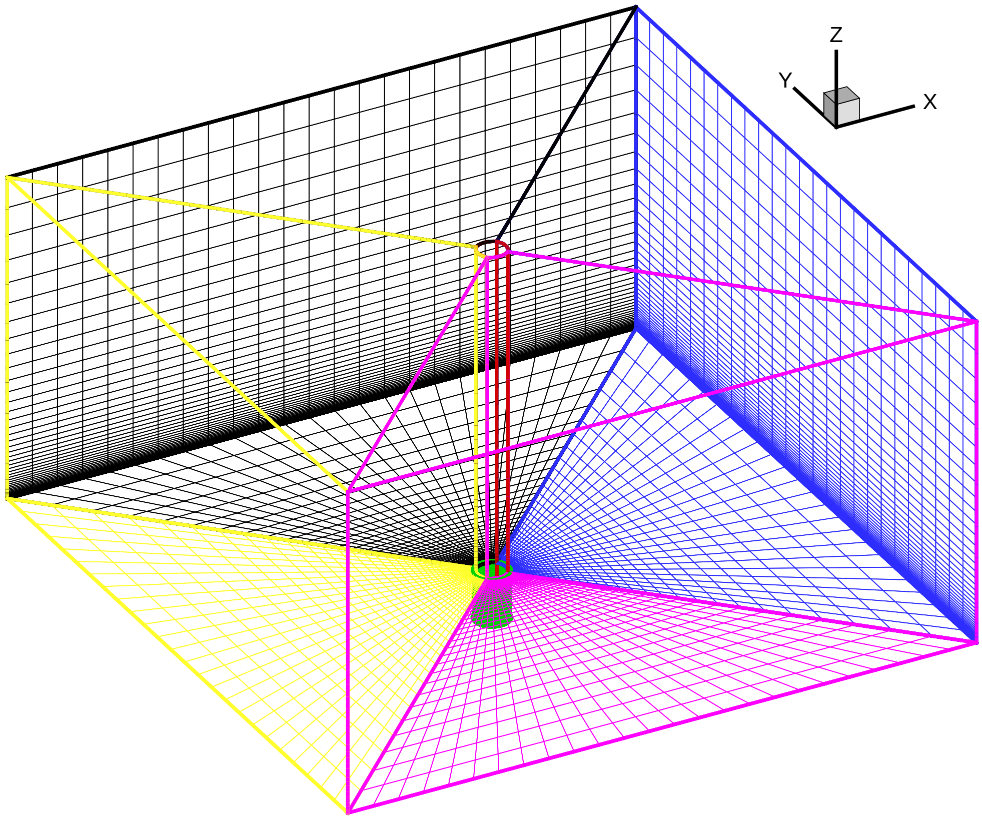

Figure 5.1: Computational mesh.

wavelength of the radiating sound. A preliminary Euler simulation suggested a low frequency mode instability in the deep cylindrical cavity flow (Grottadaurea & Rona, 2007a). The computational domain is the smallest that allows to separate the radiating pressure field from the hydrodynamic pressure due to the near-potential flow at the cavity open end as suggested by Colonius & Lele (2004). Specifically, the domain boundaries are located far enough so that the radiating pressure is dominant across them.

The computational domain boundaries are chosen so that the spurious waves in the far-field do not affect the self-sustained instability mechanism in the cavity flow.

The domain is discretized using a topologically orthogonal three-dimensional (i, j, k) curvilinear mesh. Curvilinear coordinates are used to map i and j into the streamwise direction x and spanwise direction y, where the cells of the central zone are barrelled.

The cells are elongated along the 45° angle to meet rectilinear axes at the computational domain boundary.
A simple O-type mesh cannot be used to solve the cylindrical cavity flow with a Cartesian flow solver without modifications. Shur *et al.* (2003) used a barrelled zone surrounded by an O-type mesh for a three-dimensional DNS of jet noise. This technique removes the geometrical singularity of a conventional cylindrical mesh at the origin. A similar approach is used in this study of the cylindrical cavity.
A constant stretching ratio (r_i) is used in the conformal mapping in the radial direction and in the flow normal direction. A constant spacing is used in the azimuthal direction along the cavity walls. In the computational domain, $r_i \leq 1.05$. The round off error introduced by a 5% stretching is often acceptable (Löhner, 2001).
100 equi-spaced cells are used around the cavity walls. A wall-normal distance $\Delta z = 2.94 \times 10^{-3} L$ is used at the first cell and 12 cells are used within the boundary layer thickness in the coarse DNS test case, 24 in the refined test case. 44 Cells are used in the z direction outside the cavity, 37 cells within the cavity in the $L/D = 0.71$ deep cavity and 19 cells in the $L/D = 2.5$ shallow cavity. A mesh refined test case was used in the shallow cavity test case, with 24 cells within the cavity and 48 cells outside. Along the radius from the cavity axis, 40 cells are used in both cases. The cells in the centred barrelled zone are 25×25. In the flow normal direction, the total number of cells is varied to investigate the numerical convergence of the results, as discussed in section 6.3. 13 and 14 cells are used to discretize the inflow boundary layer in the wall-normal direction at $Re_\theta = 10750$ and $Re_\theta = 8850$ respectively. 1.4 million cells are used in the $L/D = 0.71$ cavity model and 1.26 million cells in the $L/D = 2.5$ model in the first under resolved test case. The 1.4 million cells test case was refined further to achieve mesh convergence to 2.6 million cells and to 9.2 million cells.
The refined test case in section 5.3 uses a cell size of $z^+ \approx 30$ at $y = -2L$ upstream of the cavity leading edge. The introduction of the wall function given in section 3.4.3 was necessary to achieve an estimate of the friction velocity and boundary layer growth rate at the cavity leading edge.
In LES simulations, the cell should be ideally of cubic shape to give $\Delta x \approx \Delta y \approx \Delta z$. The smallest scales of turbulence are modelled by the Smagorinsky constant and the dissipation at these scales is assumed to be isotropic. The cells in the cavity neighbourhood aim to achieve this condition.

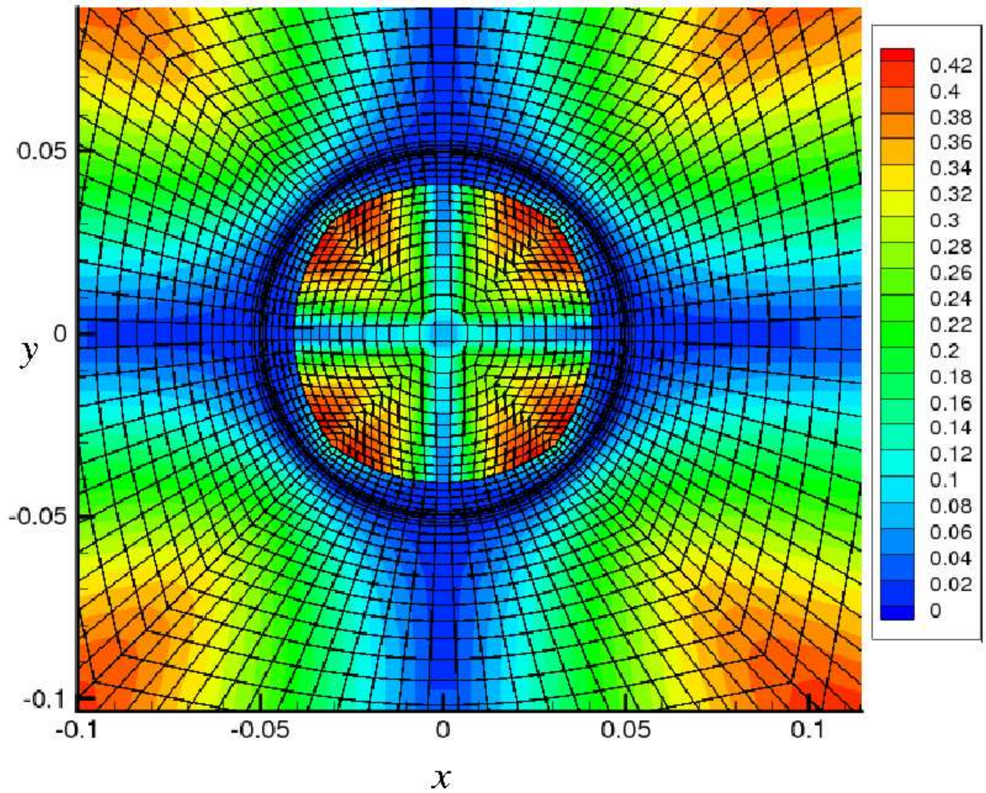

Figure 5.2: k-plane skewness over the cavity open end

A limiting factor in the three-dimensional CFD computations is the cell deformation produced by the stretching away from the cavity. Highly stretched cells introduce dispersion and dissipation errors. Stretching is necessary to resolve the acoustic near-field using a limited number of cells but this leads to unwanted cell skewness. The cavity acoustic far-field is where the radiated pressure fluctuations amplitude decays geometrically as $I \propto r^{-2}$, where r is a the radial distance from the noise sources origin and I the sound wave intensity. The main noise source is often located at the downstream cavity corner.

The mesh at $z \geq 0$ is generated by reproducing the mesh at $z = 0$. All $z \geq 0$ planes have the same (x, y) coordinates. The cell skewness (γ_1) in any $z \geq 0$ plane, shown in figure 5.2, is investigated.

It is defined as

$$\gamma_1 = \frac{\max(||\mathbf{d}_1||, ||\mathbf{d}_2||)}{\min(||\mathbf{d}_1||, ||\mathbf{d}_2||)} - 1 \tag{5.1}$$

where $\mathbf{d}_1$ and $\mathbf{d}_2$ are the diagonals of the lower face of computational cell i, j, k and are: $\mathbf{d}_1 = \mathbf{x}_{i+1,j+1} - \mathbf{x}_{i,j}$ and $\mathbf{d}_2 = \mathbf{x}_{i,j+1} - \mathbf{x}_{i+1,j}$, where $\mathbf{x}_{i,j}$, $\mathbf{x}_{i+1,j}$, $\mathbf{x}_{i,j+1}$, $\mathbf{x}_{i+1,j+1}$ are the position vectors of the face vertices.
The four corners of the central zone, in red in figure 5.1, is where the skewness has the maximum value of 0.42. The numerical instability and the numerical dissipation and dispersion errors associated to the skewness and the stretching was investigated by You *et al.* (2006). It was found that the skewness increases the numerical instability and that it is enhanced in highly stretched meshes. The analysis also suggested that, when possible the mesh has to be aligned with the flow direction to reduce the numerical error associated with the angle between the mesh lines and the flow direction. The maximum value of the skewness found in this mesh is considered acceptable for the order of accuracy of the scheme used in the simulations. As the skewness is an index of the local mesh deformation, it is best minimized throughout the domain. An advantage of the generated computational mesh is the modest deformation of the cells around the perimeter of the cylinder. The skewness at these positions is close to 0, which helps to resolve the growing shear-layer around the cylindrical wall.

5.3 DES

By domain decomposition, the computational domain of figure 5.1 is divided into six zones. The six zones have a similar number of cells to even out the computational load among the processors in the MPI implementation of the code.
Previous numerical investigations of this cylindrical cavity configuration by Grottadaurea & Rona (2007a,b) showed that a computational domain of size 13 L x 13 L x 9 L outside the cavity is required to resolve at least one full acoustic wavelength of the radiating sound. Therefore a domain of 13 L x 13 L x 9 L was used.
Given the physical constraint in section 2.2, the wall friction velocity is estimated to give $z^+ = 1$. A thin boundary layer approaches the cavity and it was found that $\Delta z \approx 4.1$ μm corresponds to the value at $z^+ = 1$. Bennett (2005) and El-Dosoky (2009) used a $CFL \leq 0.4$, this value was found to give a numerically stable computation for the explicit in-house CFD code. To meet this condition, a time step $\Delta t = 3.7$ ns would be necessary. This cannot be used in the simulation, due to the intense computation that corresponds to such a small time step. A 64 million cells computational mesh would be

necessary to achieve a well-resolved LES three dimensional model of the cylindrical cavity test-case. The introduction of a wall model is therefore necessary to reduce the computational cells by allowing larger volume cells to be used close to the walls.
The 1.4 million cells, used in the $L/D = 0.71$ cavity model, and the 1.26 million cells, used in the $L/D = 2.5$ model, consisted in 128 cells around the cavity circumference. The mesh skewness over the cavity opening was investigated and minimized in Grottadaurea & Rona (2007b). The first cell center in the boundary layer corresponds to $z^+ = 30$ and a wall function is used to impose the no-slip condition as described in section 3.4.3.
The mesh convergence of the $L/D = 0.71$ predictions was investigated by running a 2.6 million cells mesh refined test case. 256 equi-spaced points are used around the cavity circumference in this test case.
The code was run over 72 processors at the supercomputer facilities HECToR and BCX. HECToR is a 11,328 AMD 2.8 GHz Opteron processors cluster, delivering 59 Tflops at peak, located in Edinburgh, UK. BCX is a 1280 Opteron IBM Quad Core 2.6 GHz processors cluster, located in CINECA, Bologna, IT. It delivers 27 Tflops at peak. The mesh refined test of 2.6 million cells case was able to resolve a higher instability mode compared to the coarser 1.4 million cells case. This instability is discussed in the experimental comparison in section 6.7. A third level mesh refinement of 9.2 million cells was needed to validate this numerical result. This consists of 2.41 million cells inside the cavity and 6.82 million cells outside the cavity. 384 equi-spaced points are used around the cavity walls. The barrelled zone is 96×96 cells. 30 cells are used within the boundary layer thickness in the wall normal direction. 120 cells are used in the normal direction and 122 cells are used along the $45°$ in the block boundaries outside the cavity. The computational domain is divided into seven zones in this final test-case, to allow the variable space that correspond to each zone to fit in the memory of its designated processor in the computer cluster. This medium size computation cannot be run in less than seven computers, due to memory restriction. The MPI implementation is essential in this simulation.
The mesh skewness reduces by 10% with each successive mesh refinement step. The numerical results are expected to benefit from this progressive reduction in skewness.

5.4 Free-stream values in the boundary condition

5.4.1 Euler and DNS

In the far-field, two flow states $(\mathbf{u}_\infty, p_\infty, T_\infty)$ are used for $M_\infty = 0.235$ and $M_\infty = 0.3$. These are $(102.1, 0, 0)^T\ m/s$, 101325 Pa, 298.15 K and $(80, 0, 0)^T\ m/s$, 101325 Pa and 298.15 K. At the inflow, $\mathbf{u} = \mathbf{u}_\infty$ and $\rho = \rho_\infty = 1.225\ kg/m^3$. At the outflow, the reference pressure is $p = p_\infty$.
The free-stream parameters were chosen in consultation with Airbus France and are representative of those found in a civil aircraft at landing. The International Standard Atmospheric (ISA) condition applies to this flow.

5.4.2 DES

Only the $L/D = 0.71$ deep cavity configuration at $M_\infty = 0.235$ was studied using the DES scheme. The computational expense limits the total number of possible runs to only one test for the mesh refined case.
The flow conditions are those of the Euler and DNS tests, selected in consultation with Airbus France. Parallel wind-tunnel measurements were conducted at the DIMI wind tunnel for an almost dynamically similar model (Pengyuan & Biondini, 2007; Verdugo *et al.*, 2009). The limitation in the wind tunnel maximum speed were such that only L/D, L/θ and Re_L are matched. The experiment were done at $M_\infty = 0.118$ and compressibility effects are neglected in the flow comparison.
The free-stream flow state is

$$\begin{pmatrix} \mathbf{u}_\infty \\ p_\infty \\ T_\infty \\ k_\infty \\ \omega_\infty \end{pmatrix} = \begin{pmatrix} (80, 0, 0)^T \mathrm{m/s} \\ 101325\mathrm{Pa} \\ 298.15\mathrm{K} \\ 0.24\mathrm{m}^2/\mathrm{s}^2 \\ 7255\mathrm{s}^{-1} \end{pmatrix} \tag{5.2}$$

The inflow turbulent boundary layer profile and the free stream values of k and ω are detailed in the appendix B. The turbulent boundary layer mean velocity profile is obtained by the formula of Rona *et al.* (2009). This formula used explicitly the value of the friction velocity, the free-stream velocity and the boundary layer thickness as input to determine the mean velocity profile that is used at the inflow condition. At the outflow, only the back pressure $p = p_\infty$ is imposed under the assumption of a streamwise zero pressure gradient flow.

5.5 Boundary condition sensitivity analysis

The non-reflective boundary conditions described in sections 3.2.3 and 3.4.3 are analysed. The sensitivity of the numerical solution with respect to these boundary conditions is studied through the near-field sound pressure level (SPL). This is evaluated using the root mean square pressure fluctuation obtained by averaging 25 frames that are evenly distributed in time around one characteristic period of the cavity instability. Figure 5.3 is obtained using the inviscid flow simulation at $M_\infty = 0.3$ in the deep cavity test case. This is characterized by a high amplitude pressure fluctuation as discussed in section 6.2.3 and reported in Grottadaurea & Rona (2007a). Figure 5.3 shows a monotonic reduction of the SPL from the enclosure towards the computational domain through-flow boundaries. It indicates that the boundary conditions allow the passage of the outgoing pressure waves with no appreciable reflection. Minor spurious waves are found at the domain upper edges, as indicated by the change in the contours shape from convex to concave close to these edges.
The linear assumption used to obtain the non-reflective the boundary condition cannot be simultaneously satisfied in the two direction at the edge of the computational domain. This causes a localized pressure wave reflection towards the computational domain interior due to the pressure gradient set to zero in one direction. These waves are of small amplitude compared to the main instability mode and do not greatly affect the numerical solution. Moreover, the mesh is very coarse at the outer domain boundary. This introduces a locally high numerical dissipation and further reduces the propagation of these reflected waves in the computational domain. Close to the outer domain boundaries, the numerical dissipation induced by the mesh coarsening gives a behaviour similar to the introduction of a sponge zone.

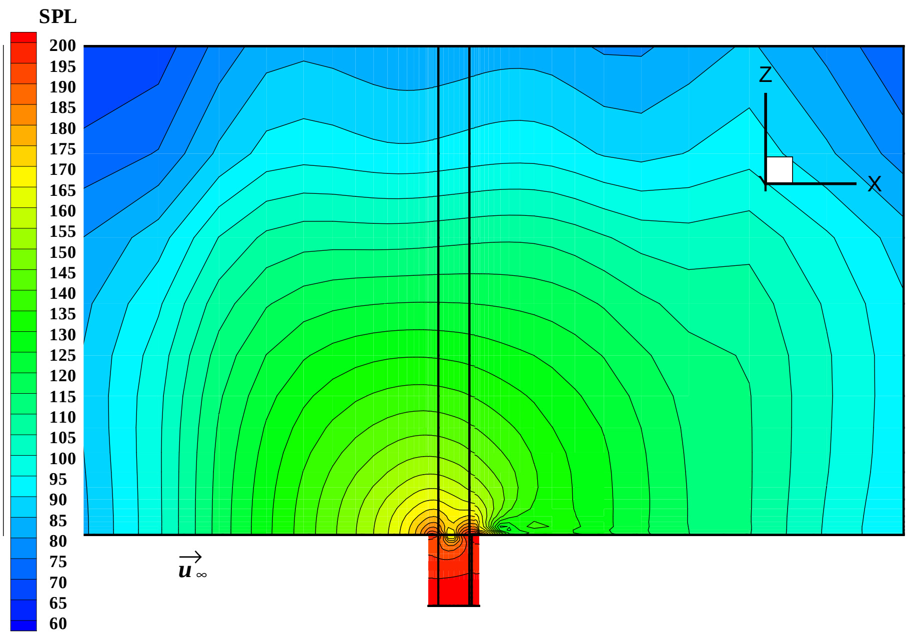

Figure 5.3: Near-field SPL on the y = 0 plane. SPL$_{min}$ = 60 dB re 20 nPa, SPL$_{max}$ = 200 dB re20 μPa, ΔSPL = 5 dB.

5.6 Summary

The meshes used in the numerical model were described in terms of the number of cells and computational domain sizes. The mesh skewness was also analysed and it was found to benefit to a 10% reduction when a finer mesh is used. The non-reflectivity of the boundary conditions was studied by evaluating the SPL along the computational boundaries. No spurious reflection of significant amplitude was found in the computation.

Chapter 6

Aeroacoustic predictions

6.1 Introduction

This chapter presents time-dependent numerical simulations of the unsteady pressure near-field of a cylindrical cavity of length and depth ratio $L/D = 0.71$ and $L/D = 2.5$, tested at free-stream Mach numbers 0.235 and 0.3. Simulations are presented from solving the Euler equations, which gives an inviscid model, and the discretized Navier-Stokes equations without turbulence modelling, which gives a viscous model that uses a laminar inflow boundary layer of $Re_\theta = 8424$ at $M_\infty = 0.235$ and of $Re_\theta = 11260$ at $M_\infty = 0.3$ for both L/D test cases. All models use the same computational domain that extends 8 L upstream and downstream of the cavity, 8 L either side of the cavity, and 9 L above it. The CFL number is smaller than 0.3 in all the models and it represents a very large constraint in the mesh-refined test cases in the viscous flow simulations.

6.2 Inviscid model

At the start of the computation, the flow within the enclosure is at rest while the flow above it is uniform at the free-stream velocity. The inviscid model uses the mesh described in section 5.2. The inflow conditions $(\rho_\infty, \mathbf{u}_\infty, p_\infty)$ are uniform and are $\rho_\infty = 1.225$ kg/m^3, $p_\infty = 101325$ Pa, and $\mathbf{u}_\infty = (102.1, 0, 0)^\mathrm{T}$ m/s at $M_\infty = 0.3$ and $\mathbf{u}_\infty = (80, 0, 0)^\mathrm{T}$ m/s at $M_\infty = 0.235$. A vortex sheet spans across the enclosure opening, separating the stagnant flow from the free-stream. In practice, the numerical dispersion

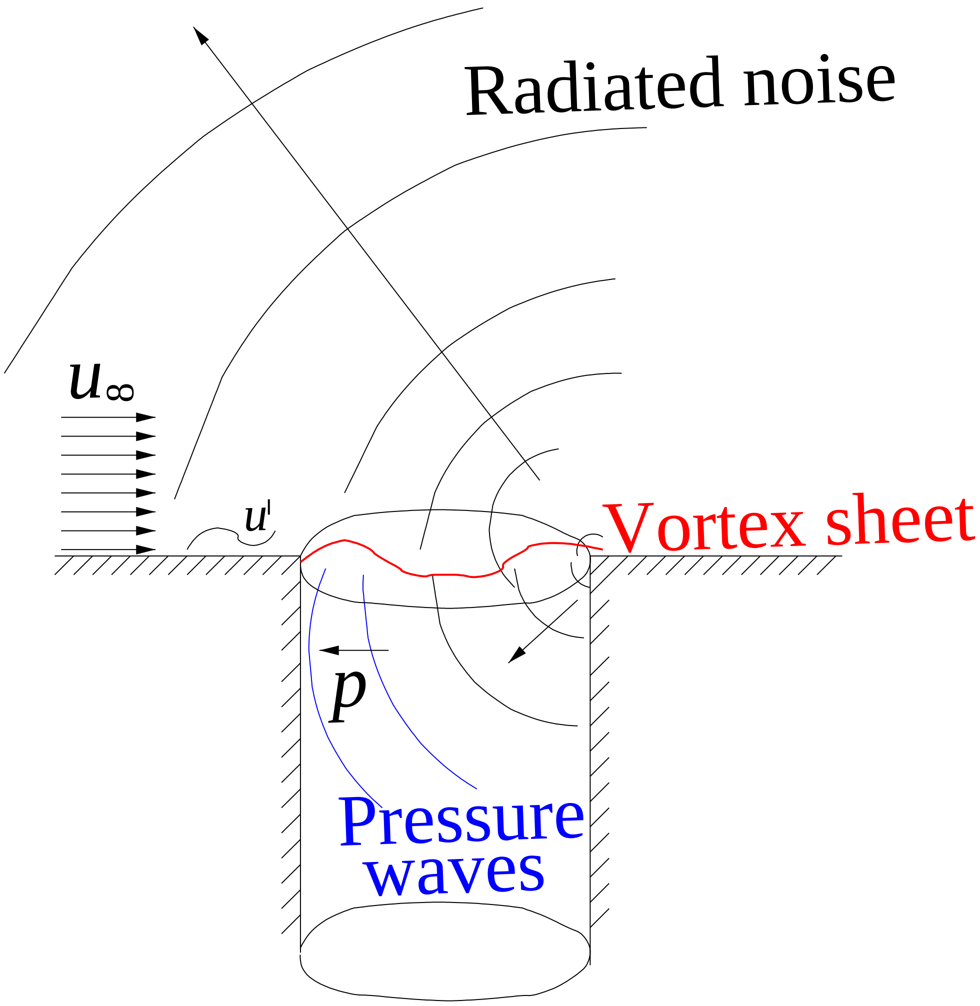

Figure 6.1: Sketch of the cavity flow in the inviscid model.

and dissipation in the flow solver generates numerical viscosity that thickens the vortex sheet as it stretches above the enclosure. This is sketched in figure 6.1. The resulting inflected velocity profile is similar to that of a shear-layer and grows Kelvin-Helmholtz type convective instabilities (Bradshaw *et al.*, 1960). The interaction of this finite-thickness vortex sheet with the downstream cavity corner is the subject of the study in these simulations, as reported in Grottadaurea & Rona (2007a).

6.2.1 Time-averaged flow

Figures 6.2(a) and 6.3(a) show the mean streamwise velocity component at the cavity opening in the $L/D = 0.71$ and $L/D = 2.5$ cavities at $u_\infty = 80$ m/s and at $u_\infty = 100$ m/s respectively. Figures 6.2(b)-(d) and 6.3(b)-(d) show the streamlines in the two configurations in the planes $y/L = 0$, $y/L = -0.25$ and $y/L = 0.25$. The averages are obtained as the algebraic mean of 54 frames and 35 frames respectively over one characteristic period of cavity oscillation.

The mean streamwise velocity component decreases asymmetrically over the cavity open end of the deep cavity configuration and its minimum is at $y/L = 0.2$. Given the strong asymmetric patten in the enclosure (Grottadaurea & Rona, 2007a), a corresponding strong asymmetry would be expected in the cavity wake region downstream the cavity trailing edge. This strong asymmetric behaviour is shown in figure 6.2(a) only close to the cavity edge at $y > 0$. Further downstream, the flow regains the symmetry of the free-stream inflow condition. The loss of momentum given by the cavity reduces the streamwise velocity in the wake region.

The asymmetry in the streamwise velocity component suggests that the flow enters the cavity only on one side in the region $0 < y/L < 0.5$ and is ejected from the other side $-0.5 < y/L < 0$. This is confirmed by figures 6.2(c) and 6.2(d), in which the streamlines are pointing towards the cavity bottom in the plane $y/L = -0.25$ in the region $-0.1 < z/L < 0.1$ whereas are pointing upwards in the plane $y/L = 0.25$ in the same region. The flow separates at the cavity leading edge, forming a vortex sheet that spans across the region $-0.1 < z/L < 0.1$. A similar asymmetric recirculation in a $L/D = 2$ cylindrical cavity was observed experimentally by Hering *et al.* (2006) and by Dybenko *et al.* (2006).

The vortex core is located at $x/L = 0.1$ and $z/L = -0.4$ in the plane $y = 0$, whereas it is located at $x = 0$ and $z/L = -0.7$ in the plane $y/L = -0.25$. The different locations of the vortex core indicate that the vortex tube is bent inward and upward in the flow past the cavity. This effect is mainly due to the effect of the numerical viscosity. The 'viscous' layer is characterized by a different thickness over the cavity opening and therefore the convective velocity is different at different y = constant planes.

The flow in the $L/D = 2.5$ cavity is mainly symmetric with respect to the cavity center, about the spanwise plane $y = 0$, as shown in 6.3(a). The flow enters the cavity in the

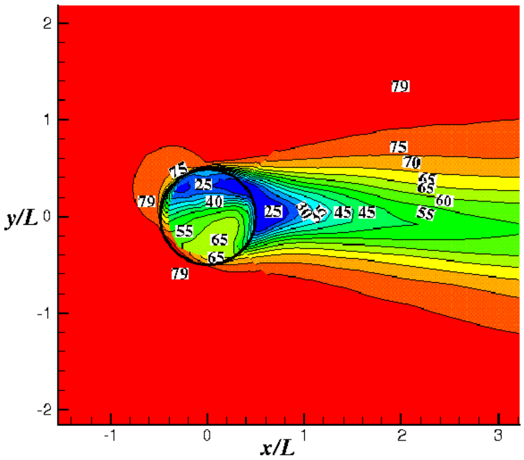

(a) Mean streamwise velocity component in the $z/L = 1.4$ plane. Velocity is given in m/s.

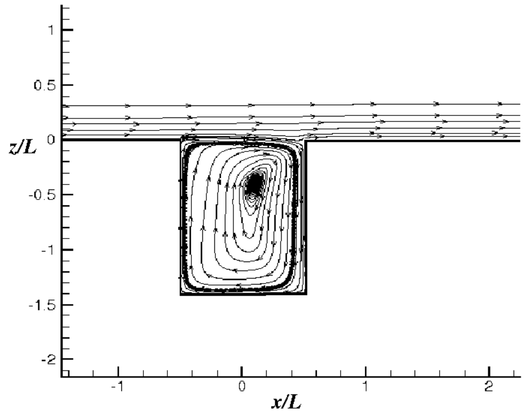

(b) Streamlines in the enclosure in the $y/L = 0$ plane.

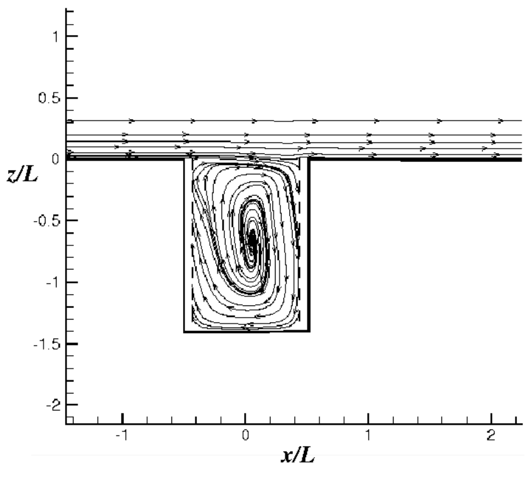

(c) Streamlines in the enclosure in the $y/L = -0.25$ plane.

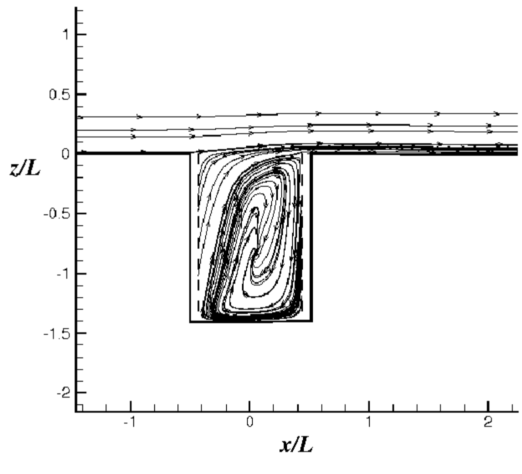

(d) Streamlines in the enclosure in the $y/L = 0.25$ plane.

Figure 6.2: Asymmetric recirculation from a $L/D = 0.71$ deep cavity at $M_\infty = 0.235$.

spanwise central area at about $-0.2 < y/L < 0.2$ and is ejected from the cavity sides $-0.5 < y/L < -0.25$ and $0.25 < y/L < 0.5$. A higher velocity magnitude is found in these areas compared to the $L/D = 0.71$ predictions, as shown by figures 6.3(b) to 6.3(d). The streamlines are pointing downwards only in the plane $y = 0$, reducing the streamwise momentum transport into the cavity and leaving a higher momentum overflow across its open end. In the wake region, the flow is symmetric and accelerates towards the centreline to balance the conservation of mass. Further above the enclosure, the flow is at constant free-stream velocity. A bound vortex is found inside this cavity with the core angled at about 45° with respect to the streamwise direction. The bound vortex core is located at $(x/L, y/L, z/L)$ $(0.25, 0, -0.1)$ and $(0, \pm 0.25, -0.27)$. The numerical predictions indicate that the recirculation pattern inside the enclosure is similar at $M_\infty = 0.235$ and $M_\infty = 0.3$ and is more dependent upon the cavity geometry.

6.2.2 Aerodynamic instability

Figures 6.4(a) and 6.4(b) show instantaneous streamlines and pressure iso-surfaces in the enclosure in the $L/D = 2.5$ shallow cavity. The symmetric recirculation is confirmed also by these instantaneous images at both $M_\infty = 0.235$ and $M_\infty = 0.3$. The interaction between the fluctuating vortex sheet predicted by the Euler model and the cavity trailing edge produces pressure waves as predicted by the aerodynamic noise generation theory of Powell (1964). The frequency that characterizes these pressure waves phase-locks the vortex sheet fluctuation, producing a self-sustained instability. The numerical predictions suggest that the recirculation pattern inside the enclosure is independent from the free-stream velocity but it is related to the cavity geometry. The $L/D = 2.5$ cavity flow is found to have a dominant instability mode at $St = 0.833$ at $M_\infty = 0.235$ and at $St = 1.448$ at $M_\infty = 0.3$. The maximum velocity in the upstream direction inside the enclosure is approximately $u = -24$ m/s at $M_\infty = 0.235$ and $u = -40$ m/s at $M_\infty = 0.3$. The near-field pressure fluctuation peak directivity is shown by Grottadaurea & Rona (2007a) to be 135° from the free-stream direction in the two cases. Figure 6.5 shows an instantaneous flow visualization of the $L/D = 0.71$ deep cavity at $M_\infty = 0.235$. Streamlines and pressure iso-surfaces are used to detail the flow in this configuration. As highlighted in sub-section 6.2.1, the flow shows an asymmetric pattern. The flow enters the cavity at $-0.5 < y/L < 0$ and it is ejected from

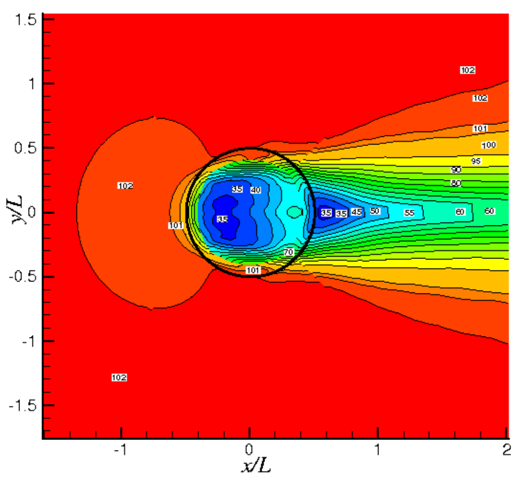

(a) Mean streamwise velocity component in the $z/L = 0.4$ plane. Velocity is given in m/s.

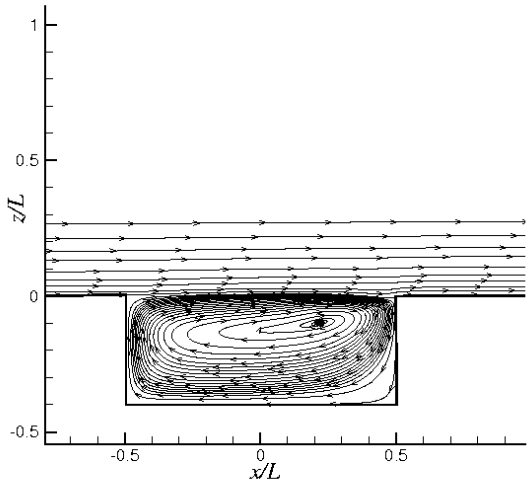

(b) Streamlines in the enclosure in the $y/L = 0$ plane.

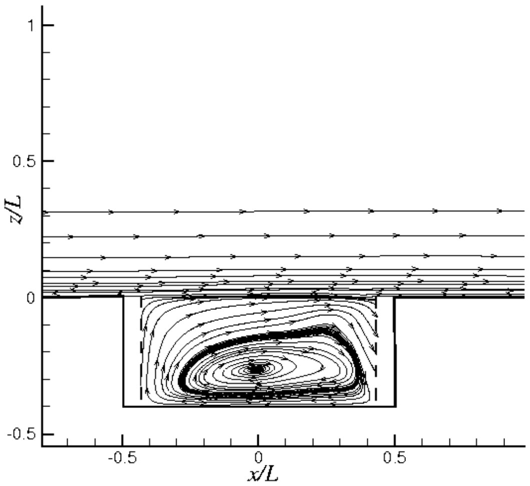

(c) Streamlines in the enclosure in the $y/L = -0.25$ plane.

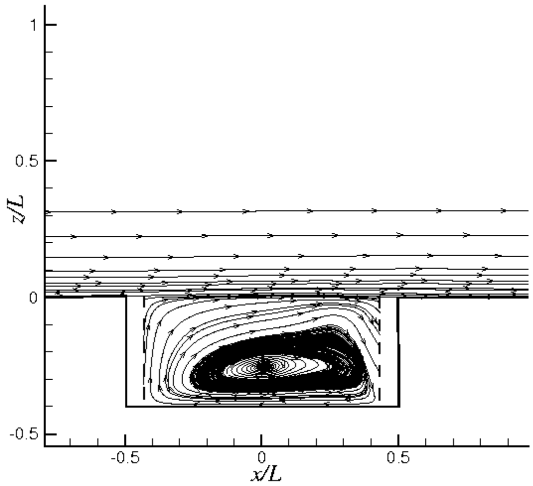

(d) Streamlines in the enclosure in the $y/L = 0.25$ plane.

Figure 6.3: Symmetric recirculation from a $L/D = 2.5$ shallow cavity at $M_\infty = 0.3$.

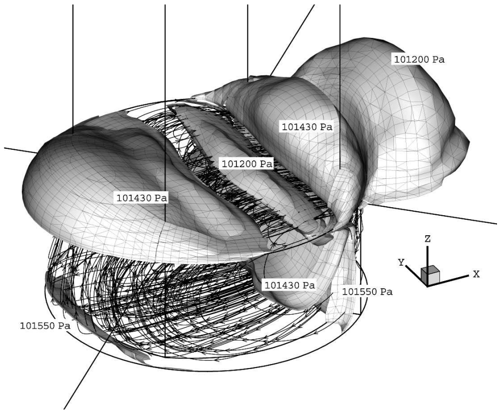

(a) Streamlines and pressure iso-surfaces in the enclosure, $L/D = 2.5$ and $M_\infty = 0.235$.

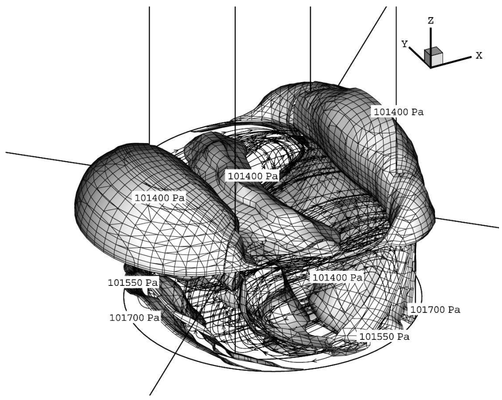

(b) Streamlines and pressure iso-surfaces in the enclosure, $L/D = 2.5$ and $M_\infty = 0.3$.

Figure 6.4: Symmetric recirculation from a $L/D = 2.5$ shallow cavity.

the opposite side at $0 < y/L < 0.5$. The vortex sheet of finite thickness interacts with the cavity downstream edge producing pressure waves. These are shown in figure 6.5 by means of pressure iso-surfaces of different level. The alternating mass injection and ejection either side locates the noise sources asymmetrically on either side of the $y = 0$ mid-span plane. The $L/D = 0.71$ cavity flow is found to have a dominant instability mode at $St = 0.5295$ at $M_\infty = 0.235$ and at $St = 0.491$ at $M_\infty = 0.3$. The maximum convective velocity above the bottom wall of the enclosure is approximately $u = -50$ m/s at $M_\infty = 0.235$ and $u = -63$ m/s at $M_\infty = 0.3$.
Rona (2007) proposed an analytical model of the different acoustic resonant modes in a cylindrical cavity of infinite depth. He found both symmetric and asymmetric cavity modes. The present simulations show that the geometry triggers the selection of different instability modes as the diameter to depth ratio changes.

6.2.3 Radiating pressure near-field

The near-field Sound Pressure Level (SPL) from a shallow cavity configuration is characterized by a low-amplitude pressure fluctuation as shown in figure 6.6. SPL = 87 dB re 20μPa is predicted at $\mathbf{x} = (0, 0, 8L)$ at $M_\infty = 0.3$ and SPL = 86 dB re 20μPa is predicted at $\mathbf{x} = (0, 0, 8L)$ at $M_\infty = 0.235$. Comparing figure 6.6(a) and figure 6.6(b), the near-field SPL iso-contours have a different shape. The SPL has been evaluated using 43 frames at $M_\infty = 0.235$ and 31 frames $M_\infty = 0.3$ over one period of oscillation

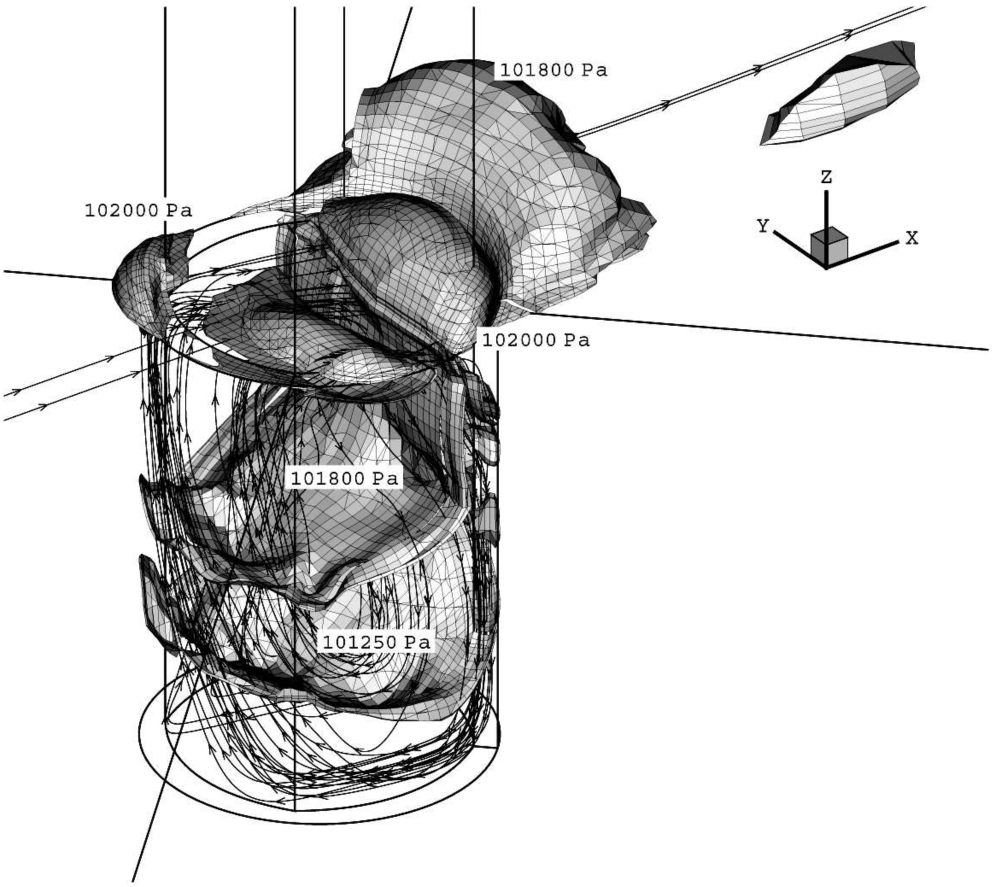

Figure 6.5: Asymmetric recirculation from a deep cavity configuration. Streamlines and pressure iso-surfaces in the enclosure. $L/D = 0.71$ and $M_\infty = 0.235$. Instantaneous inviscid numerical prediction.

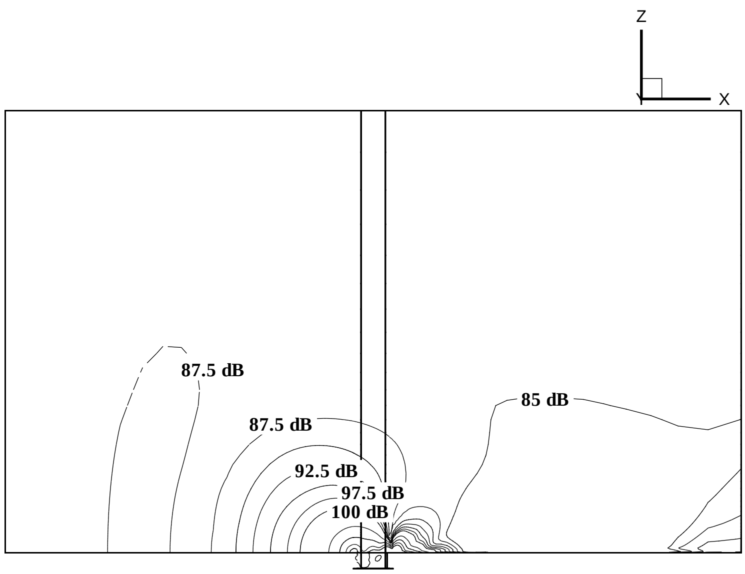

(a) Near-field SPL iso-contours on the $y = 0$ plane. $M_\infty = 0.235$.

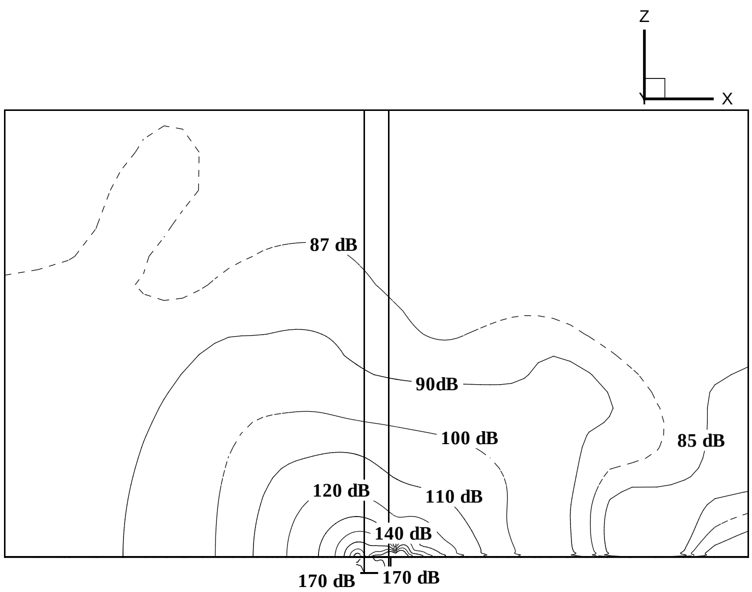

(b) Near-field SPL iso-contours on the $y = 0$ plane. $M_\infty = 0.3$.

Figure 6.6: Predicted near-field SPL from a $L/D = 2.5$ shallow cavity configuration.

in the acoustic near-field. Comparing figure 6.7(a) and figure 6.7(b), the SPL iso-contours in acoustic near-field are similar. The amplitude of the pressure fluctuation decreases monotonically towards the domain boundaries, without appreciable reflection, showing the good performance of the non-reflective boundary conditions used in the simulation. The SPL maxima are higher compared to those from the shallow cavity, suggesting that the azimuthal instability enhances the amplitude of the pressure fluctuations.

The numerical model predicts that the mass ejections alternate either side of the cavity trailing edge with respect to the streamwise direction, as shown in figure 6.5. This results in that, during each mass ejection event, mass is ejected from only one side of the cavity. The higher pressure peak, characterizing this instability, could be related to the more localized interaction between the vortex sheet and the the cavity trailing edge lip.

6.3 Low Reynolds number model

The cylindrical cavity flow that models an aircraft fuel vent at full-scale is characterized by a thin fully developed turbulent boundary layer approaching the enclosure. A preliminary analysis of the effects of the inflow boundary layer momentum thickness and boundary layer growth rate on the unsteady flow is performed by Direct Numerical Simulation (DNS) of a model cavity with a laminar inflow boundary layer of the same momentum thickness as the full-scale model. The results are given in non-dimensional form as in Grottadaurea & Rona (2007b).

Four simulations model two cavities of aspect ratio $L/D = 0.71$ and $L/D = 2.5$ at two free-stream Mach numbers $M_\infty = 0.235$ and $M_\infty = 0.3$. The approaching boundary layer has $L/\theta = 65$ at $M_\infty = 0.3$ and $L/\theta = 62$ at $M_\infty = 0.235$. The computational domain of section 6.2 is used that extends $8L$, $8L$, $9L$ in the streamwise, spanwise and flow-normal directions above the cavity. The mesh is detailed in chapter 5.2. At the solid walls, the no-slip boundary condition described in section 3.3.3 is used. The inflow boundary condition is given in appendix A. A non-reflective boundary condition is applied to the remaining boundaries, where the exterior domain reference flow state is changed to match the free-stream Mach number. The flow is let to develop from

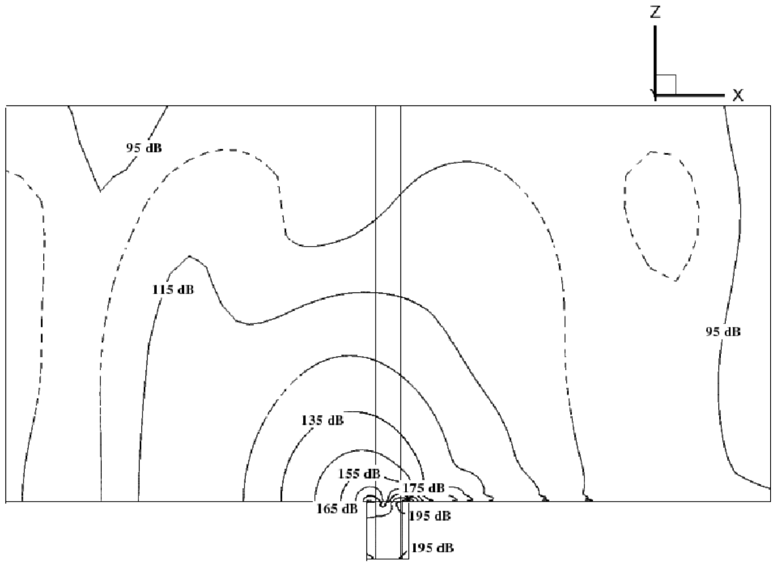

(a) Near-field SPL iso-contours on the $y = 0$ plane. $M_\infty = 0.235$.

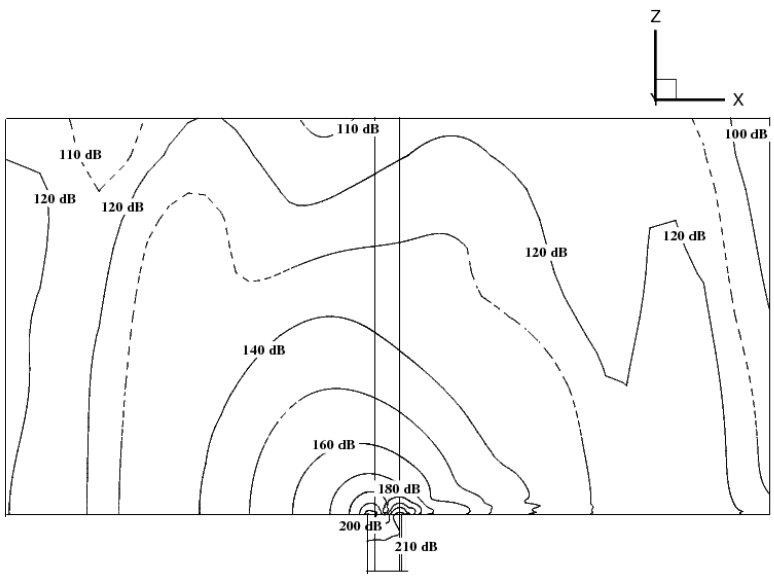

(b) Near-field SPL iso-contours on the $y = 0$ plane. $M_\infty = 0.3$.

Figure 6.7: Predicted near-field SPL from a $L/D = 0.71$ deep cavity configuration.

the inviscid flow prediction given in section 6.2, as this is a good match in the free-stream, along the non-reflecting boundaries. The simulations were performed on the University of Leicester Newton cluster on one 2.2 GHz AMD Opteron processor. This small simulation did not require the MPI parallelization but took over one month to achieve a statistically steady state.

6.3.1 Time-averaged flow

Figures 6.8(a)-(d) and 6.9(a)-(d) show the normalized mean streamwise velocity component of the $L/D = 0.71$ deep cavity configuration at $M_\infty = 0.235$ and $M_\infty = 0.3$ respectively. The cavity diameter to boundary layer thickness ratio in the two test cases at the cavity leading edge is $L/\theta = 65$ and $L/\theta = 62$ respectively. A symmetric recirculation is predicted at $M_\infty = 0.235$. A bound vortex inside the enclosure makes up the main recirculation. This is centred at $(x/L, z/L) = (0, -1.15)$ at the cavity mid-span $y = 0$ and its core bends slightly towards the cavity bottom in the spanwise direction, reaching $(x/L, z/L) = (0, -1.2)$ in the planes $y/L = \pm 0.25$. A secondary recirculation is found at the cavity trailing edge, where $u/u_\infty = 0.2$. In figures 6.8(a) and 6.9(a), the flow accelerates in the $y = 0$ plane towards the center as the flow reaches the cavity opening. This flow velocity is caused by the secondary recirculation that leads the flow upwards and towards the center, accelerating it like in a nozzle. The streamwise velocity iso-contours appear to be discontinuous along 45° lines stemming from the cavity perimeter. This is a numerical artefact of the interpolation used in the post-processing software package Tecplot. The package interpolates the cell-averaged input flow state on a vertex centred mesh. At the internal boundaries, a zero-order interpolation from the domain interior results in a discontinuous velocity field across interior domain boundaries, whereas the cell-averaged flow state across these boundaries was verified to be continuous. Figure 6.9(a) clearly shows the asymmetric shape of the flow recirculation within the enclosure. The flow is ejected in the positive spanwise direction from the $y \geq 0$ side of the opening, whereas it flows into the cavity from the opposite side. The velocity maximum at $M_\infty = 0.3$ is higher than in figure 6.8(a) at $M_\infty = 0.235$ and the ejection is constrained to a smaller area. The corresponding cavity wake is asymmetric, featuring two streamwise velocity local maxima and a local minimum as it develops downstream.

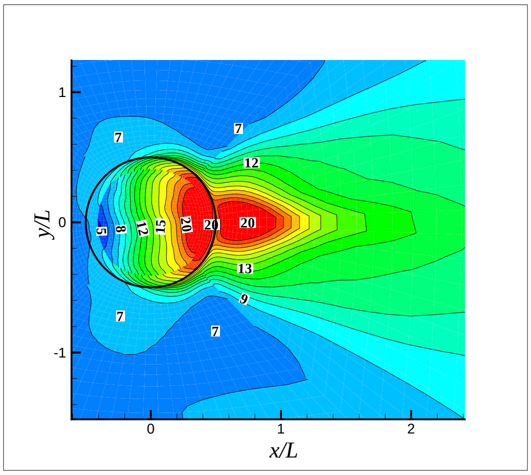

(a) Normalized mean streamwise velocity component u/u_∞ expressed in % in the $z = 0$ plane.

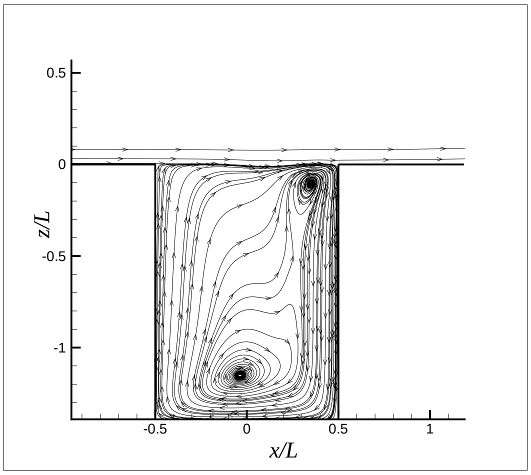

(b) Streamlines in the enclosure in the $y/L = 0$ plane.

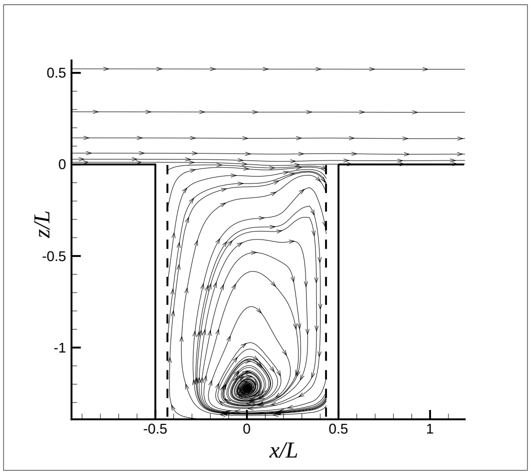

(c) Streamlines in the enclosure in the $y/L = -0.25$ plane.

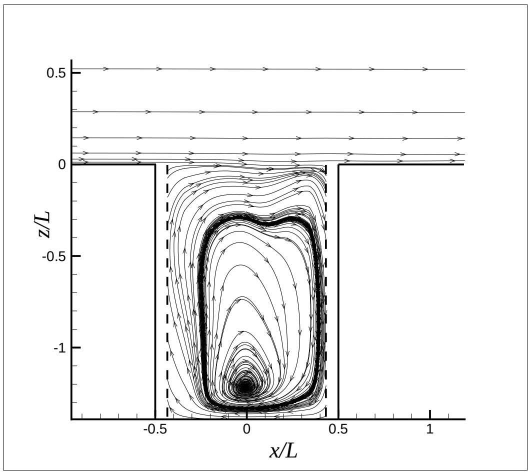

(d) Streamlines in the enclosure in the $y/L = 0.25$ plane.

Figure 6.8: Symmetric recirculation from a $L/D = 0.71$ deep cavity at $M_\infty = 0.235$.

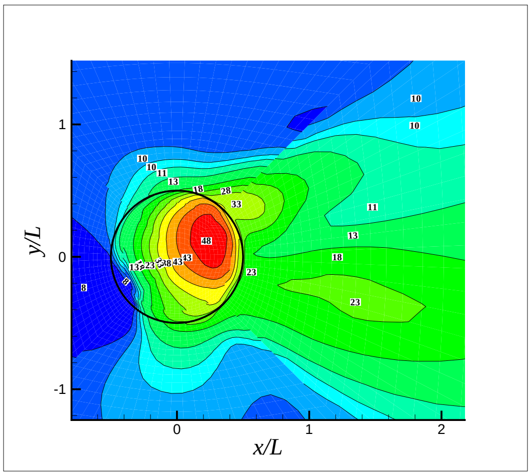

(a) Normalized mean streamwise velocity component u/u_∞ expressed in % in the $z = 0$ plane.

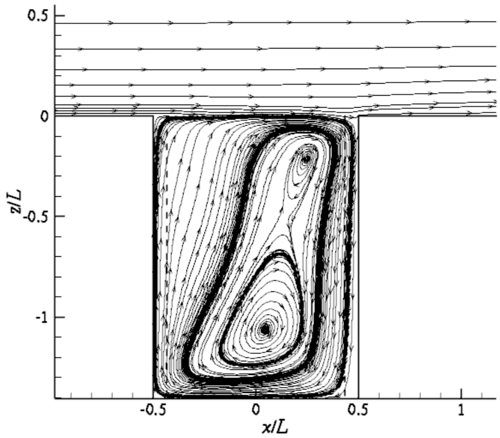

(b) Streamlines in the enclosure in the $y/L = 0$ plane.

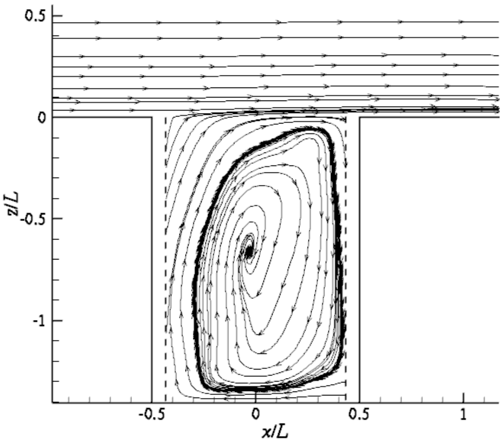

(c) Streamlines in the enclosure in the $y/L = -0.25$ plane.

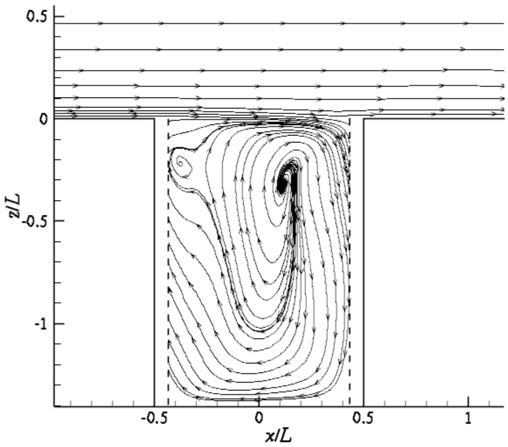

(d) Streamlines in the enclosure in the $y/L = 0.25$ plane.

Figure 6.9: Asymmetric recirculation from a $L/D = 0.71$ deep cavity at $M_\infty = 0.3$.

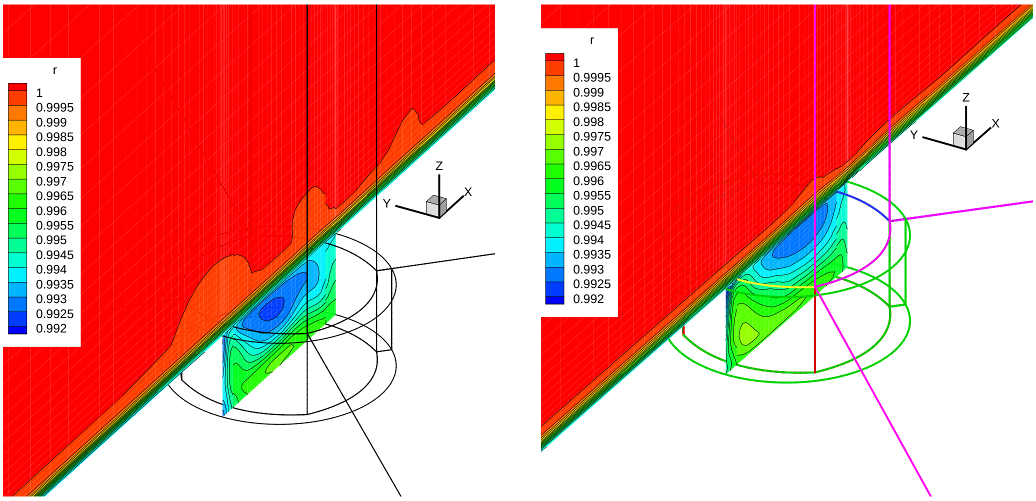

(a) 0.31 million cells baseline mesh.

(b) 50% refined mesh in the cavity.

Figure 6.10: Dimensionless ρ/ρ_∞ iso-contours on the $y = 0$ plane.

Figures 6.9(b) to 6.9(d) show how the main recirculation is oriented in the spanwise direction. This is centred respectively at $(x/L, y/L, z/L) = (-0.055, -0.25, -0.65)$, at $(x/L, y/L, z/L) = (0, 0, -1)$ and at $(x/L, y/L, z/L) = (0.2, 0.25, -0.2)$.

The $L/D = 2.5$ shallow cavity predictions are shown in figures 6.10(a) and 6.10(b). The flow model predicts a steady flow solution, indicating that the laminar cavity is behaving as a lightly damped system at these conditions. The time averaged solution coincides with that in figure 6.10(a). A mesh refinement of 50% was used to check whether the steady flow was the result of the mesh-related numerical viscosity, since the Euler model (Grottadaurea & Rona, 2007a) of the same cavity predicts a self-sustained instability. Although the refined mesh simulation better resolves the symmetric recirculation within the cavity, it also gives a steady flow, as shown in figure 6.10(b).

6.3.2 Aerodynamic instability

In the Euler simulation, it was found that L/D influences the development of the unsteady vortex structure within the cavity. This is also the case for the laminar simulation. Figures 6.11(a) and 6.11(b) show the colour iso-levels of the predicted instantaneous pressure coefficient (Cp) from the laminar cavity model with $L/D = 0.71$, during the mass ejection sequence. Figures 6.11(c) and 6.11(d) shows the same levels during the mass injection sequence. The prediction is characterized by an asymmetric vortex structure with respect to the $y = 0$ plane, as shown by the different streamwise positions of the Cp maximum along the cavity shear layer in figures 6.11(a) and 6.11(b). Vortices alternatively impinge on the cavity rear edge to the left and to the right of the $y = 0$ plane, producing a three-dimensional mass impingement and ejection sequence. Their interaction with the solid edge produces pressure waves. An asymmetric vortex structure has been found by Hering *et al.* (2006) and by Dybenko *et al.* (2006) in their experimental work on a $L/D = 2$ incompressible cylindrical cavity flow at $M_\infty = 0.08$. As the shear layer thickens across the cavity opening, shown in figure 6.12, its interaction with the cavity trailing edge is weaker with respect to the vortex-edge interaction in the Euler model (Grottadaurea & Rona, 2007a). In the laminar simulations, the SPL at $(x, y, z) = (0.5L, 0, 8L)$ is reduced by 3 dB for $L/\theta = 65$ and by 22 dB for $L/\theta = 62$ with respect to the Euler model predictions.

6.3.3 Radiating pressure near-field

In the laminar simulations, the shallow cavity does not display a self-sustained instability. Therefore, a steady-state near field pressure amplitude could not be determined, as the pressure fluctuations are characterized by a small amplitude that is quickly damped by the numerical scheme.

The SPL is evaluated only in the deep cavity configuration at $M_\infty = 0.235$ and at $M_\infty = 0.3$. Figures 6.13(a) and 6.13(b) show the SPL of the $L/D = 0.71$ deep cavity configuration in the streamwise plane $y = 0$ and in the spanwise plane $x = 0$ at $M_\infty = 0.235$. Figures 6.14(a) and 6.14(b) show the corresponding predictions at $M_\infty = 0.3$. The near field pressure fluctuations are characterized by a directivity peak ($\psi = 60°, \phi = 0°$) in the streamwise plane $y = 0$, as shown in figure 6.13(a). The radiating pressure field is symmetric in the spanwise direction, as shown in figure 6.13(b). The noise sources are mainly located at the downstream cavity corner, where the SPL seems to convergence towards, as shown in figures 6.13(a) and 6.14(a). The pressure fluctuation intensity quickly drop by 50 dB as found by comparing the SPL at a distance of $z/L = 5.5$ from the cavity downstream edge to the SPL at $z/L = 1.4$. This

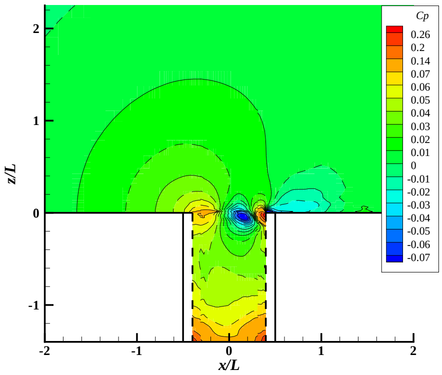

(a) Cp on the $y = -0.3L$ plane. $Cp_{\text{max}} = 0.26$ and $Cp_{\text{min}} = -0.07$.

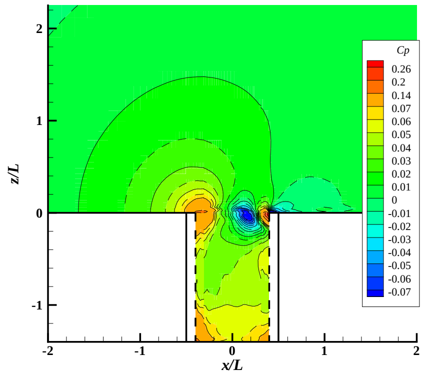

(b) Cp on the $y = 0.3L$ plane. $Cp_{\text{max}} = 0.26$ and $Cp_{\text{min}} = -0.07$.

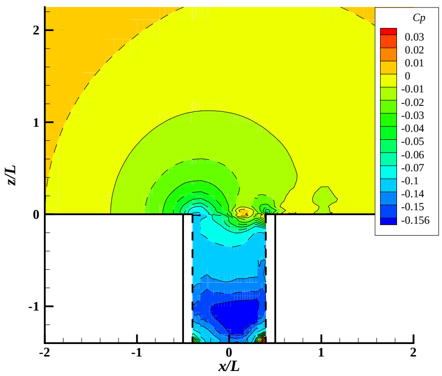

(c) Cp on the $y = -0.3L$ plane. $Cp_{\text{max}} = 0.03$ and $Cp_{\text{min}} = -0.156$.

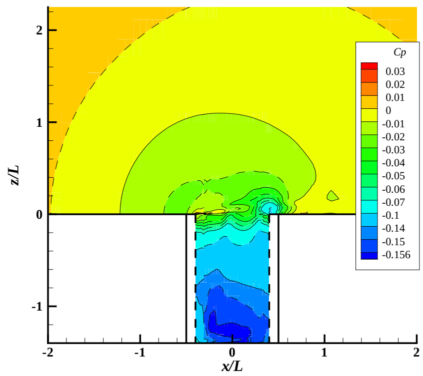

(d) Cp on the $y = 0.3L$ plane. $Cp_{\text{max}} = 0.02$ and $Cp_{\text{min}} = -0.156$.

Figure 6.11: Pressure coefficient during mass ejection and injection. $L/D = 0.71$ deep cavity where $L/\theta = 65$ and $M_\infty = 0.235$. $Cp = (p - p_\infty)/(0.5\rho u_\infty^2)$.

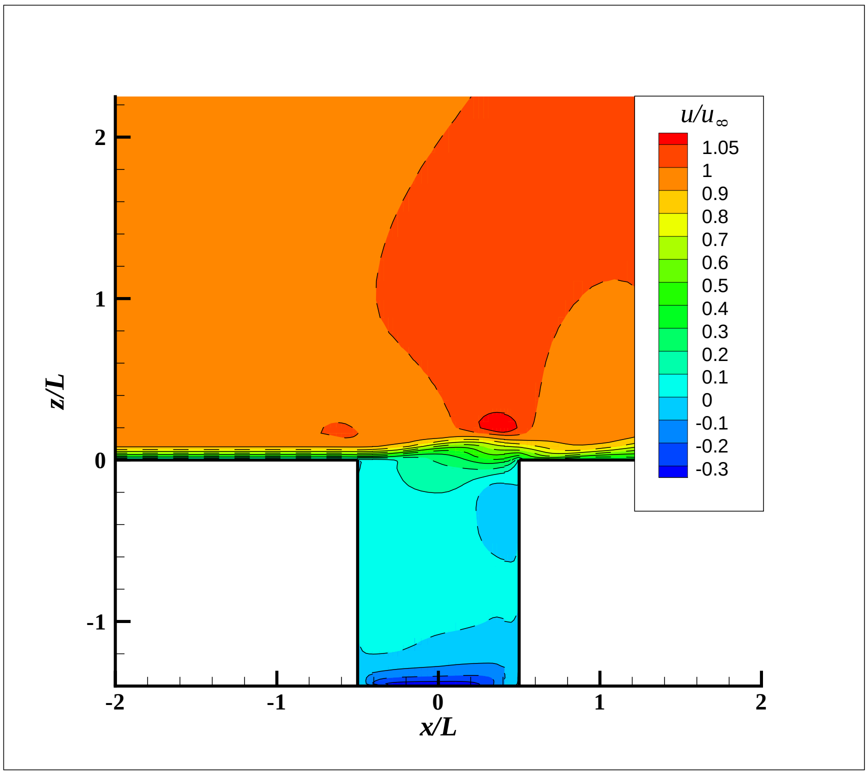

Figure 6.12: Dimensionless streamwise velocity on the $y = 0$ plane.

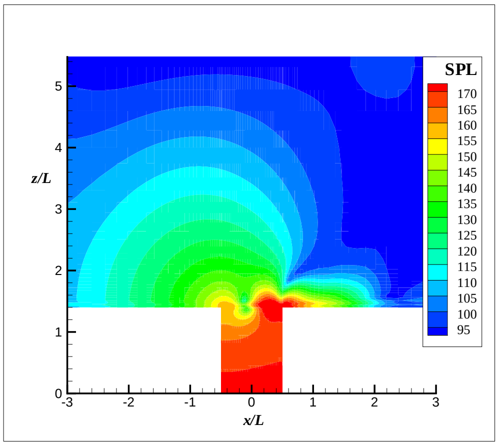

(a) $y = 0$ plane.

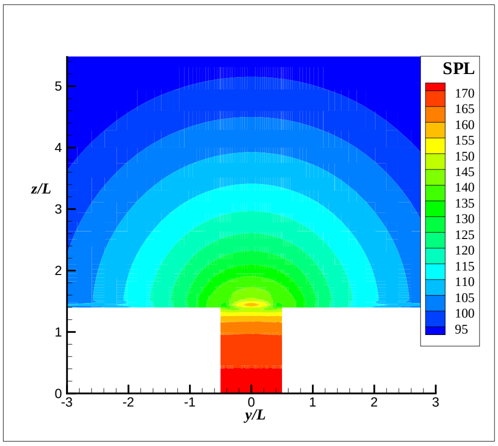

(b) $x = 0$ plane.

Figure 6.13: SPL in the $L/D = 0.71$, $L/\theta = 65$ cavity at $M_\infty = 0.235$. Low Reynolds number model.

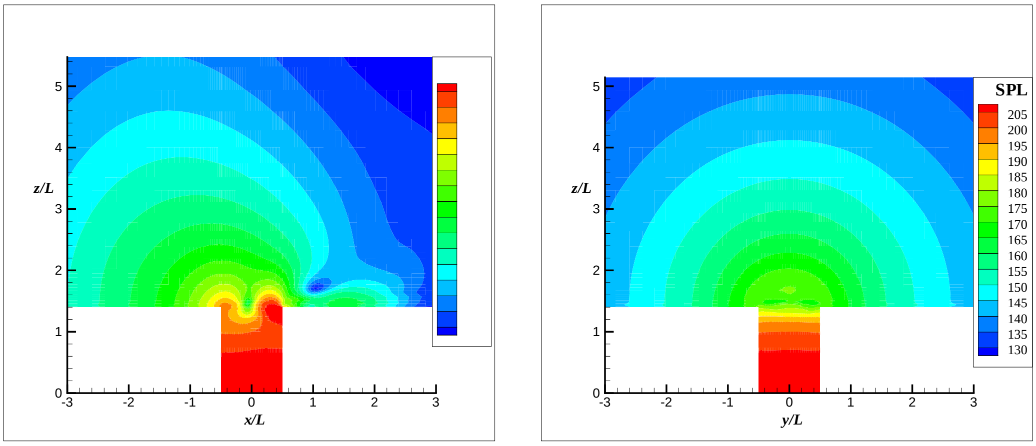

(a) $y = 0$ plane.

(b) $x = 0$ plane.

Figure 6.14: SPL in the $L/D = 0.71$, $L/\theta = 65$ cavity at $M_\infty = 0.3$. Low Reynolds number model.

high reduction is probably not only acoustic in nature but also affected by the hydrodynamic field that surrounds the cavity neighbourhood. The SPL is computed using the root mean square of the pressure fluctuation and hydrodynamic and acoustic pressure are not distinguished in the cavity near-field.

The symmetric directivity of the radiated noise suggests that the mass impingement and ejection of flow to the cavity trailing edge is essentially symmetric either side the $y = 0$ plane. This produces a symmetric distribution of the noise sources at the cavity edge that is responsible for the symmetric far-field noise. A similar reduction in the near-field SPL is found at $M_\infty = 0.3$ in figures 6.14(a) and 6.14(b). The cavity near-field directivity pattern is not affected by the higher velocity and smaller momentum thickness, whereas the radiating pressure intensity is much smaller at the lower speed. To a thicker boundary layer corresponds a reduction in the radiated noise. This was also proven experimentally in a rectangular cavity. Vakili & Gauthier (1991) used mass-injection upstream of a $M_\infty = 1.8$ rectangular cavity to control the shear flow across the cavity to reduce or eliminate cavity oscillations. They observed a significant attenuation in the cavity oscillations by upstream mass-injection. The thickening of the cavity shear layer alters its stability characteristics such that its preferred vortex roll-up frequency falls outside of the natural mode frequency range of the cavity. Lamp & Chokani (1999) used either steady blowing or oscillatory blowing with a zero net mass flux and achieved a 10 dB reduction of the amplitude of the dominant resonant mode. These results suggest that a passive control strategy for a cylindrical cavity can be developed based on the introduction of steady vertical blowing around the cavity circumference.

6.4 Detached Eddy Simulation model

Detached Eddy Simulation (DES) is used to model a $L/D = 0.71$ and a $L/D = 2.5$ cylindrical cavity at $Re_L = 548000$. The computational domain extends $7L$, $7L$ and $8L$ in the streamwise, spanwise and flow-normal directions respectively. The mesh is detailed in section 5.3. The $L/D = 0.71$ geometry is studied in detail and three different mesh refinement levels were tested, 1.4, 2.6 and 9.2 million cells.
The inflow is a thin turbulent boundary layer at $Re_\theta = 8800$. The inflow is modelled using the analytical law of the wake by Rona *et al.* (2009). The profile of the turbulent kinetic energy is obtained using the non-dimensional formula by Marusic & Kunkel (2003) and the density correction at constant pressure is obtained following White (1991). Further details on how the inflow profile is generated are given in appendix B. At the start of the computation, the flow in the computational domain interior is primed with the low Reynolds number solution from section 6.3, to reduce the computational time required to develop a statistically stationary DES prediction with respect to a zero-flow initial condition. The DES computation is then time-marched to allow the turbulent inflow boundary layer to flow across the domain, pushing the laminar boundary layer from the low Reynolds number prediction downstream and out of the computational domain, through the computational domain outflow boundary. Given the CFL constrain and the large number of cells, all turbulent simulations were performed using multi-processor clusters, except the small 1.4 million cells simulation. This was used as the baseline to test the parallelization performance. Simulations using the 2.6 million cell mesh were run at CINECA and on HECToR cluster at HPCx, Edinburgh. The 9.2 million cells model was run on HECToR to a statistically steady state. The mean flow analysis and spectra were obtained for the same simulation at CASPUR. Preliminary result were presented by Grottadaurea & Rona (2008b) of the $L/D = 0.71$ deep cavity and the $L/D = 2.5$ shallow cavity configurations. A cavity of

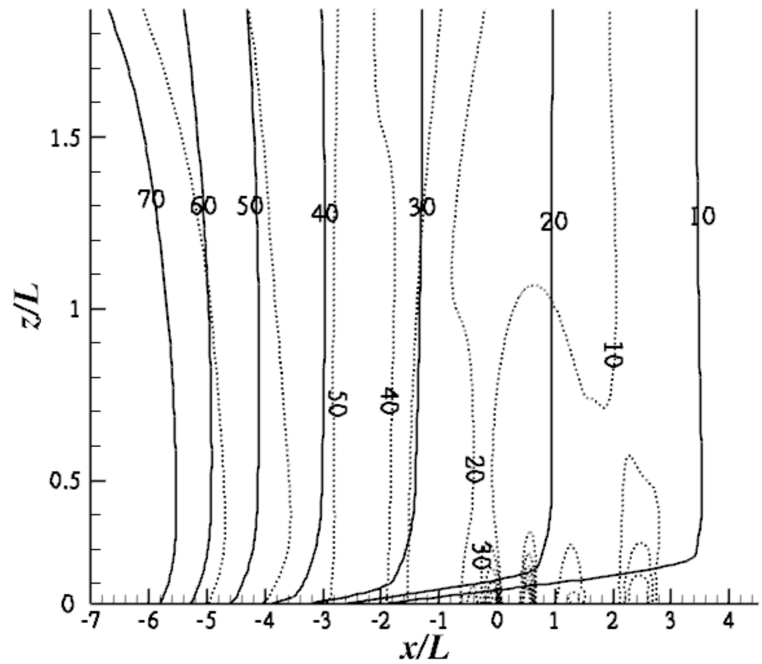

Figure 6.15: $L/D = 0.71$ deep cavity with $Re_L = 548000$ and $M_\infty = 0.235$. $-6.9 < x/L < 4.5$ portion of the computational domain. $p - p_\infty$ is shown and is given in Pa. Dashed lines are used in the $y = 0$ plane and solid lines are used in the $y/L = 6.9$ plane. The contour spacing is $\Delta p = 10$ Pa.

the same aspect ratio and $Re_L = 548000$ has been tested at $M_\infty = 0.1175$ by Verdugo *et al.* (2009).

6.5 Mean flow description

Figure 6.15 shows the mean dynamic pressure $p - p_\infty$ iso-contours in the $L/D = 0.71$ deep cavity in the $-6.9 < x/L < 4.5$ portion of the computational domain at the $y = 0$ and $y/L = 6.9$ planes. Dashed line are used in the $y = 0$ plane and solid line are used in the $y/L = 6.9$ plane. The flow is characterized by a pressure difference of 88 Pa in the computational domain that is given by the pressure drops at the solid wall. The $y = 0$ plane is characterized by pressure spots downstream the cavity trailing edge that convect downstream, exiting the computational domain. Those are convected downstream and exit the computational domain. The cavity also influence the pressure distribution upstream, as expected in subsonic flow.

Figure 6.16 shows the mean normalized velocity iso-contours in the $L/D = 0.71$ deep cavity in the $-6.5 < x/L < 4.5$ portion of the computational domain at the $y = 0$ and $y/L = 6.9$ planes. The region upstream of the cavity $-5 < x/L < 0$ is shown in figure 6.17. Dashed line are used in the $y = 0$ plane and solid line are used in the $y/L = 6.9$ plane. The velocity vector in the $y/L = 6.9$ are also shown to better render the boundary layer growth in this figure. The presence of the cavity affects the inflow boundary layer velocity profile with respect to the freely developing turbulent boundary layer at $y/L = 6.9$. The velocity close to the wall is lower than the theoretical zero pressure gradient turbulent boundary layer profile in the plane $y = 0$. Only at the edge of the boundary layer, where $u \approx u_\infty$, the wake region of the turbulent boundary layer profile is recovered. This gives a higher approaching boundary layer momentum thickness of $L/\theta = 32$ as compared to the target value $L/\theta = 64$.

This change in the turbulent boundary layer is unlikely to determine the staging to a different instability mode with respect to the full-scale airframe cavity but it affects the intensity of the tonal noise radiation.

The cavity is affecting the boundary layer growth rate as clearly shown is figure 6.17, where in the region $-0.5 < x/L < 0$ suddenly the boundary layer growth increases. The increase in the growth rate influences the boundary layer further upstream in the region $-4 < x/L < -0.5$ to give an approaching momentum thickness larger than the one from a zero pressure gradient boundary layer over a solid wall without cavity of the same length. At the domain boundary, the cavity does not affect the boundary layer growth and therefore the boundary layer growth is recovered.

Downstream the cavity rounded edge, $x/L > 0.5$, the boundary layer shows two local maxima where $u/u_\infty = 1$ in the region $0.5 < x/L < 0.7$. This area corresponds to the recirculation bubble downstream of the cavity corner, where the primary and secondary vortices interact.

Figure 6.18 shows a simple sketch of the cavity mean flow. A non-uniform shear layer spans the cavity leading edge. The cylindrical shape of the edge is such that the flow at the cavity mid plane is convected at a slower velocity with respect to the one moving over the sides of the cavity. At the cavity trailing edge, the flow is therefore faster at the cavity sides and slower at the cavity center. This occurs across the cavity span, downstream of the leading edge, at $x/L > -0.5$. Over the range $-0.5 < x/L < 0$,

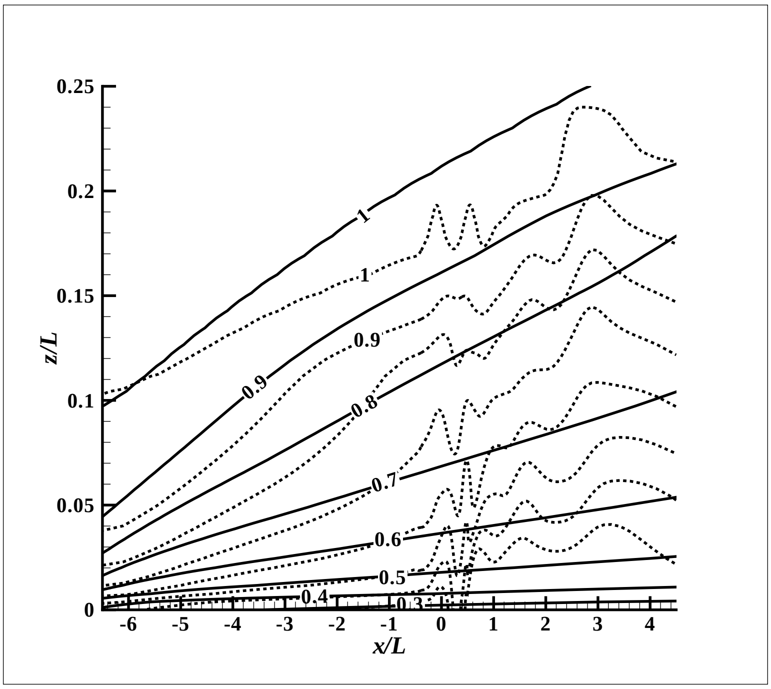

Figure 6.16: $L/D = 0.71$ deep cavity with $Re_L = 548000$ and $M_\infty = 0.235$. $-6.5 < x/L < 4.5$ portion of the computational domain. Normalized mean velocity iso-contours. Dashed lines are used in the $y = 0$ plane and solid lines are used in the $y/L = 6.9$ plane. The contour spacing is $\Delta u/u_\infty = 0.1$.

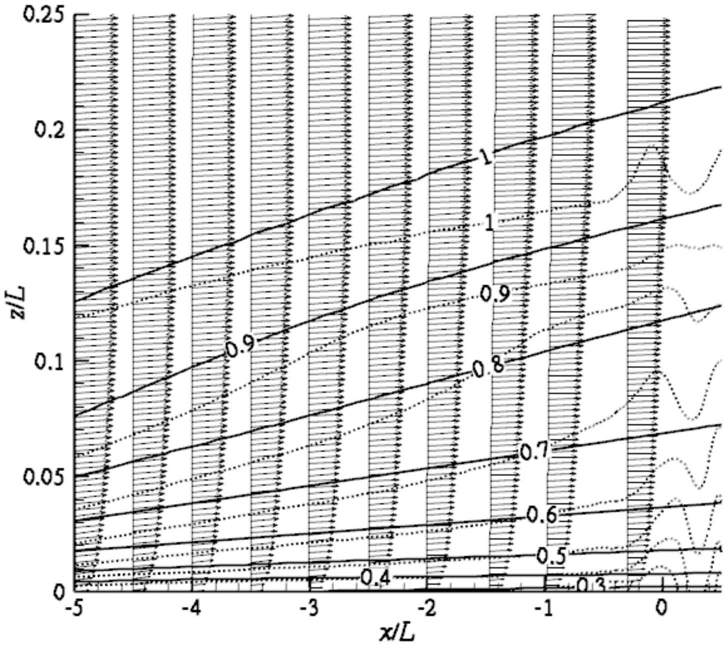

Figure 6.17: $L/D = 0.71$ deep cavity with $Re_L = 548000$ and $M_\infty = 0.235$. $-5 < x/L < 0$ portion of the computational domain.. Normalized mean velocity iso-contours. Dashed lines are used in the $y = 0$ plane and solid lines are used in the $y/L = 6.9$ plane. The contour spacing is $\Delta u/u_\infty = 0.1$. Velocity vectors in the $y/L = 6.9$ plane are shown at a constant $\Delta x/L = 0.5$

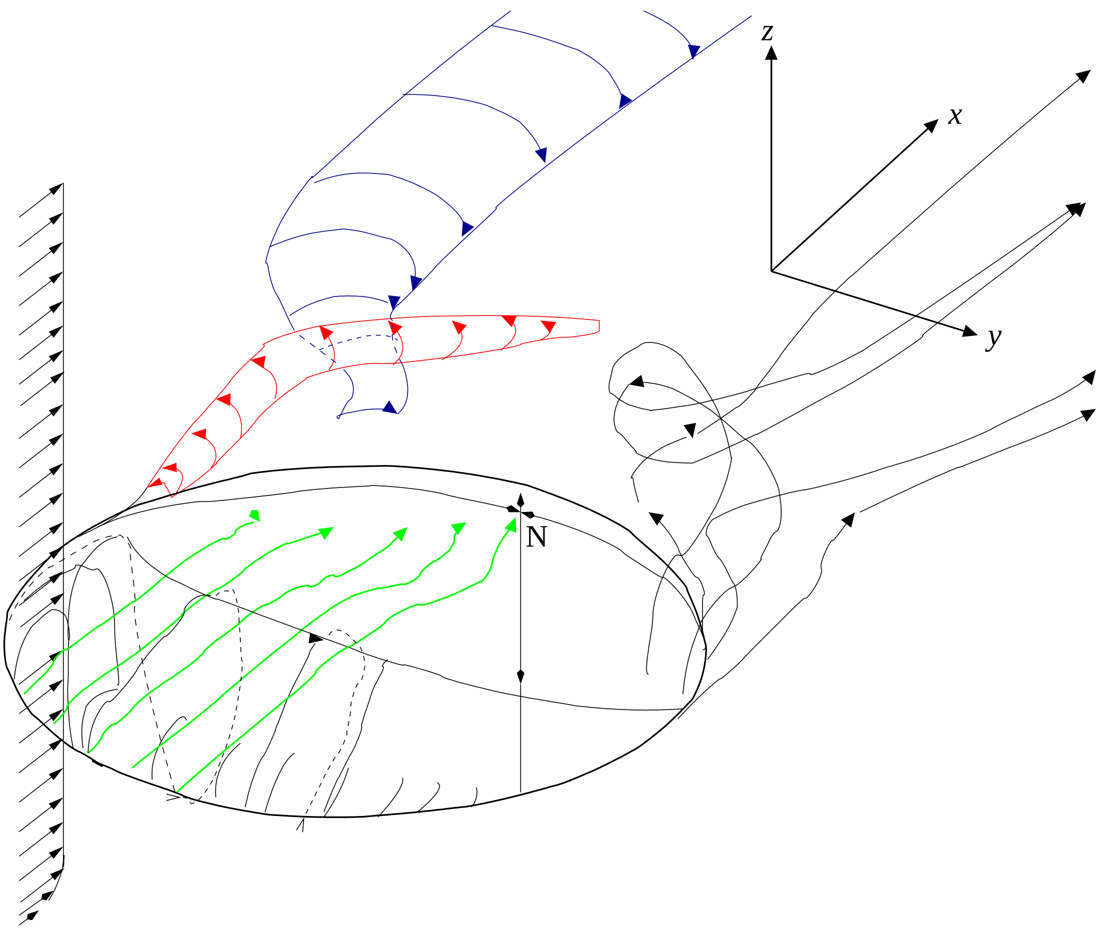

Figure 6.18: Cylindrical cavity sketch. Green streamlines are used in the shear-layer. The secondary recirculation is highlighted using red lines and the primary recirculation is highlighted using blue lines. The incoming turbulent boundary layer and the recirculation in the enclosure are identified with black lines.

the growing shear layer in the mean flow across the cavity opening results in a time-averaged mass injection in the enclosure. Downstream of $x/L = 0$, mass ejection takes place to balance the mass injected over the forward half of the opening.

During mass injection, the centreline flow subsides into the enclosure while the faster side flow moves more tangential to the horizontal surface. Downstream of $x/L = 0$, the mass ejection from the cavity is pushed towards the cavity mid-plane upward. This can be explained by the principle of conservation of momentum. Specifically, the flow at cavity edges is faster as compared to that at the cavity center, therefore it accelerates towards the cavity mid-plane.

As the flow accelerates towards the cavity mid-plane, like in a convergent nozzle, the flow to the sides of it needs to expand to balance the mass flow rate. This expansion coincides with the formation of two primary vortices at the plane $x/L = 0.55$. The cores of the two primary counter-rotating vortices are pushed upwards by the nearby mass ejection. The trajectory of the vortex cores in the downstream portion of the cavity are highlighted in blue in figures 6.18 and 6.19.

Downstream of $x/L = 0$, there is a small flow spill outwards from the sides of the cavity, along the cavity curve edges. This ejection cannot follow the shape of the sharp 90 degrees cavity lip, therefore it separates at the lip line, forming the two secondary recirculations, shown in figures 6.18 and 6.19. These first appear in the predictions at the plane $x/L = 0.22$ as two counter-rotating secondary vortices. These secondary recirculations are then convected upwards by the induced velocity of the primary vortices and meet at the plane $x/L = 0.73$. The two vortices cancel one another and are not detected in the planes $0.73 < x/L < 1$ further downstream. As a result of the primary recirculation, the cavity wake flow is characterized by three zones of low streamwise momentum, which are along the cavity mid-plane and at $y/L = \pm 0.45$ either side of it, as shown in figure 6.19. Figure 6.20 shows the time averaged velocity streamlines in the five spanwise planes $x/L = (0, 0.375, 0.5, 0.65, 1)$. Figure 6.21 shows velocity streamlines in the five streamwise planes $y/L = (0, \pm 0.25, \pm 0.5)$ and on the horizontal plane $z/L = 0.144$.

In figures 6.20(a)-(e), the streamlines are pointing upwards as the time-averaged flow-normal velocity component w is positive, due to the conservation of mass in the streamwise direction. The predicted in-plane velocity streamlines at $x/L = (0, 0.375, 0.5, 0.65, 1)$

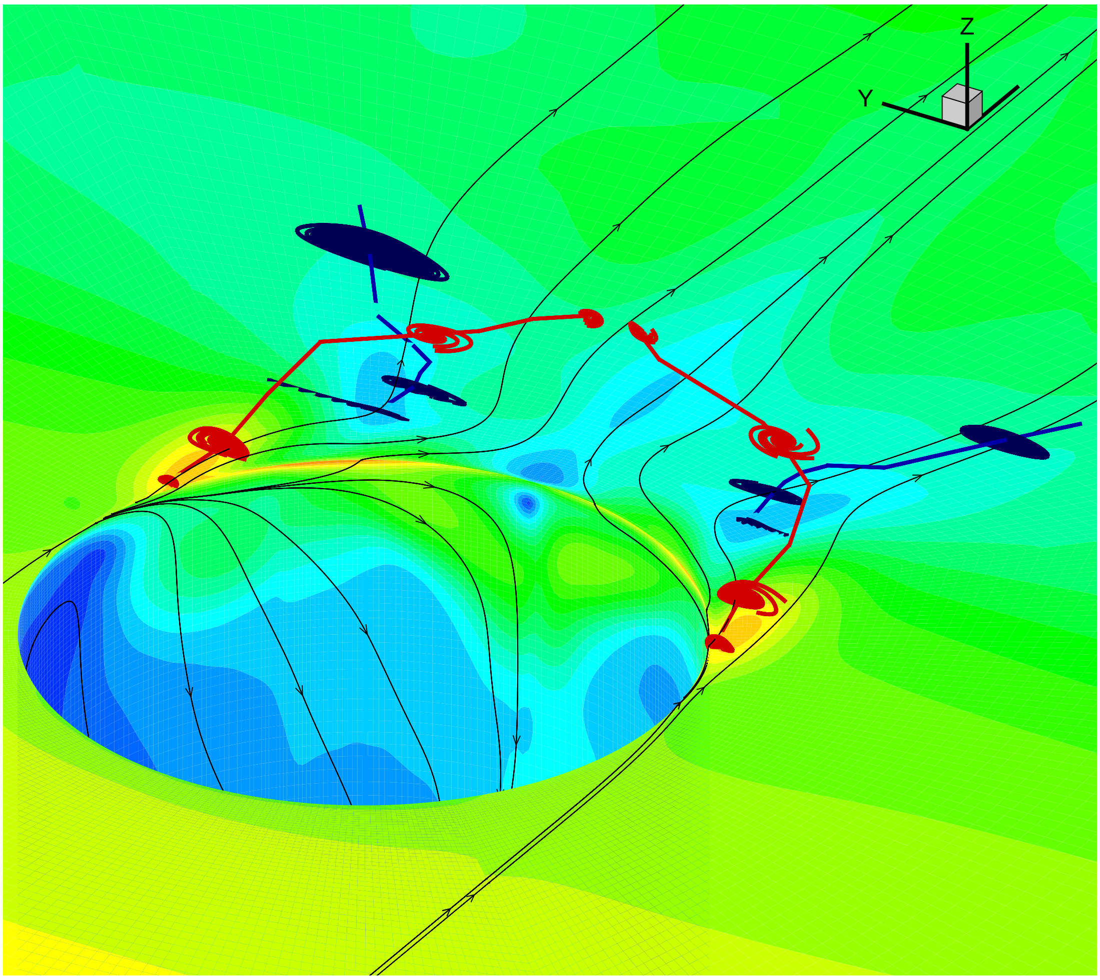

Figure 6.19: Cylindrical cavity mean field and vortex structure evolution.

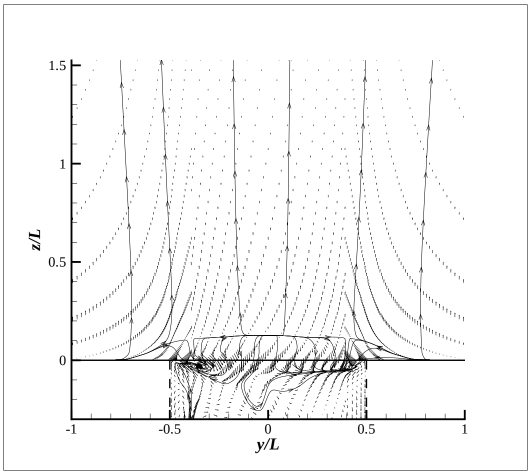

(a) $x = 0$ plane.

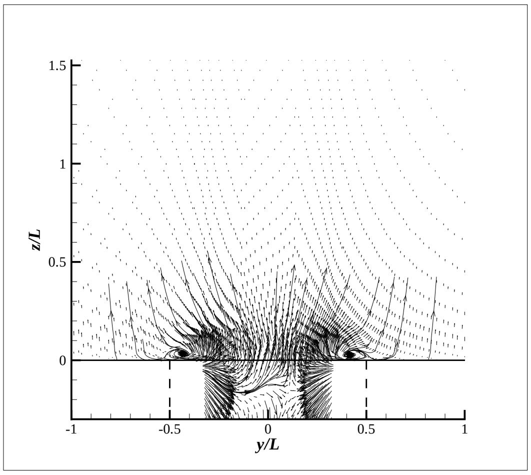

(b) $x/L = 0.375$ plane.

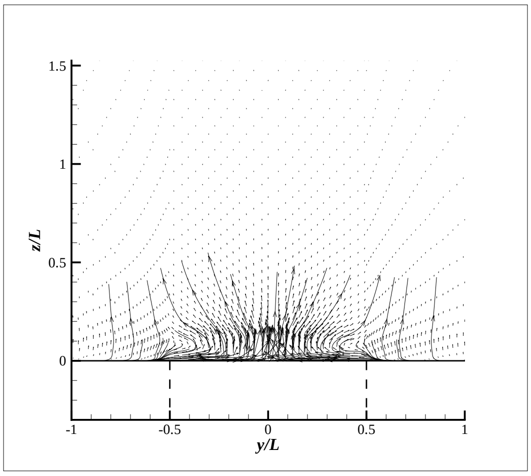

(c) $x/L = 0.5$ plane.

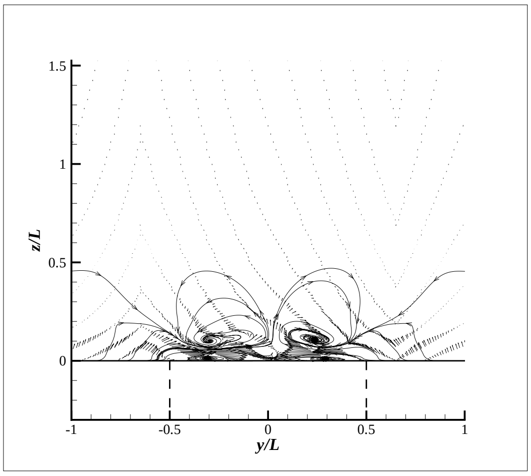

(d) $x/L = 0.65$ plane.

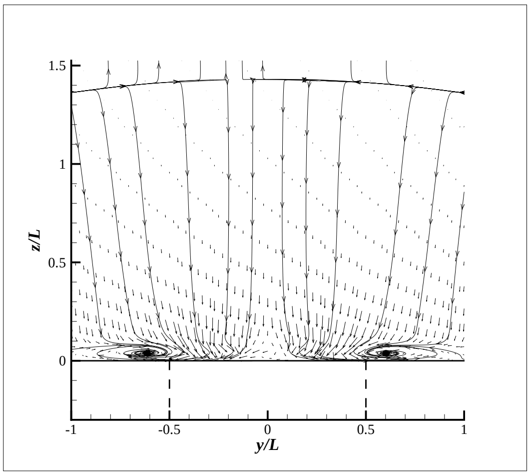

(e) $x/L = 1$ plane.

Figure 6.20: Streamlines and velocity vectors on spanwise planes. Only one vector every ten is shown for clarity.

	$\mathbf{x}_1$		$\mathbf{x}_2$	
x/L	y/L	z/L	y/L	y/L
0.556	0.311	1.430	-0.314	1.430
0.633	0.295	1.437	-0.310	1.439
0.667	0.304	1.442	-0.310	1.442
0.7	0.309	1.442	-0.319	1.444
0.733	0.357	1.439	-0.343	1.446
0.767	0.437	1.448	-0.418	1.448
0.9	0.530	1.457	-0.544	1.467
1	0.607	1.467	-0.610	1.464

Table 6.1: Primary vortex core locations. $L/D = 0.71$ deep cavity at $M_\infty = 0.235$ and $L/\theta = 32$.

in figure 6.19 indicate the presence of two essentially symmetric counter-rotating primary vortices either side of the $y = 0$ cavity centreline. These are centred at $(y/L, z/L)$ = (±0.45, ±0.033) in the plane $x/L = 0.22$. The vortex cores rise above the cavity and spread away from one another downstream, as these primary vortices grow in size, as diagrammatically shown in figure 6.18. This results in the vortex cores being centred at $(y/L, z/L) = (\pm, 0.45 \pm 0.025)$ in the plane $x/L = 0.375$, at $(y/L, z/L) = (\pm 0.45, \pm 0.025)$ in the plane $x/L = 0.5$, $(y/L, z/L) = (\pm 0.45, \pm 0.055)$ in the plane $x/L = 0.65$ and at $(y/L, z/L) = (\pm 0.65, \pm 0.055)$ in the plane $x/L = 1$.
At $x/L = 0.65$, figure 6.20(d), two additional secondary vortices are shown external to the counter-rotating primary vortex pair, centred at $(y/L, z/L) = (\pm 0.25, \pm 0.15)$. The position vectors $\mathbf{x}_1$ and $\mathbf{x}_2$ of each vortex core on different spanwise planes are listed in tables 6.1 and 6.2. These tables summarize the positions of the primary and secondary vortex cores and how these vary in the downstream direction. Figure 6.19 explains how the two vortex pairs interact and how the flow is shaped over the cavity opening and downstream of the cavity edge. Figure 6.19 shows the roll-up of the two primary vortices at the plane $x/L = 0$, about a tenth of a diameter inbound from the cavity edge, where the streamlines converge to a point. Inside the enclosure, a main recirculation is present, as suggested by the confluence of downward streamlines on the rear cavity wall in figure 6.19. The vortex core of the main recirculation is found at $(x/L, z/L) = (-0.2, -0.5)$ inside the cavity. The vortex cores of the two secondary vortices are first detected downstream of the cavity center at $(x/L, z/L) = (0.6, 0.055)$. These are then

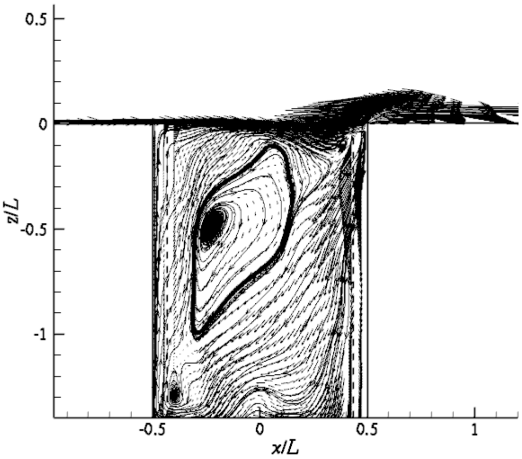

(a) $y = 0$ plane.

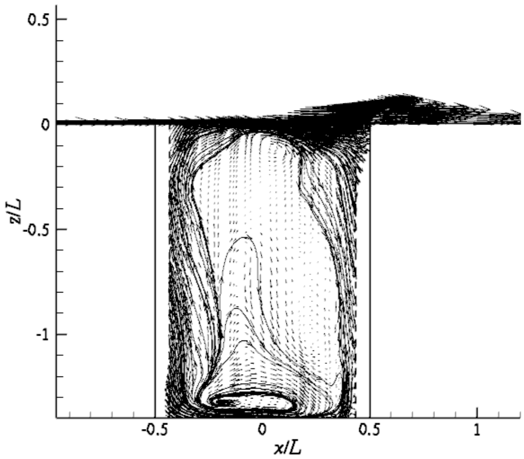

(b) $y/L = -0.25$ plane.

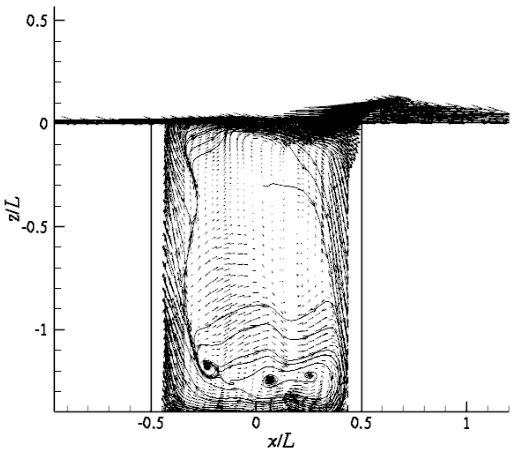

(c) $y/L = 0.25$ plane.

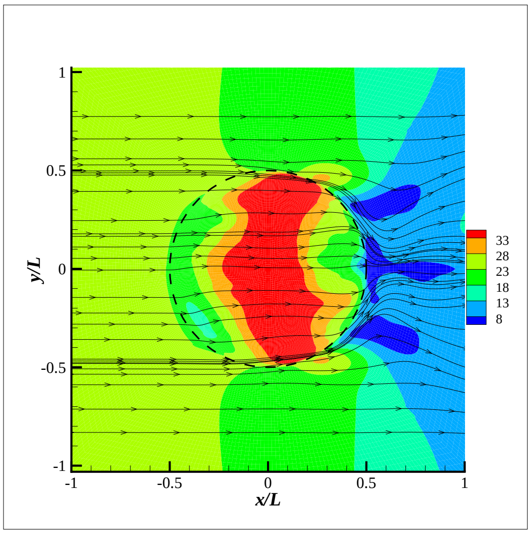

(d) $z/L = 0.0002$ plane.

Figure 6.21: Streamlines and velocity vectors on spanwise planes. Streamlines and velocity magnitude iso-levels from the plane above the enclosure in the $z/L = 0.0002$ plane. Only one vector every ten is shown for clarity. A threshold on the velocity magnitude is applied, $u/u_\infty > 0.5$ is not shown.

	$\mathbf{x}_1$		$\mathbf{x}_2$	
x/L	y/L	z/L	y/L	y/L
0.222	0.463	1.433	-0.458	1.433
0.333	0.435	1.448	-0.436	1.451
0.444	0.428	1.480	-0.451	1.489
0.556	0.406	1.518	-0.418	1.523
0.633	0.271	1.532	-0.323	1.527
0.667	0.205	1.541	-0.272	1.530
0.7	0.134	1.566	-0.078	1.561
0.733	0.066	1.575	-0.023	1.575

Table 6.2: Secondary vortex core locations. $L/D = 0.71$ deep cavity at $M_\infty = 0.235$ and $L/\theta = 32$.

shown moving inbound towards the $y = 0$ cavity mid-span plane downstream of the cavity trailing edge.

6.5.1 Aerodynamic instability

From the starting flow condition detailed in section 6.4, the simulation is time-marched to $26L/u_\infty$ to allow a self-sustained cavity flow instability to develop. A fully developed instability is characterized by a statistically stationary flow. This condition is reached at $22.4L/u_\infty$, as indicated by the predicted wall pressure history of figure 6.22, where the predicted wall pressure oscillation over the period $7 \leq tu_\infty/L \leq 12$ closely matches the oscillation over the subsequent period $16.5 \leq tu_\infty/L \leq 21.5$, as shown in figure 6.22(b). Figure 6.22(a) shows that the cavity wall pressure fluctuation is a convolution of two main modes, a dominant instability mode and a lower frequency and lower amplitude mode. In figure 6.22(b), the two modes have been separated using a low-pass and a band-pass filter, respectively. The dash-dotted line displays the low frequency low intensity mode. The higher amplitude mode, shown by the solid line, is the main instability mode at $St = 0.512$ that is within 12 % of the first mode predicted by the modified Rossiter equation of Block (1976) and within 15 % of the acoustic resonant mode of a flanged pipe (Rayleigh, 1894). The sequence of figures 6.23(a)-(d) shows four snapshots of the flow in the enclosure and immediate surroundings. A small portion of the full computational domain $(\pm 0.6L, \pm 0.6L, L)$ is visualized near the

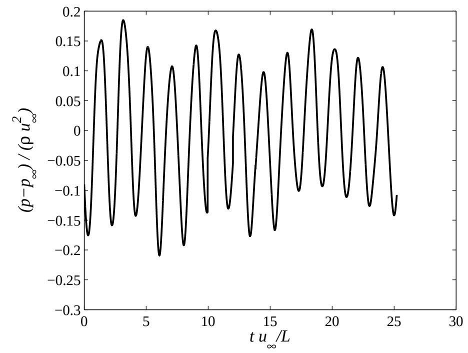

(a) Original sampled signal.

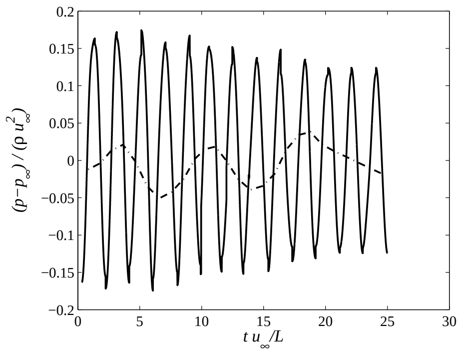

(b) Filtered signal. A dashed-dotted line is used for the low frequency mode and a solid line for the main instability mode.

Figure 6.22: Wall pressure probe located at $(x/L, y/L, z/L) = (0.5, 0, 0.7)$, pressure is normalized by $\rho_\infty u_\infty^2$ and the time by L/u_∞. $L/D = 0.71$ cavity at $M_\infty = 0.235$ and $L/\theta = 32$.

cavity. The four snapshots are a time sequence that shows the interaction of convected vorticity at the top of the enclosure with the cavity downstream edge. The interaction takes place over a period $\mathcal{T} = 0.7745L/u_\infty$. The unsteady recirculation pattern in each snapshot is visualized by the tracing of streamlines in the Favre averaged velocity field. The $L/D = 2.5$ shallow cavity is characterized by a large recirculation in the enclosure. A shear layer spans across the cavity opening. In the shear flow, the streamlines identify the presence of a downstream convecting vortex, which is shown in figure 6.23(b) centred at $x = 0.35L$ and $z = 0.875D$. The convecting vortex size is smaller with respect to the main recirculation inside the enclosure, centred at about $x = 0.23L$ and $z = 0.5D$. As it approaches the downstream wall in figure 6.23(b), the vortex strength appears to increase, as indicated by the packing of the streamlines. The interaction of the convected vortex with the cavity trailing edge produces pressure waves (Powell, 1964) that radiate to the far-field, where they are perceived as aerodynamic noise. The $L/D = 2.5$ shallow cavity flow is found to have a dominant instability mode at $St = 1.332$ at $M_\infty = 0.235$. The maximum reverse flow velocity inside the enclosure is $u = -37$ m/s. The sequence of figures 6.24(a)-(d) shows short-time averaged flow snapshots from the $L/D = 0.713$ deep cavity simulation at $M_\infty = 0.235$, taken at increasing computational time. The velocity field is visualized by the tracing

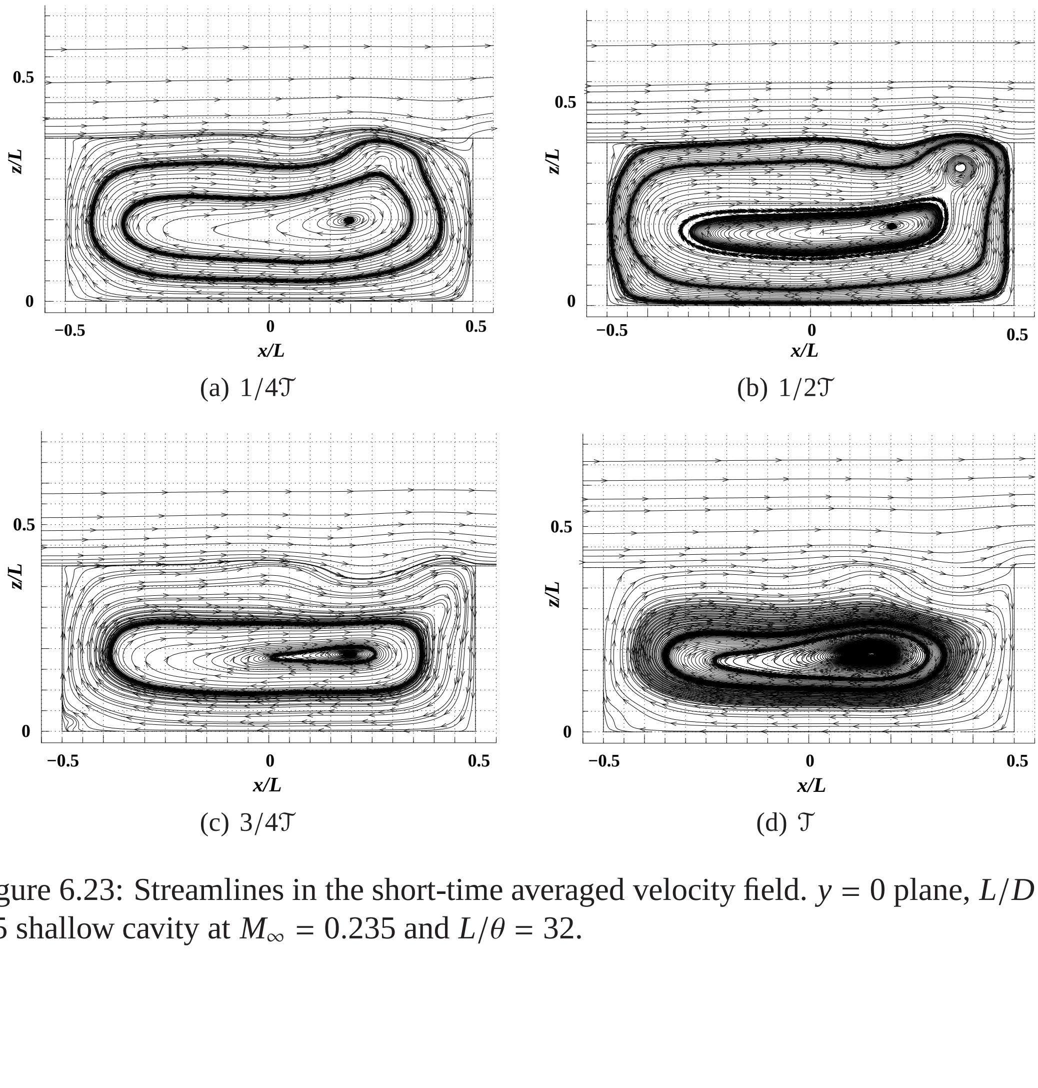

(a) $1/4\mathfrak{T}$ (b) $1/2\mathfrak{T}$

(c) $3/4\mathfrak{T}$ (d) $\mathfrak{T}$

Figure 6.23: Streamlines in the short-time averaged velocity field. $y = 0$ plane, $L/D = 2.5$ shallow cavity at $M_\infty = 0.235$ and $L/\theta = 32$.

of streamlines in the Favre averaged flow. The four snapshots show a time-dependent vortex structure. The vortex structure evolves over a much longer period $\mathcal{T} = 1.853$ in the $L/D = 0.713$ deep cavity with respect to the $L/D = 2.5$ shallow cavity. Two additional smaller recirculation zones are identified at the bottom cavity corner and just under the leading edge of the cavity, where the upstream boundary layer separates, as shown in figure 6.23(a). The dominant instability mode corresponds to $St = 0.539$ in the $L/D = 0.71$ cavity at $M_\infty = 0.235$. The maximum reverse flow velocity inside the enclosure is approximately $u_1 = -51$ m/s. A similar instability to the inviscid one (Grottadaurea & Rona, 2007a) is predicted by this model. The Euler model gave a main instability mode that corresponds to $St = 0.53$. This suggest that the dominant cavity flow instability is convective and inviscid in nature.

Figures 6.25(a)-(d) show short-time averaged snapshots of the $L/D = 0.713$ deep cavity simulation at $M_\infty = 0.235$, modelled using a computational mesh of 9.2 million cells. This is a finer mesh compared to the 2.6 million cell grid used to obtain figures 6.24(a)-(d). Four snapshots are shown in figure 6.25, which are evenly distributed in time over one cavity instability characteristic period $\mathcal{T}$. In this refined mesh model, the mean flow is symmetric about the cavity mid-span. Figure 6.25 displays the time-evolving flow on this plane of symmetry $y = 0$. Similarities with two-dimensional simulations of rectangular cavities by Colonius *et al.* (1999), by Rowley *et al.* (2002), and by Yao *et al.* (2004) are identified in this figures. In particular, in figure 6.25(a) two small vortex structures are identified in the shear layer spanning across the cavity open end. Figure 6.25(a) shows one vortex rolling-up at the cavity leading edge while the other one is impinging at the cavity trailing edge. The vortex structures are three-dimensional in nature and behaviour and their interaction with the main recirculation inside the cavity appears to be weak at $t = 1/5\mathcal{T}$. This interaction strengthens later in the main instability mode period $\mathcal{T}$, as shown in figures 6.25(b) to 6.25(d), where the vortex structure shed from the leading edge is convected downstream while it interacts with the main recirculation. Small vortices are found at the cavity upstream bottom corner, close to the floor. These result from the flow separation induced by the main recirculation. This pushes the flow upstream along the cavity floor and then upwards along the cavity upstream wall. This motion segregates a small recirculating flow region at the upstream bottom corner. As the upstream moving flow separates from the cavity floor, vortex structures are created that convect upwards and along the cavity

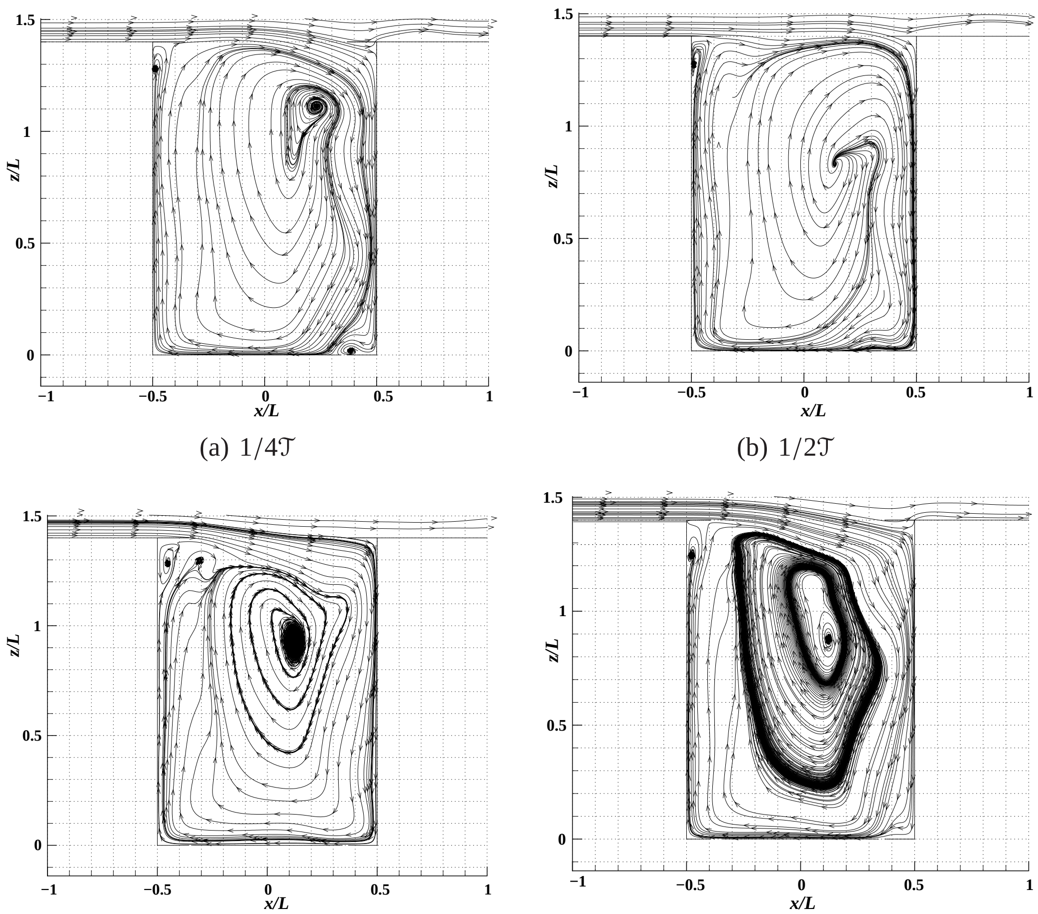

(a) $1/4\mathfrak{T}$ (b) $1/2\mathfrak{T}$

(c) $3/4\mathfrak{T}$ (d) $\mathfrak{T}$

Figure 6.24: Streamlines in the short-time averaged velocity field. $y = 0$ plane, $L/D = 0.713$ deep cavity at $M_\infty = 0.235$ and $L/\theta = 32$. 2.6 million cells medium mesh.

span, with either a positive or a negative spanwise convection speed. Figure 6.25(d) shows a small vortex located at $(x/L, z/L) = (0.55, 1.45)$. The flow separates as it is ejected from the cavity opening, due to the local adverse pressure gradient. The shearing of the ejected vortex over the downstream cavity lip generates aerodynamic noise, according to the theory of Powell (1964). The flow then reattaches downstream of the cavity, as shown in figures 6.25(b) to 6.25(d).

The flow pattern from the 9.2 million cells model, shown in figures 6.25(a)-(d), is similar to the one obtained from the 2.6 million cells simulation, in figures 6.24(a)-(d). The 9.2 million cells refined mesh better resolves the small vortical structures across the cavity opening and near the cavity floor. It allows to observe vortex shearing over the cavity rear edge, showing the physical process of aerodynamic noise generation in the cavity through the theory of Powell (1964).

6.5.2 Radiating pressure near-field

Figures 6.26(a)-(d) and 6.27(a)-(d) show the near-field pressure fluctuations in the $L/D = 2.5$ shallow cavity and in the $L/D = 0.713$ deep cavity, respectively. In figures 6.26(a)-(d) and 6.27(a)-(d) only a portion of the computational domain of extent $(\pm 7L, \pm 7L, 9L)$ is shown. Outside this area, the pressure waves are damped by the rapid mesh stretching. Contours of static pressure fluctuation, $p' = p - p_\infty$ are shown by ten solid lines ($p' \geq 0$) and nine dashed lines ($p' < 0$). The contour spacing $\Delta p' = 2$ Pa in the $L/D = 2.5$ shallow cavity and $\Delta p = 5$ Pa in the $L/D = 0.713$ deep cavity. In figures 6.26(a) and 6.27(a), the largest amplitude time-dependent pressure fluctuation is shown inside the enclosure and just above the downstream bulkhead. These fluctuations are hydrodynamic in nature and are associated to the generation of vorticity in the shear layer spanning the cavity opening. This vorticity is injected and ejected alternatively at the cavity trailing edge and the ejected structures convect over the downstream bulkhead. The pressure fluctuation associated to these vorticity clusters is shown by small clusters of packed contour lines in figures 6.26(a) and 6.27(a) along the cavity rear bulkhead. The region where hydrodynamic pressure fluctuations are dominant is highlighted in figures 6.26(a) and 6.27(a) by a dashed line rectangle.

Outside this region, the contours of pressure fluctuation show larger structures. The time sequence of figures 6.26(a)-(d) and 6.27(a)-(d) shows these structures radiating

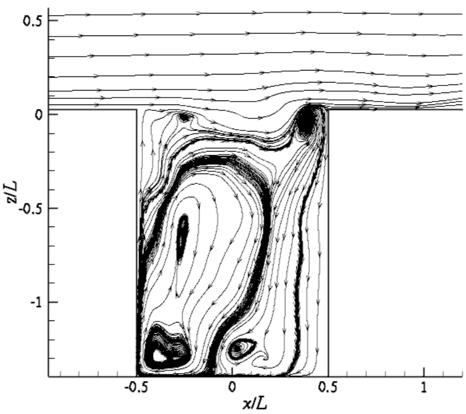

(a) 1/5$\mathfrak{T}$

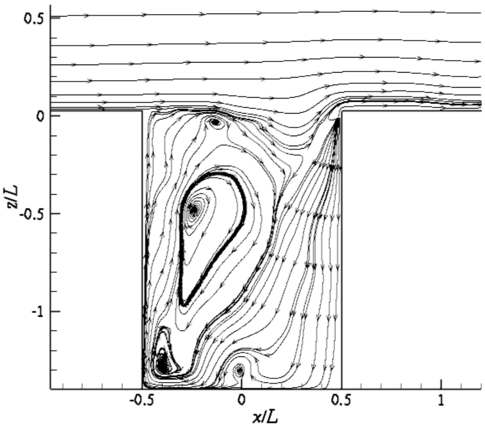

(b) 2/5$\mathfrak{T}$

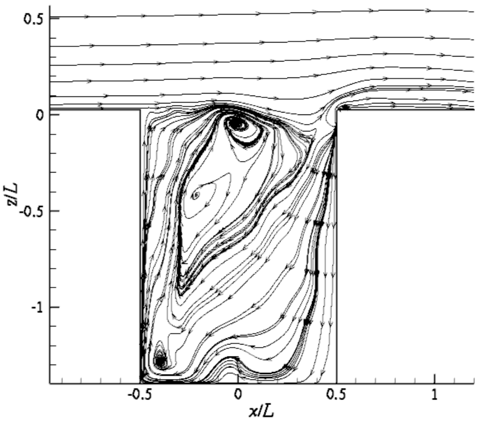

(c) 3/5$\mathfrak{T}$

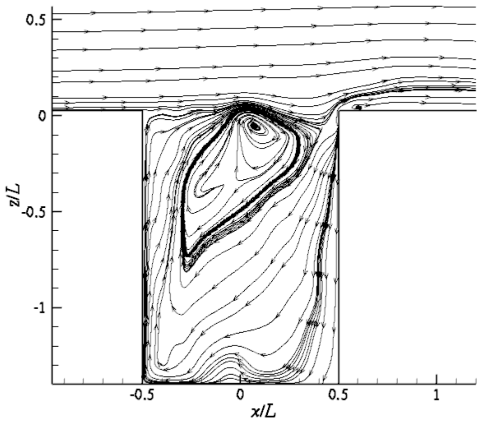

(d) 4/5$\mathfrak{T}$

Figure 6.25: Streamlines in the short-time averaged velocity field. $y = 0$ plane, $L/D = 0.713$ deep cavity at $M_\infty = 0.235$ and $L/\theta = 32$. 9.2 million cells fine mesh.

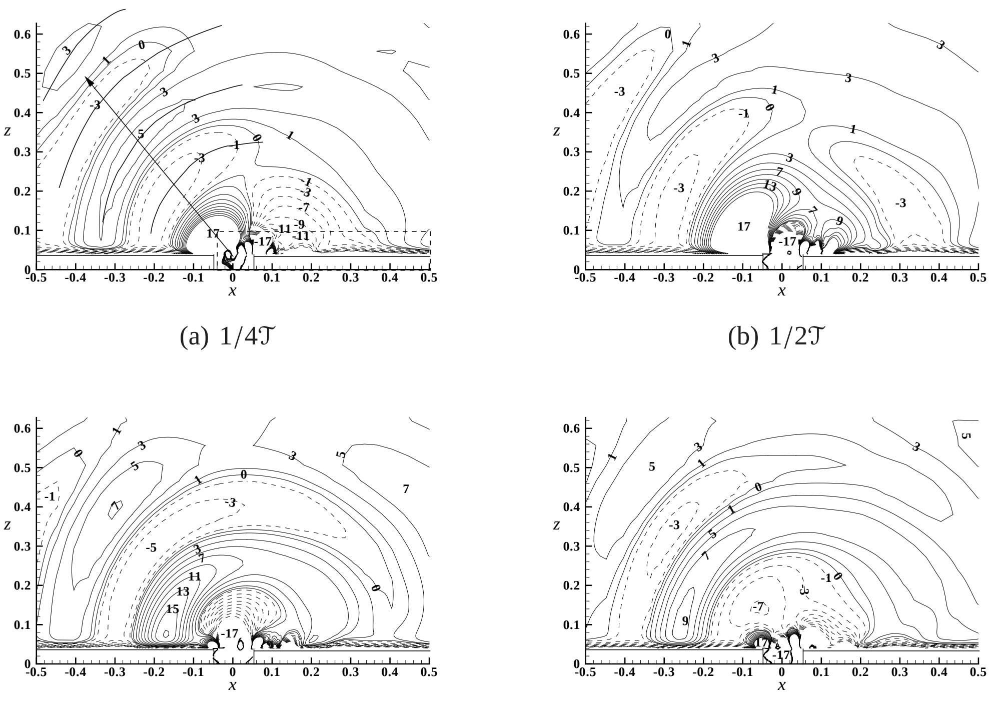

(a) $1/4\mathcal{T}$ (b) $1/2\mathcal{T}$

(c) $3/4\mathcal{T}$ (d) $\mathcal{T}$

Figure 6.26: Pressure fluctuation iso-contours in Pa. $y = 0$ plane, $L/D = 2.5$ shallow cavity at $M_\infty = 0.235$ and $L/\theta = 32$.

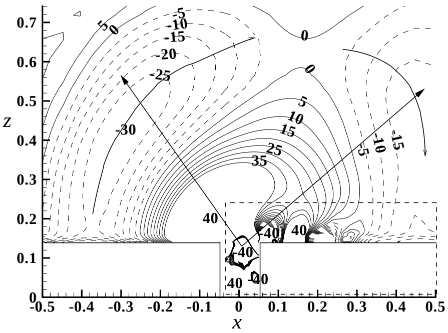

(a) 1/4$\mathfrak{T}$

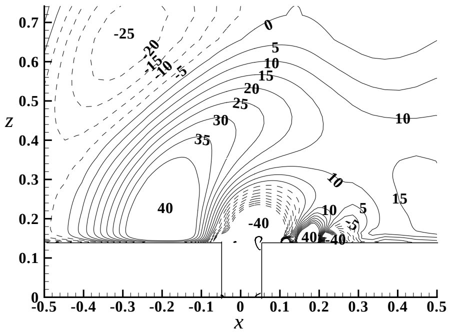

(b) 1/2$\mathfrak{T}$

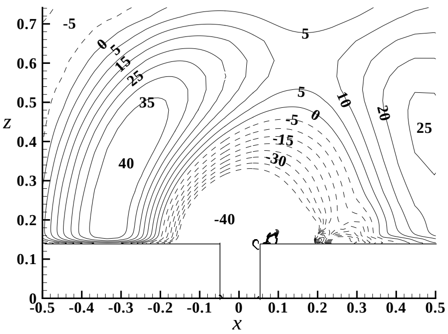

(c) 3/4$\mathfrak{T}$

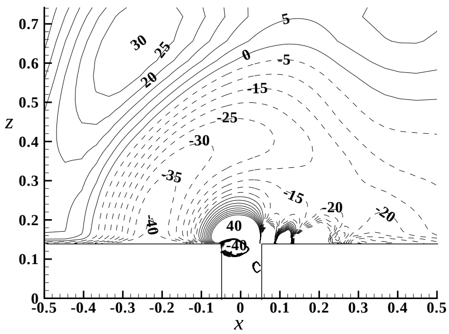

(d) $\mathfrak{T}$

Figure 6.27: Pressure fluctuations iso-contours in Pa. $y = 0$ plane, $L/D = 0.713$ deep cavity at $M_\infty = 0.235$ and $L/\theta = 32$.

away from the enclosure. The fluctuations of pressure in this area are due to the cavity acoustic radiation and the contours here describe the acoustic near-field. In figure 6.26(a), an acoustic wave-front is shown propagating in the upstream direction. The position of this wave-front is marked by a continuous thick arc. This suggests that, in the $L/D = 2.5$ cavity, the main radiation is directed upstream.

In figure 6.27(a), two acoustic fronts are identified in the near-field of the $L/D = 0.713$ deep cavity. There is a dominant upstream radiation, just like in the $L/D = 2.5$ cavity, that is accompanied by a downstream pressure front, which is peculiar to the $L/D = 0.713$ deep cavity.

The pressure field associated to the $L/D = 2.5$ shallow cavity is characterized by a lower amplitude fluctuation with respect to the $L/D = 0.71$ deep cavity, consistently with the previous inviscid simulations by Grottadaurea & Rona (2007a). Specifically, the highest positive contour away from the cavity where the near-field acoustic radiation dominates is 15 Pa, as shown in figure 6.26(c). The largest positive acoustic near-field pressure fluctuation contour in the $L/D = 0.71$ predictions is 40 Pa, as shown in figure 6.27(c).

The near-field Sound Pressure Level (SPL) has been estimated by averaging the time-resolved pressure predictions over one fundamental period of cavity flow instability $\mathcal{T}$. $N = 43$ frames are used from the $L/D = 2.5$ shallow cavity simulation and $N = 72$ frames from the $L/D = 0.71$ deep cavity simulation.

$$\mathrm{SPL} = 20\log\left(p_{rms}/p_0\right) \tag{6.1}$$

$$p_{rms} = \sqrt{\frac{1}{N}\sum_{i=1}^{N}(p_i - \overline{p})^2} \tag{6.2}$$

In equation 6.2, the reference pressure is $p_0 = 20\ \mu$Pa, p_{rms} is the root mean square pressure fluctuation and $\overline{p} = (1/N)\sum_{i=1}^{N} p_i$ is the ensemble averaged pressure taken over the N frames.

Figures 6.28(a)-(b) and 6.29(a)-(b) show SPL iso-contours in the $L/D = 2.5$ shallow cavity and in the $L/D = 0.713$ deep cavity respectively. The contour spacing is ΔSPL = 5dB. Figures 6.28(a) and 6.29(a) show the SPL iso-contours in the $\phi = 0°$ plane and figures 6.28(b) and 6.29(b) show the SPL iso-contours in the $\phi = 90°$ plane.

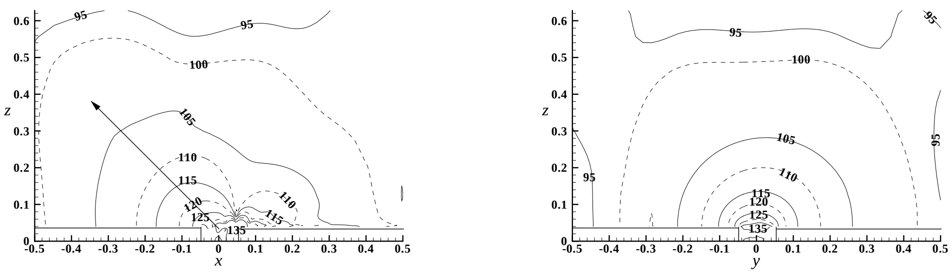

(a) $\phi = 0°$ (b) $\phi = 90°$

Figure 6.28: Contours of near-field SPL, dB re 20μPa. $L/D = 2.5$ shallow cavity at $M_\infty = 0.235$ and $L/\theta = 32$.

The $L/D = 2.5$ cavity shows the main acoustic radiation being in the direction of ($\psi = 126°, \phi = 0°$), as shown in figure 6.28(a). In the spanwise plane, the predicted sound wave is asymmetric with respect to the cavity mid-span, with a stronger radiation at the azimuthal angle $\psi = 60°$ at $\phi = 90°$, as shown in figure 6.28(b). At the same radial distance, the deep cavity acoustic near-field is about 15dB re 20 μPa louder with respect to the shallow cavity. For instance, the 100 dB contour in figure 6.28(b) covers about the same position as the 115 dB contour in figure 6.29(b). As noted in the near-field pressure fluctuation contours of figure 6.27(a), the deep cavity has two preferential directivity directions for the near-field acoustic radiation. The SPL contours of figure 6.29(a) enable to estimate the directions of preferential radiation in the $\phi = 0°$ plane. These are at an azimuthal angle $\psi = 114°$ in the upstream direction and at $\psi = 60°$ in the downstream direction. Figure 6.29(b) shows the directivity of the deep cavity in the spanwise plane, at $\phi = 90°$. The contours appear to be more circular and symmetric with respect to figure 6.28(b). An easier comparison of the near-field acoustic radiation directivity is provided by figure 6.30(a-b), where the predicted SPL from both $L/D = 0.713$ and $L/D = 2.5$ cavities is shown at the same radial distance $r = 5L$ from the cavity center $(x, y, z) = (0, 0, D)$. The $L/D = 0.713$ cavity is confirmed to be the louder flow, with two maxima of SPL = 121 dB at ($\psi = 114°, \phi = 0°$) and SPL = 118.5 dB at ($\psi = 60°, \phi = 0°$), shown in figure 6.30(b). A lower directivity maximum of SPL = 104 dB is predicted at ($\psi = 126°, \phi = 0°$) in the $L/D = 2.5$ cavity.

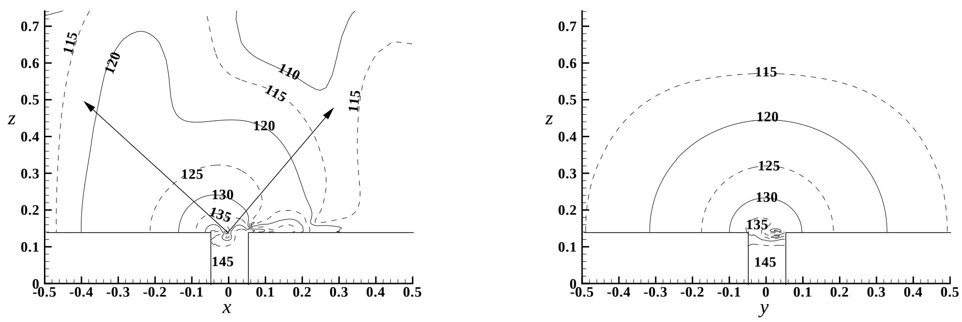

(a) $\phi = 0°$ (b) $\phi = 90°$

Figure 6.29: Contours of near-field SPL, dB re 20μPa. $L/D = 0.713$ deep cavity at $M_\infty = 0.235$ and $L/\theta = 32$.

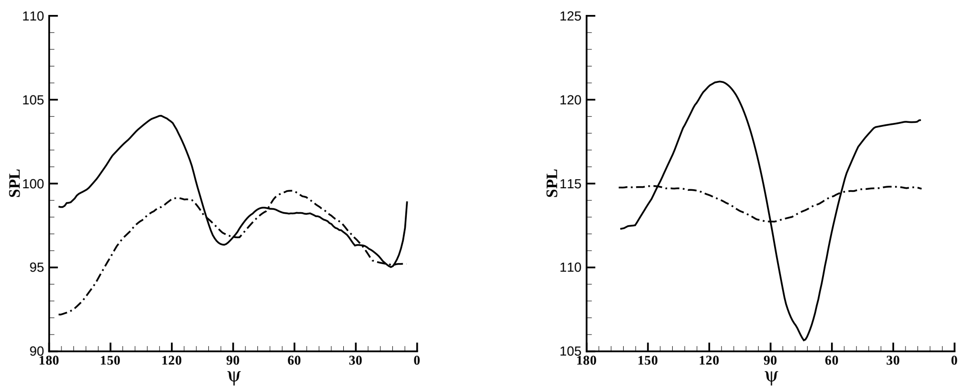

(a) $L/D = 2.5$ shallow cavity (b) $L/D = 0.713$ deep cavity

Figure 6.30: SPL at $r = constant = 5L$ above cavity opening, $\phi = 0°$ [–] and $\phi = 90°$ [– · –].

6.6 Comparison among numerical predictions

The Euler model and in the viscous flow simulation without a turbulence model predict almost the same instability mode at the same the free-stream velocity. The maximum intensity of the radiating noise depends on the approaching boundary layer thickness. To a growing shear layer corresponds a smaller amplitude of the radiating noise in the near-field in the $L/D = 0.71$ deep cavity. An asymmetric recirculation is found in the predictions from both models, while the predicted flows differ in the cavity wake region downstream the cavity trailing edge. Despite the asymmetry in the flow enclosure, the wake region in the Euler simulation is almost symmetric and the presence of a cavity results in a decrement of the flow speed by momentum loss downstream of it.

The $L/D = 2.5$ cavity shows a symmetric recirculation in the enclosure and in the cavity wake region in both simulations. A higher frequency flow unsteadiness is found in the Euler model cavity compared to $L/D = 0.71$ and it is due to the cavity staging to a higher natural mode number between $L/D = 0.71$ and $L/D = 2.5$. At $L/D = 2.5$, the viscous flow simulations predict a damped pressure fluctuation in the enclosure. The viscous model did not predict a sustained near-field acoustic pressure radiation.

Asymmetric or azimuthal instabilities can occur in a cylindrical cavity as shown mathematically by Rona (2006) and experimentally by Hering *et al.* (2006) and by Dybenko *et al.* (2006). These modes arise from the freedom of the flow to revolve inside the cavity barrel. Clockwise and anticlockwise motion is equally probable under ideal inflow conditions. Any small asymmetry in the inflow or in the cylinder barrel may trigger an azimuthal instability with a dominant clockwise or anti-clockwise wavenumber.

Fourier analysis shows the presence of an instability mode at Strouhal number 0.514 in the most refined 9.2 million cell DES in the $L/D = 0.71$ deep cavity. This is close to the dominant instability mode Strouhal number 0.532 in the Euler simulations. However, in the DES simulation with 9.2 million cell, the second mode dominates the wall pressure spectra as well as in the near-field pressure. This mode corresponds to $St = 1.02$ and is close to the second Rossiter mode predicted by the formula of Block (1976).

Using a turbulence closure model in the DES simulations gives an asymmetric recirculation in the $L/D = 2.5$ shallow cavity at $M_\infty = 0.235$ whereas the mean flow in the $L/D = 0.71$ deep cavity is essentially symmetric about the $y = 0$ cavity mid-span. This symmetry is also found in experiment, as detailed in section 6.7.

6.7 Comparison with experiment from Università degli Studi Roma Tre

This section compares the predictions from the most refined 9.2 million cell DES of the $L/D = 0.71$ deep cavity tested at a cavity diameter based Reynolds number $Re_L = 548000$ against wind tunnel tests performed at the same L/D ratio and Reynolds number. In the computations, the free-stream Mach number is 0.235 and is higher than in experiment, where this is 0.1175.

6.7.1 Approaching turbulent boundary layer

Figure 6.31 shows the streamwise evolution of the ratio of the cavity diameter to the boundary layer momentum thickness. The data refers to the $y = 0$ cavity mid-span plane, upstream of the leading edge. 200 points are extrapolated from the computational domain at $\Delta z = constant$ above the wall at the locations x/L equal to -6.9, -6, -5, -4, -3, -2, -1. $z_{\max}$ depends on the value of the boundary layer thickness δ and it is chosen equal to 3δ. The value of the momentum thickness is computed using the 200 values as the numerical integral of the discrete function $u_i/u_\infty\,(1 - u_i/u_\infty)$ with respect to z over the range $0 \le z_i \le z_{\max}$. z_i is the ith interpolated position normal to the wall. In the range $-6 < x/L < -1$, θ grows faster than in a $1/7^{th}$ power law turbulent boundary layer under zero pressure gradient, in which $\theta/x = 0.036 Re_x^{-0.2}$ (Calvert & Farrar, 1999). As the boundary layer thickness at the computational domain inflow was prescribed assuming a $1/7^{th}$ power law growth rate, θ approaching the cavity leading edge is higher than agreed for joint experimental and numerical work between the University of Leicester and the Università degli Studi Roma Tre. This gives a lower L/θ approaching the cavity leading edge with respect to the target value $L/\theta = 62$. The experiment was such that $L/\theta = 72$ at $x/L = -1$, which gives a value of the momentum thickness slightly lower as compared to the target value.

The cavity instability modes are influenced by the value of the approaching turbulent boundary layer momentum thickness, as shown by Colonius & Lele (2004) in rectangular cavity flows. In the cylindrical cavity, the instability mode is driven mainly by the interaction between acoustic resonance (organ pipe type mode) and the cavity 'Rossiter' like modes. At the selected free stream speeds in the simulation, a peak

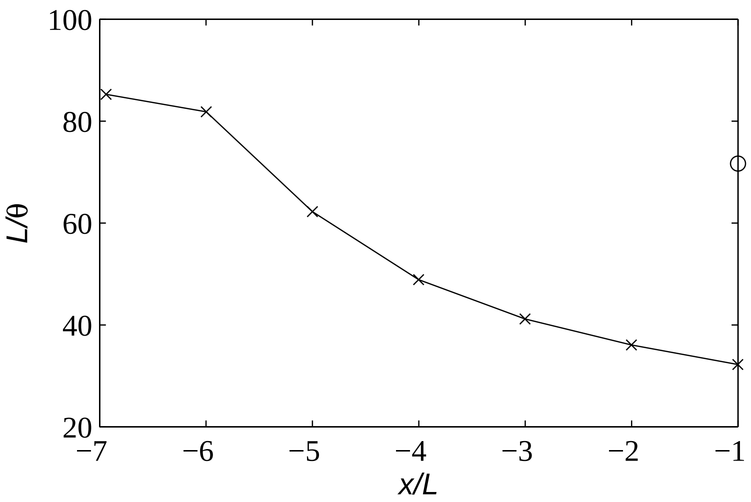

Figure 6.31: Boundary layer growth in the computational domain and comparison with experiment approaching the cavity leading edge. $y/L = 6.9$ plane at $u_\infty = 80$ m/s.

in the wall pressure spectrum corresponding to this frequency is found, as shown in section 6.7.3.

Figure 6.32 shows the normalized time-averaged velocity profiles predicted by the 9.2 million cell DES model along the cavity mid-span, on the $y = 0$ plane. The profiles detail the boundary layer upstream of the cavity. Symbols $\times, \cdot, +$ and $*$ denote time-averaged streamwise velocity profiles at x/L equal -7, -6, -5, and -4, respectively. The contours line denotes the power law curve $u/u_\infty = (z/\delta)^{-1/7}$, which is given as a reference, and the circles denote the wind tunnel measurements. In the numerical predictions, the boundary layer displays a streamwise growing velocity defect on approach to the enclosure that is higher than the target value, represented by the $1/7^{th}$ power law. In experiment, the velocity defect is lower than the target value.

The comparison given in section 6.7.2 is limited by this difference in the approaching boundary layer between experiment and computation.

6.7.2 Mean flow

Figures 6.33(a), 6.33(c), 6.34(a) and 6.34(c) are hot-wire streamwise velocity measurements taken above and inside the $L/D = 0.71$ cavity at $Re_L = 548000$. Figures 6.33(b), 6.33(d) 6.34(b) and 6.34(d) are the time-averaged stream-wise velocity profiles from

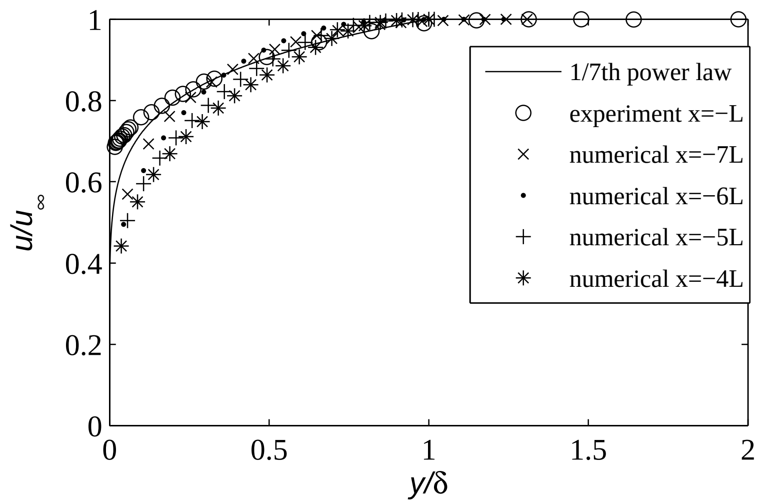

Figure 6.32: Boundary layer mean velocity profiles at different streamwise locations in the $y = 0$ plane. $L/D = 0.71$ deep cavity at $Re_L = 548000$.

the 9.2 million cell DES. The numerical predictions are obtained by averaging over 6000 time-dependent snapshots of the computational domain. The mean flow field is obtained in the time-marching DES computation by adding a running average routine to the flow solver. The predicted mean flow is then visualized using TECPLOT 360.

The measurements cover a different u/u_∞ range in experiment and in the computations. The range of the ordinate axis has been chosen differently in experiment and computation to best resolve the respective trends within. At the same non-dimensional height z/L, listed in the legend of each figure, the computation predicts a lower u/u_∞ than the measurements. For instance, at $z/L = 0.024$, the predictions of figure 6.33(b) at $x/L = -0.25$ (open red circles) give a span-averaged mean velocity profile of approximately $0.53u_\infty$, whereas the measured values at the same x/L, z/L in figure 6.33(a) (open red circles) show a span-averaged mean velocity profile of approximately $0.81u_\infty$. This difference is present at the upstream most traverse and is therefore not just the result of different shear layer growth rates above the enclosure, but it is due to the different boundary layer momentum thickness approaching the model cavity than in experiment, as documented in section 6.7.1.

The eddy viscosity in the Detached Eddy Simulation plays an important role in determining the streamwise growth of the inflow boundary layer. However, in the DES

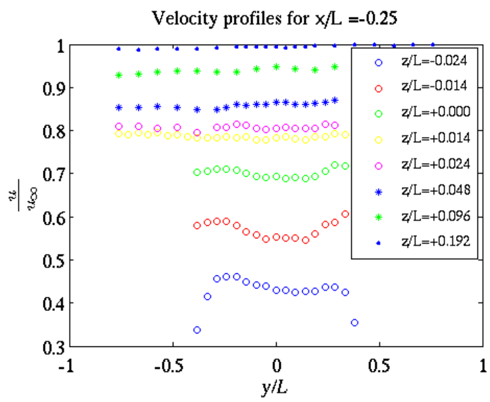

(a) Experimental values. Plane $x/L = -0.25$

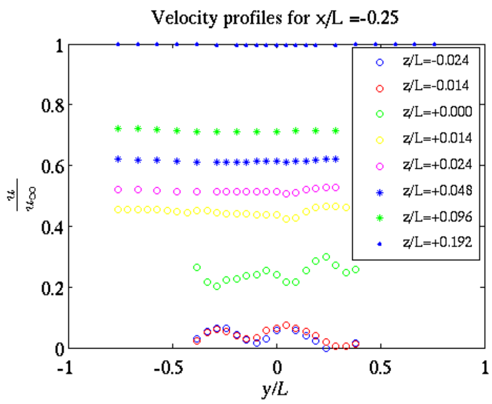

(b) Numerical values. Plane $x/L = -0.25$

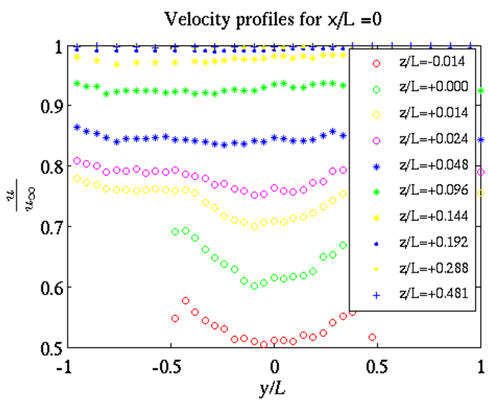

(c) Experimental values. Plane $x/L = 0$

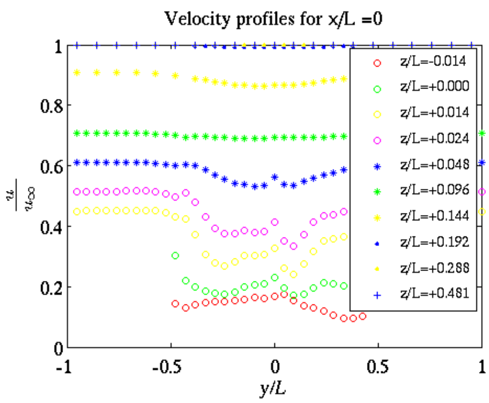

(d) Numerical values. Plane $x/L = 0$

Figure 6.33: Spanwise profiles of non-dimensional time-averaged streamwise velocity across the cavity opening. $L/D = 0.71$ deep cavity at $Re_L = 0.546 \times 10^6$, experimental $M_\infty = 0.1175$ and numerical $M_\infty = 0.235$. Different y-axis ranges are used to account for the shear layer streamwise growth.

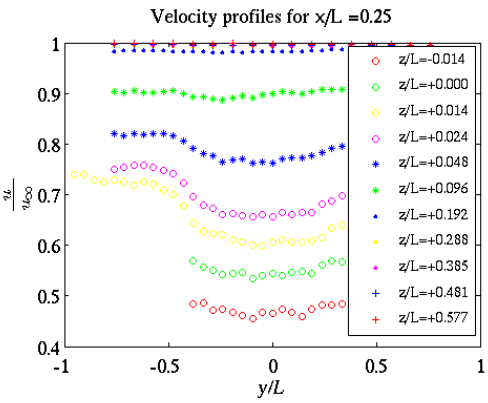

(a) Experimental values. Plane $x/L = 0.25$

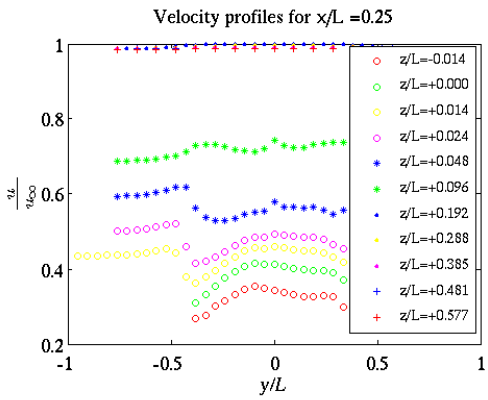

(b) Numerical values. Plane $x/L = 0.25$

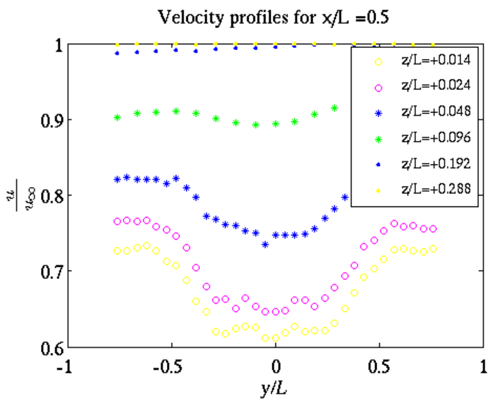

(c) Experimental values. Plane $x/L = 0.5$

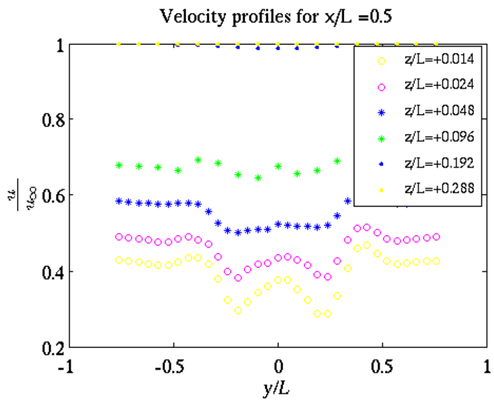

(d) Numerical values. Plane $x/L = 0.5$

Figure 6.34: Spanwise profiles of non-dimensional time-averaged streamwise velocity across the cavity opening. $L/D = 0.71$ deep cavity at $Re_L = 0.546 \times 10^6$, experimental $M_\infty = 0.1175$ and numerical $M_\infty = 0.235$. Different y-axis ranges are used to account for the shear layer streamwise growth.

model, the value of the eddy viscosity close to the wall is less controllable than in standard RANS computations, as it is driven by the hybridization of the RANS and LES models in the turbulence closure. The sensitivity of the numerical predictions to changes in the RANS to LES blending function was not tested. Adjusting the turbulence model to reproduce the inflow boundary layer growth rate of the experiment was not attempted, as it departs from the main aim of this work, which focuses on reproducing the cavity interior flow. The author used published values of the RANS/LES turbulence closure model, relying on the underlying calibration work of Yoshizawa (1986) and of Menter (1992).

Above the cavity opening, the shear layer from the detached eddy simulation computation seems to grow more slowly as compared to the measured flow. Specifically, whereas the difference between the predicted spanwise averaged mean velocity profile at $x/L = -0.25$ and $x/L = 0.5$ at $z/L = 0.024$ is about $0.1u_\infty$, as shown by the red open circle symbols in figures 6.33(b) and 6.34(d), the measured spanwise averaged mean velocity at the same z/L reduces by $0.15u_\infty$ over the same streamwise distance above the enclosure, as shown by figures 6.33(a) and 6.34(c). This difference in shear layer growth rate is appreciable but is not as significant as to determine a large change in the mean streamwise convection velocity. These two aspects are responsible for the cavity instability and the production of noise.

The three dimensionality of the flow above and inside the enclosure is confirmed by the spanwise non-uniform velocity profile. This result in different shear layer growth rates along the span. The streamwise distance between the shear layer separation point and its impingement on the downstream cavity edge is maximum at the cavity mid-span, where the flow spans over $1L$. The shear layer at the cavity mid-span has therefore more distance to grow over the cavity open end before it reaches the downstream wall than the flow that separates at either side of the $y = 0$ plane. This results in a greater momentum transfer from the free-stream to the slower moving flow inside the cavity. Therefore, at the same wall-normal distance $z/L > 0$, a lower streamwise velocity is expected along the cavity mid-span compared to the cavity sides. This is confirmed experimentally and numerically in figures 6.33 and 6.34. The spanwise profiles of time-averaged velocity from experiment, figures 6.33(a), 6.33(c), 6.34(a) and 6.34(c), show a velocity minimum in the $y = 0$ plane, just like in the predictions of figures 6.33(b), 6.34(b), 6.33(d) and 6.34(d). This suggests an increasing flow entrainment at this plane.

Figures 6.35(a)-(f) show spanwise profiles of the non-dimensional time-averaged streamwise velocity at different heights above the downstream cavity bulkhead. Figures 6.35(a), 6.35(c), and 6.35(e) are measurements from the Università degli Studi Roma Tre and figures 6.35(b), 6.35(d), and 6.35(f) are the corresponding DES numerical predictions using a 9.2 million cell mesh. The two primary and two secondary vortices described in section 6.5 give two symmetric local maxima at $y/L \sim \pm 0.45$ in the planes $x/L = 0.89$ and $x/L = 1.55$ in the numerical investigation and in the plane $x/L = 1.55$ in experiment. In the numerical study, the numerical viscosity is probably inducing an early flow separation at the cavity trailing edge. This results in the effect of the secondary vortices on the spanwise profile of time-averaged streamwise velocity being more pronounced. As a result, the velocity maxima can be observed more clearly in the numerical simulations further upstream than in the measurements.

Further downstream, at $x/L = 2.55$, the secondary vortices are dissipated and only the two counter-rotating primary vortices are detected in both the numerical predictions of figure 6.35(f) and in the experimental profiles of figure 6.35(e). Local maxima in each experimental profile at different z/L are found at $y/L \sim \pm 0.4$ whereas they are found at $y/L \sim \pm 0.35$ in the numerical predictions. The elevation of these maxima above the streamwise velocity of the relatively unperturbed boundary layer to the sides of the cavity, at $|y/L| > 1$, at each z/L is $0.05 \leq \bar{u}/u_\infty \leq 0.1$ in the experimental profiles and $0.1 \leq \bar{u}/u_\infty \leq 0.2$ in the numerical predictions. The differences in the boundary layers approaching the enclosure between experiment and computation discussed in section 6.7.1 are likely to be responsible for this difference. Specifically, the fully turbulent boundary layer approaching the enclosure in experiment contains a wide spectrum of structures. As these structures interact with the primary vortices, they introduce an additional degree of unsteadiness on top of the one resulting from the tonal cavity instability. The instantaneous position of the counter-rotating primary vortex cores are therefore like to precess in the $x/L = 2.55$ plane. By time averaging, the motion of the vortex cores results in broader local maxima with a lower peak in the measured profiles of figure 6.35(e) than in figure 6.35(f).

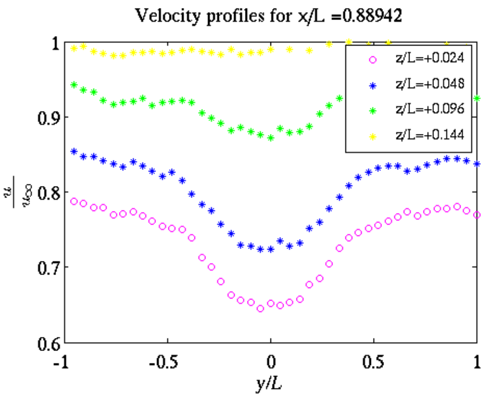

(a) Experimental values. Plane $x/L = 0.89$

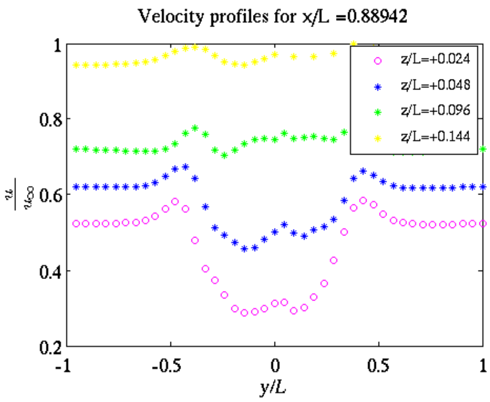

(b) Numerical values. Plane $x/L = 0.89$

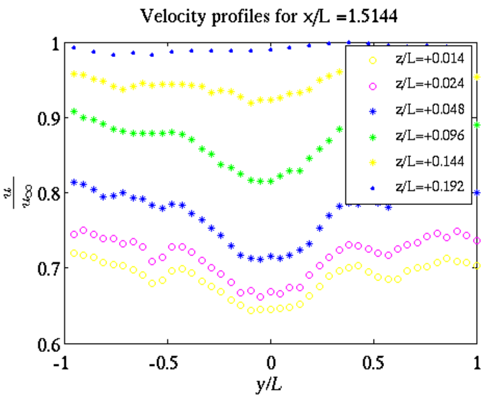

(c) Experimental values. Plane $x/L = 1.51$

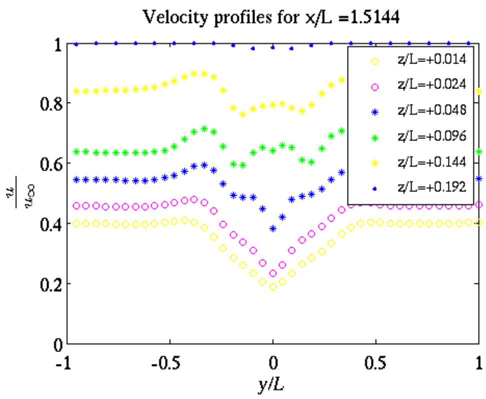

(d) Numerical values. Plane $x/L = 1.51$

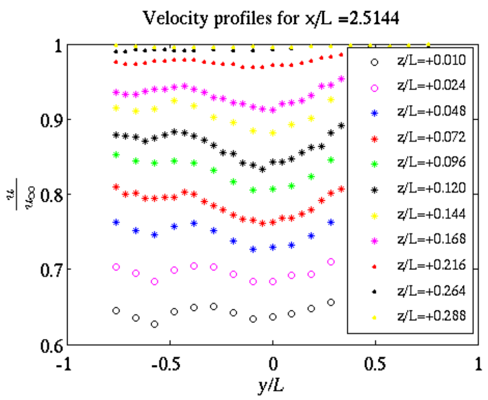

(e) Experimental values. Plane $x/L = 2.51$

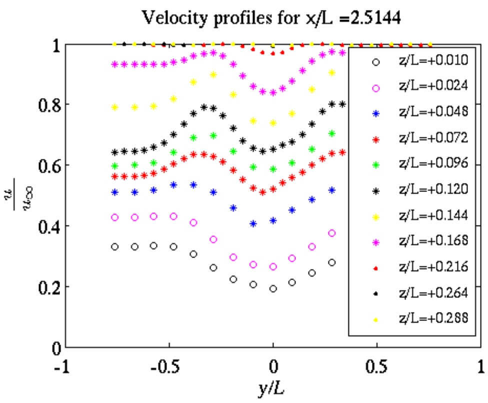

(f) Numerical values. Plane $x/L = 2.51$

Figure 6.35: Spanwise profiles of non-dimensional streamwise velocity over the downstream bulkhead. $L/D = 0.71$ deep cavity at $Re_L \approx 54.8 \times 10^3$. experimental $M_\infty = 0.1175$ and numerical $M_\infty = 0.235$. Different y-axis ranges are used to account for the shear layer streamwise growth.

6.7.3 Unsteady flow

Figure 6.36 shows the non-dimensional power spectral density (PSD) that corresponds to the wall pressure fluctuation at $(x/L, y/L, z/L) = (0.5, 0, -0.35)$ in the $L/D = 0.71$ deep cavity.

The reference free-stream velocity u_∞ is 40 m/s and 80 m/s in experiment and in the numerical model, respectively. To compare experiment and computation, frequency in the PSD is normalized by the cavity diameter L and free-stream reference velocity u_∞, which gives the Strouhal number $St = fL/u_\infty$. Similarly, the PSDs are normalized by the fourth power of the free stream velocity and by the square of the free-stream density.

The experimental data are acquired with a sampling frequency of 40 kHz over a period $tu_\infty/L = 952$. The data is then divided into shorter intervals of $tu_\infty/L = 47.62$ that are discrete Fourier transformed, giving a $\Delta St_{exp} = 0.021$. The experimental power spectra are then ensemble averaged to reduce noise. The numerical data are sampled over a period $tu_\infty/L = 25.56$ that corresponds to $\Delta St_{num} = 0.039$.

The dashed line in figure 6.36(a-b) shows a power $-7/3$ slope. This corresponds to the energy cascade of pressure fluctuations in the inertial range of three-dimensional isotropic turbulence (Kolmogorov, 1991). The measured and predicted PSD seem to follow this slope at $St > 1.5$ within limits. Specifically, the decay of pressure fluctuation amplitude with frequency reported in figure 6.36(a) stops at $St > 8$, leading to a flat spectrum over the range $8 < St < 24$ and finally to a higher energy decay. This trend is due to two different aspect in the experimental acquisition. The flat spectrum is related to the Kelvin-Helmholtz resonance at the frequency of the pin-holes where the microphones are mounted. The energy drop in the PSD at $St > 24$ is due to the anti-aliasing analogue filter that was used in-line with the microphones. The experimental set-up is detailed in Verdugo *et al.* (2009).

The numerical predictions at $St > 8$ show a sustained decay of pressure fluctuation amplitude at increasing Strouhal numbers. This decay displays however a modulation, which is likely to be a spurious numerical effect from the error in modelling high-frequency and high-wavenumber components with the flow solver, which is at best third order space accurate.

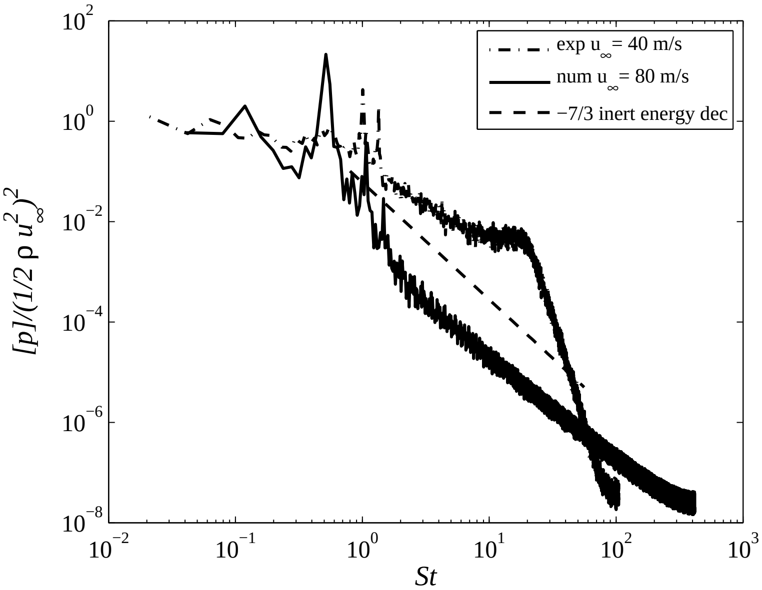

(a) Power Spectral Density

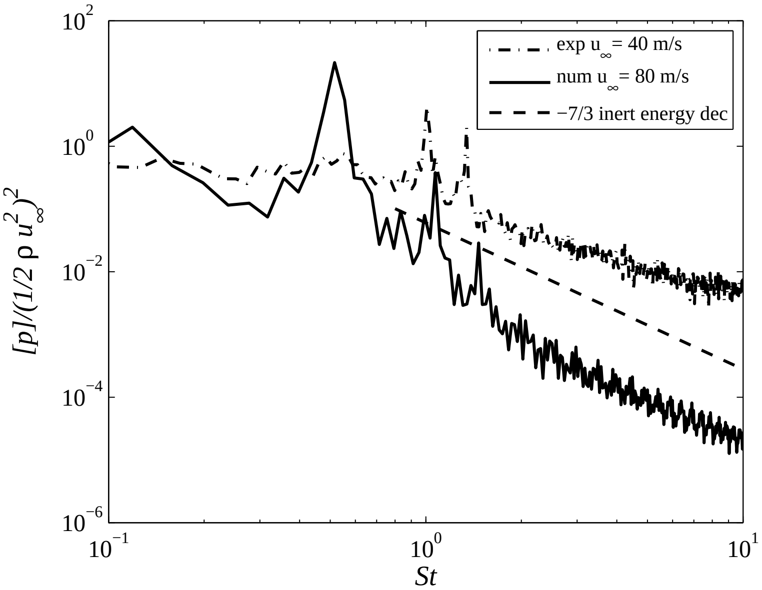

(b) Detail of the PSD

Figure 6.36: Non-dimensional PSD of wall pressure from the $L/D = 0.71$ deep cavity at a free-stream velocity of 40 m/s (experiment) and 80 m/s (Detached Eddy Simulations).

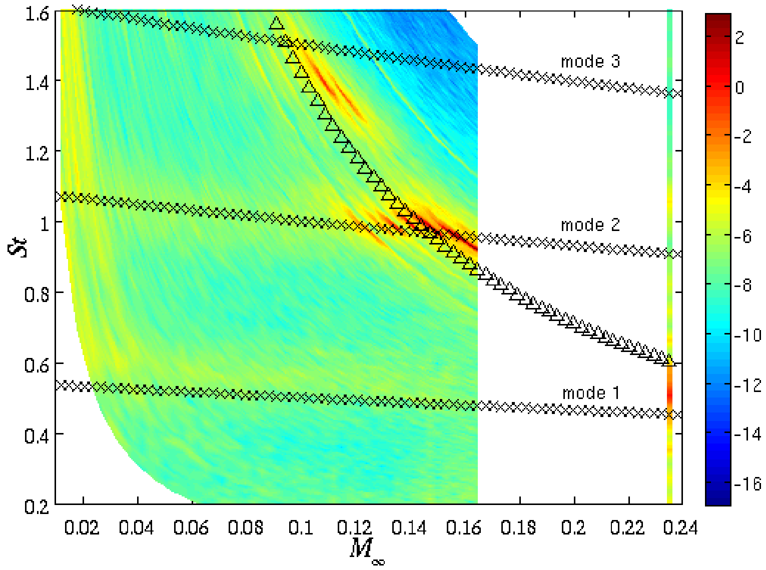

Figure 6.37: Non-dimensional PSD of cavity wall pressure at varying free-stream Mach numbers. Instability modes $n = 1, 2, 3$ from Block (1976) ($\times$), acoustic resonant (depth) mode ($\triangle$). $L/D = 0.71$ deep cavity.

The predicted PSD in figure 6.36(b) displays a higher frequency peak at $St_{1,num} = 0.51$, which is close to the first mode $n = 1$ identified by the formula of Block (1976). A less intense peak is shown at $St_{2,num} = 1.05$, which close to the second mode $n = 2$ from Block (1976). In the measured PSD, two peaks are found at $St_{1,exp} = 1.01$ and at $St_{2,exp} = 1.34$, respectively. These correspond to the second mode from Block (1976) and to the first acoustic resonant mode (depth mode). A less intense peak at $St_{3,exp} = 0.56$ is close to the first mode from Block (1976).
For a given cylindrical cavity geometry of constant aspect ratio L/D, the acoustic resonant mode is proportional to $1/M_\infty$ as described in section 2.4. Figure 6.37 shows non-dimensional PSD at varying free-stream Mach number. The data over the range $0.015 < M_\infty < 0.165$ are from experiment and the data at $M_\infty = 0.235$ are from the numerical model. The non-dimensional coordinates of the measurement location, the anti-aliasing filter, the sampling rate and the spectral averaging are the same as in figure 6.36. The PSD prediction from the numerical model are that of figure 6.36. The PSD amplitude is shown by iso-colour levels in figure 6.37, using the same logarithmic scale of figure 6.36.

Figure 6.37 shows how the depth mode and the $n = 1, 2, 3$ cavity resonant mode constructively interfere when their Strouhal numbers are close to each other. Consider the discrete wall pressure spectra at $M_\infty = 0.115$, $M_\infty = 0.14$ and $M_\infty = 0.235$. At these three Mach numbers, red regions of high pressure fluctuation amplitude appear close to the intercept of the predicted acoustic mode, shown by the line with triangles ($\triangle$), with a cavity resonant mode, shown by a line of crosses ($\times$). This mode coincidence generates reinforced wall pressure fluctuations. Coincidence occurs between the first acoustic depth mode and the third cavity resonant mode from Block (1976) at $M_\infty = 0.115$, between the first acoustic mode and the second cavity resonant mode at $M_\infty = 0.14$, and between the first acoustic mode and the first cavity resonant mode at $M_\infty = 0.235$.

Figure 6.37 shows the value of complementary experiment and numerical simulations in unsteady aerodynamics. In experiment, it is relatively straight forward to vary the wind-tunnel velocity over the range $0 \leq u_\infty \leq 40$ m/s and acquire several spectra, to well-resolve the variation of the mode amplitudes with the inflow Mach number. However, the wind tunnel measurements could not be performed at Mach numbers above 0.16, due to the rising tunnel noise floor in the measurements. As the computational scheme used in this work is based on an approximate Riemann solver, the scheme is not limited to low Mach numbers and in fact works better and faster at higher Mach numbers. However, varying the Mach number in the simulations requires one complete new run per Mach number, which is computationally expensive. The numerical and experimental methods therefore complement each other well, the measurements giving good resolution at low Mach numbers and the numerical method allowing to explore the coincidence between the first acoustic mode and the first cavity resonance mode, lying above the Mach number operational limit of the wind tunnel. By merging the results from numerical and experimental techniques, figure 6.37 gives a more complete picture of the effect of mode coincidence in a $L/D = 0.71$ deep cavity over the range $0.1175 \leq M_\infty \leq 0.235$. By combining both results, a better description of the flow physics is obtained, specifically, the measurements enable to appreciate the difference in mode amplitude at coincidence and away from this conditions, whereas the numerical predictions resolved the coincidence between two modes that occurs above the operating limits of the wind tunnel.

In previous numerical and experimental investigations on rectangular cavities (Colonius & Lele, 2004; Colonius *et al.*, 1999; Rossiter, 1964; Rowley *et al.*, 2002; Tam & Block, 1978), the cavity mode selection is triggered by the approaching boundary layer momentum thickness. In this study, the dominant instability mode at $M_\infty = 0.235$ is triggered by the coincidence between the $n = 1$ first instability mode and the cavity acoustic resonant mode.
The modes predicted by the formula of Block (1976) are satisfactory in terms of their dependency on the Mach number. The cavity modes switching is closely related to the coincidence with a cavity resonant (depth) mode by Rayleigh (1894).

6.8 Conclusion

This chapter analysed the different aerodynamic instabilities found in the cylindrical cavity when varying the diameter to depth ration (L/D) and the free-stream velocity. The cavity flow instability was found to be weakly influenced by a small change of 5% increase in the boundary layer thickness. The instability modes are closely linked to the geometrical parameters and to the flow parameters, in particular a symmetrical recirculation was found at $L/D = 0.71$ both numerically and experimentally and an asymmetric recirculation was found at $L/D = 2.5$ when the turbulent model was used. A different behaviour was found when the flow was modelled as inviscid, in particular the numerical simulation predicted an asymmetric recirculation in the $L/D = 0.71$ cavity. This is described in section 6.6. A non-dimensional comparison of the $L/D = 0.71$ was done by means of time-averaged result and time-dependent results. The approaching turbulent boundary layer measured in the experiment had a higher velocity with respect to the canonical $1/7^{th}$ power law close to the wall, whereas the one measured in the computation had a lower velocity close to the wall. The mean flow was captured qualitatively correctly but not quantitatively. The study of the Power Spectral Density highlighted the coincidence of the acoustic resonance mode and the "Rossiter" modes as well as the mode selection mechanism.

Chapter 7

Conclusion

7.1 Introduction

A time-dependent numerical investigation was performed on the aerodynamic unsteadiness and near-field radiating pressure from a cylindrical cavity at two aspect ratios $L/D = 0.71$ and $L/D = 2.5$ at the Reynolds number $Re_L = 548000$ and $Re_L = 698000$ and two Mach numbers of 0.235 and 0.3. The numerical data from the mesh converged test case of the $L/D = 0.71$ cavity at $M = 0.235$ and $Re_L = 548000$ were compared with those from Università degli Studi Roma Tre wind tunnel experiment. This chapter highlights the achievement of the numerical model.

7.2 Conclusion

Time-resolved numerical models of a cylindrical cavity flow predicted symmetric and asymmetric cavity instabilities mainly related to the diameter to depth ratio of the cavity. Three different numerical approaches were used to model the flow. These were an inviscid flow prediction (Grottadaurea & Rona, 2007a), a viscous flow prediction, in which the dissipation is associated only to the viscosity of the flow and to the numerical dissipation given by the grid stretching (Grottadaurea & Rona, 2007b), and a turbulent flow prediction, in which the energy dissipation at the small scales of turbulence is modelled using Detached Eddy Simulation (Grottadaurea & Rona, 2008b).

The Detached Eddy Simulation gave fundamentally different predictions than the other two approaches.
An azimuthal instability and a recirculation with its axis at 45° with respect to the streamwise direction was identified in flow averaged numerical result of the Euler model and in the viscous flow model of the $L/D = 0.71$ deep cylindrical cavity. Mass ejection and injection were predicted only on one side of the cavity. This peculiar instability was documented in the experiments of Gaudet & Winter (1973) and of Dybenko *et al.* (2006) in a $L/D > 2$ shallow cylindrical cavity. This asymmetric pattern was also found in a coarse mesh DES cavity simulation of 1.6 million cells. This prediction was at odds with the available literature and the experiments by Verdugo *et al.* (2009) on the $L/D = 0.71$ deep cylindrical cavity, where a symmetric pattern is reported. Only a 2.8 million cells finer mesh and a subsequent mesh convergence test using a 9.2 million cells DES model were able to predict the symmetric flow observed in experiment. The last computation used a optimized recursive MPI parallelization technique developed by the author.
The importance of testing for mesh independence in the simulations is demonstrated by the mode switching between the different levels of mesh refinement in the L/D deep cylindrical cavity DES. In spite of some difference in the approaching boundary layer momentum thickness, the refined test cases were able to show the symmetric flow regime observed in experiment.
The simulation helped to interpret the measured velocity distributions at various streamwise planes. Local velocity maxima are due to counter-rotating convective eddies generated at the cavity downstream edge. To visualize this vortex, the time-mean spanwise and flow-normal velocity components were used to trace in-plane streamlines. Despite the complexity associated with modelling the cylindrical cavity flow and the uncertainty associated with using just standard DES turbulence closure parameters, the three-dimensional DES simulations offered an improved insight of the flow by means of time-dependent and time-averaged predictions that are well-resolved in space and time.
The comparison between Euler and viscous flow simulations showed the significant effect the inflow boundary layer thickness has on the near-field Sound Pressure Level. The Euler model develops a thin numerical shear layer across the cavity opening, equivalent to having a very thin inflow boundary layer. A thinner boundary layer gives

a louder near-field pressure fluctuation in a cavity flow, as found experimentally by Dang-Guo *et al.* (2009) in a rectangular geometry at different δ/L.

The time dependent predictions of the radiating pressure field in the shallow and deep cavity configurations indicate a significant noise radiation from these flows. The acoustic near-field is not symmetric with respect to the cavity mid-span in the $L/D = 2.5$ shallow cavity. This asymmetry is most likely linked to the azimuthal instability modes that develop in the enclosure. The mode selection in the 'hydrodynamic' flow region that spans the cavity opening drives the production of sound along preferential directions in the acoustic near-field. The persistence of such asymmetric radiation in the acoustic far-field is likely to be significant for the noise performance of cylindrical aircraft fuel vents at landing.

The DES simulation and the experiment show that the fundamental instability mechanism described by Rossiter is found in a subsonic turbulent cylindrical cavity flow and that the mode frequency can be obtained by using a correction to the characteristic length by Czech *et al.* (2006) in the modified Rossiter formula of Block (1976).

The cylindrical cavity is characterized also by acoustic resonant modes associated with the geometry, as described in Rayleigh (1894). The interaction between the hydrodynamic convective instabilities, the Rossiter modes, and acoustic instabilities is found to be significant for the mode selection in the cylindrical cavity flow, as detailed in section 6.7.3.

The Power Spectral Density of the wall pressure fluctuation at varying Mach number from Verdugo *et al.* (2009) was used to interpret the physics behind mode switching in the cylindrical cavity flow. Scaled numerical predictions were used to extend the Mach number range to $M_\infty = 0.235$ and show how the higher intensity mode correspond to the coincidence between the first acoustic resonant modes and the first "Rossiter" mode. This interaction is also found in experiment at $M_\infty = 0.123$ and $M_\infty = 0.145$.

Marsden *et al.* (2008) modelled a cylindrical cavity of $L/D = 1$ at $M_\infty = 0.265$ using cylindrical coordinates in the enclosure and Cartesian coordinate elsewhere, and used a high-order Lagrangian interpolation at the interface. The advantage of such modelling strategy is not to include a curvilinear coordinate system in the computation and to be able to use a high-order flow solver coupled with an analytical (exact) evaluation of the Jacobians. Although different approaches can be sought to model a cylindrical cavity flow to overcome the limitation associated with a low-order finite-volume flow solver, the latter is more suitable to study flow of industrial interest. The curvilinear multi-block parallel DES code developed in this study aims to be a ready-to-use tool to study such flows.

The MPI parallelization strategy, developed at CINECA by Grottadaurea & Rona (2008a), was essential for running the mesh refined test-cases that required a large number of cells. A 4 GB RAM processor limited the simulations to a maximum of 1.4 million cells test case. The recursive domain decomposition overcome this limitation distributing only a smaller portion of the full computational domain across distributed memory clusters. It granted the access to the most powerful distributed memory facilities in Europe and represented a strong attractor for the industrial use of this code in applications that require a high computational performance.

The algorithm includes a novel aspect by parallelization of the input with respect of the flow variables and geometry parameters. Distribution of Input/Output of existing parallel codes represent the state of the art of MPI parallelization, a preliminary step to achieve this is presented in this work.

The comparison of parallelization strategies in section 4.4 demonstrated the advantage of using this algorithm as compared to a single domain decomposition, in which a large number of processors are used in the simulation. This algorithm represents a suitable candidate to further increase in parallelization efficiency, reducing the processors communication.

Chapter 8

Future work

Given the potential impact of asymmetric cavity instability modes on airframe noise and the difficulties associated with its modelling, further research is required to determine the drivers behind mode staging, together with a better assessment of the effects such modes have on the radiated noise. A number of simulations at different aspect ratios and varying the free-stream velocity is required to extend the formula of Block (1976) for cylindrical cavity flows that feature such modes.

The present numerical model of the near-field cylindrical cavity flow can be used to seek far-field noise predictions and to reconstruct the contribution of fuel vent noise to the aircraft landing Effective Perceived Noise Level (ICAO, 2002). This requires locating the monitoring points of a ground observer outside the airframe cavity following the Chapter 3 ICAO (2002) guidelines for landing noise. Considering the distance of the ground observer prescribed by ICAO (2004), stretching a single computational domain to include the ground observer is not computationally affordable, therefore the acoustic predictions will be obtained via a hybrid approach, which divides the computational domain into a source region (acoustic near-field) and a propagation region (acoustic far-field), developing a Ffowcs Williams & Hawkings (1969) acoustic analogy in the simplified formulation of Di Francescantonio (1997) and Brentner & Farassat (1998).

As discussed in section 6.7.3 limitations are found in modelling the energy associated with high frequency pressure fluctuations. Although the energy decay is captured in the numerical simulation, a modulation is found in the power spectral density. This modulation is probably associated with the use of a low-order finite-volume flow solver. This limitation does not affect the result herein reported but limits the use of the flow solver only to application dominated by periodic flow phenomena of a relatively small spectral breath. This aspect is considered a future point for improvement for this numerical method.

In parallel to the author's work, Spisso & Rona (2007) have been developing a high-order finite-difference flow solver to upgrade the existing flow solver. The high-order method allows to reduce dispersion and dissipation errors of the low-order solver using the same computational mesh. Despite the complexity associated with boundary closure, such as wall boundary conditions or radiating boundary conditions, this method gives a higher power spectral density cut-off frequency. This may help to remove the spurious numerical modulations predicted at the high frequency end of the power spectral density of aerodynamic pressure.

To retain the computational advantage of the high-order interior scheme, high-order no-slip wall boundary conditions are required, that advance on the inviscid wall formulation of Spisso *et al.* (2009). The introduction of a curvilinear coordinate system to the selected high-order finite difference scheme is also required to model a cylindrical cavity. This can be achieved following the work of Visbal & Gaitonde (1999) and Visbal & Rizzetta (2002).

This work highlighted the importance of modelling dissipation in cylindrical cavity flows. The Detached Eddy Simulation turbulence closure can be improved by the dynamic sub-grid scale model of Germano *et al.* (1991) or Lilly (1992). Despite the larger computational cost of this model, as stated by Monti & Rona (2009), this approach will remove some of the model constant calibration issues of the current implementation of Detached Eddy Simulations.

A different approach is not to use a RANS wall-function and model the flow only using LES. This was not attempted due to the difficulties associated with modelling flow separation only with LES, where a constant value from Yoshizawa (1986) is used for the Smagorinsky (1963)-Lilly (1966) constant. The improved dynamic sub-grid scale model overcomes also this limitation.

Appendix A

Laminar boundary layer inflow for CFD

The inflow to the computational domain is imposed by solving the compressible non-dimensional form of the Blasius equation for a laminar boundary layer. The following equations describe the flow field (White, 1991):

$$f'''(\eta) + f(\eta) f''(\eta) = 0 \tag{A.1}$$

$$\frac{T_{aw}}{T(\eta)} = 1 + \frac{\gamma - 1}{2} r M(\eta)^2 \tag{A.2}$$

Equation (A.1) is the non-dimensional Blasius equation for a laminar boundary layer, where $\eta = \tilde{z}\sqrt{u_\infty / (2\nu\tilde{x})}$ and $u = u_\infty f'(\eta)$. Equation (A.2) gives the adiabatic wall temperature, when $M(\eta) \rightarrow M_\infty$ and $T(\eta) \rightarrow T_\infty$. In (A.2), r is the recovery factor and γ the specific heats ratio. For a Prandtl number (Pr) in the range $0.1 < Pr < 3$, the recovery factor $r = \sqrt{Pr}$.
From equations (A.1) and (A.2) and assuming the static pressure p is constant across the boundary layer, the conservative variables distribution is known as a continuous function of the flow-normal direction ($\tilde{z}$). The discretized conservative variables vector

distribution $\mathbf{U}_i$ is the average of the local value of $\mathbf{U}$ over the cell:

$$\mathbf{U}_i = \frac{1}{\Delta z} \int_{z_i}^{z_{i+1}} \mathbf{U}(\tilde{z})\, d\tilde{z} \tag{A.3}$$

In the equation (A.3), it is assumed that the local variation of $\mathbf{U}$ in the flow-normal direction ($\tilde{z}$) is larger compared to that in the streamwise direction ($\tilde{x}$) and in the spanwise direction ($\tilde{y}$).

Appendix B

Turbulent boundary layer inflow for CFD

B.1 Mean velocity profile

The mean streamwise velocity u of a fully developed turbulent boundary layer is found as a function of the distance from the wall in the flow-normal direction z, the friction velocity u_τ and the boundary layer thickness δ.
In particular, let $z^+ = yu_\tau/\nu$ be the inner scaling non-dimensional wall-normal distance, where ν is the kinematic viscosity of the flow. To describe the mean velocity profile in a turbulent boundary layer, similarity solutions are sought in the inner and the outer regions. In the inner region, the following relation describes the mean velocity profile

$$\frac{u}{u_\tau} = f\left(z^+\right) \tag{B.1}$$

In outer region, the velocity profile is described by the velocity defect law

$$\frac{u_\infty - u}{u_\tau} = f\left(\eta\right) \tag{B.2}$$

where $\eta = y/\delta$ is the outer scaling non-dimensional wall-normal distance and u_∞ is the free-stream velocity.

Based on the existence of an overlap region between the inner and the outer regions, Coles (1956) proposed the following additive law of the wall and law of the wake in non-dimensional form:

$$\begin{aligned} u^+ &= \frac{1}{\kappa} \ln z^+ + B + \frac{\Pi}{\kappa} f(\eta) \\ f(\eta) &= 1 - \cos(\pi\eta) \end{aligned} \tag{B.3}$$

where $u^+ = u/u_\tau$ is the normalized streamwise velocity, Π is the wake parameter, κ the von Kármán constant, and B the logarithmic law constant.

Coles (1956) determined the wake parameter as

$$\Pi = \kappa/2 \left(u_e^+ - \kappa^{-1} \ln Re_\tau - B\right) \tag{B.4}$$

where $Re_\tau = \delta u_\tau/\nu_l$ is the boundary layer Reynolds number and $u_e^+ = u_e/u_\tau$ is the normalized free-stream velocity.

Let

$$f(\eta) = A_1\eta^2 + A_2\eta^3 \tag{B.5}$$

be a cubic polynomial approximation to $f(\eta)$ in equation (B.3). Substituting the boundary conditions

$$u|_{y=\delta} = u_e \tag{B.6}$$

and

$$\left.\frac{\partial u}{\partial y}\right|_{y=\delta} = 0 \tag{B.7}$$

in equation (B.3), with $f(\eta)$ from equation (B.5), gives $A_1 = 6[1 + 1/(6\Pi)]$ and $A_2 = -4[1 + 1/(4\Pi)]$, with Π defined by equation (B.4). The law of the wake of equation (B.3) then becomes

$$u^+ = \underbrace{\frac{1}{\kappa} \ln z^+ + B}_{\text{Log-law of the wall}} + \underbrace{\frac{1}{k}\eta^2(1-\eta) + 2\frac{\Pi}{\kappa}\eta^2(3-2\eta)}_{\text{Wake component}} \tag{B.8}$$

Equation (B.8) is validated over a relatively wide range of momentum thickness based Reynolds number $Re_\theta = u_e\theta/\nu_l$ (Rona *et al.*, 2009) for $z^+ > 30$. The author takes $\kappa = 0.41$ and $B = 5.0$ to evaluate equation (B.8), as proposed by Coles (1956).
At $5.4 < z^+ < 30$, the following relation is used in the buffer layer (White, 1991):

$$z^+ = u^+ + \exp -\kappa B\left[\exp \kappa u^+ - 1 - \kappa u^+ - \frac{(\kappa u^+)^2}{2} - \frac{(\kappa u^+)^3}{6}\right] \tag{B.9}$$

At $z^+ < 5.4$, the laminar sublayer is reached and $z^+ = u^+$.
Given that the free-stream Mach number of the cylindrical cavity flow test cases of section 6.4 is below 0.3, the time-averaged flow-normal velocity component of the turbulent boundary layer is computed by assuming the flow to be incompressible and two dimensional. The time-averaged spanwise velocity component is identical to zero over the flat plate ($v = 0$). The incompressible continuity equation then becomes:

$$\frac{\partial u(x,z)}{\partial x} = -\frac{\partial w(x,z)}{\partial z} \tag{B.10}$$

Equation (B.10) is solved to obtain the mean flow-normal velocity component w of the turbulent boundary layer.

B.2 Turbulent kinetic energy and turbulent dissipation rate

The turbulence intensity profile in the outer region of a fully developed turbulent boundary layer is described by an empirical function f_3 at $z^+ > 150$. The latter is obtained by the interpolation of measurement by Pengyuan & Biondini (2007) at the wind tunnel of the Ente Nazionale per l'Energia e l'Ambiente (Italian national research center for Energy and Environment) (ENEA). Figure B.1 shows the normalized turbulence intensity $u'^{2+} = u'^2/u_\tau^2$ versus the normalized wall distance $z^+ = zu_\tau/\nu$. The data from the ENEA wind tunnel is plotted with the symbols $\diamond$, $\square$, $\triangle$ and $\circ$ over the range $67 \leq z^+ \leq 5000$. The experimental predictions from De Graaff & Eaton (2000) are also shown, covering the wider range $4 \leq z^+ \leq 9000$. Over the common range, the

#	Symbol	Re_θ	Author
1	$\diamond$	4900	ENEA
2	$\circ$	6050	ENEA
3	$\square$	8250	ENEA
4	$\triangle$	8760	ENEA
5	$\times$	5200	De Graaff-Eaton
6	$+$	13000	De Graaff-Eaton
7	$*$	31000	De Graaff-Eaton
f_1	$- \cdot -$	5200	Marusic-Kunkel
f_3	$-$	8760	ENEA

Table B.1: Summary table.

two data sets show a good agreement, with the spread among data sets being due to the variation in Re_θ. In the measurement, the outer boundary layer was traversed, therefore a model for the inner region is used in the simulation. Marusic & Kunkel (2003) proposed an empirical formula (f_1) to evaluate the turbulence intensity in the inner region as a function of Re_θ and z^+.
u'^{2+} is analytically described by:

$$u'^{2+} = \begin{cases} f_1\left(z^+, Re_\theta\right), & z^+ \leq z^+_{inner} \\ f_2\left(z^+, Re_\theta\right), & z^+_{inner} < z^+ < z^+_{outer} \\ f_3\left(z^+, Re_\theta\right), & z^+ \geq z^+_{outer} \end{cases} \tag{B.11}$$

f_2 is a function of Re_θ and z^+ and it is obtained as a gradient-matched cubic curve-fit as proposed by Marusic & Kunkel (2003).
The turbulent kinetic energy and its specific dissipation rate are defined as:

$$\begin{aligned} k &= \frac{3}{2} u'^{2+} u_\tau^2 \\ \omega &= \frac{\rho k}{\mu_t} \end{aligned} \tag{B.12}$$

At the inflow, $\rho = \rho_\infty = 1.225\ kg/m^3$. k and ω are obtaining by equation (B.12) using

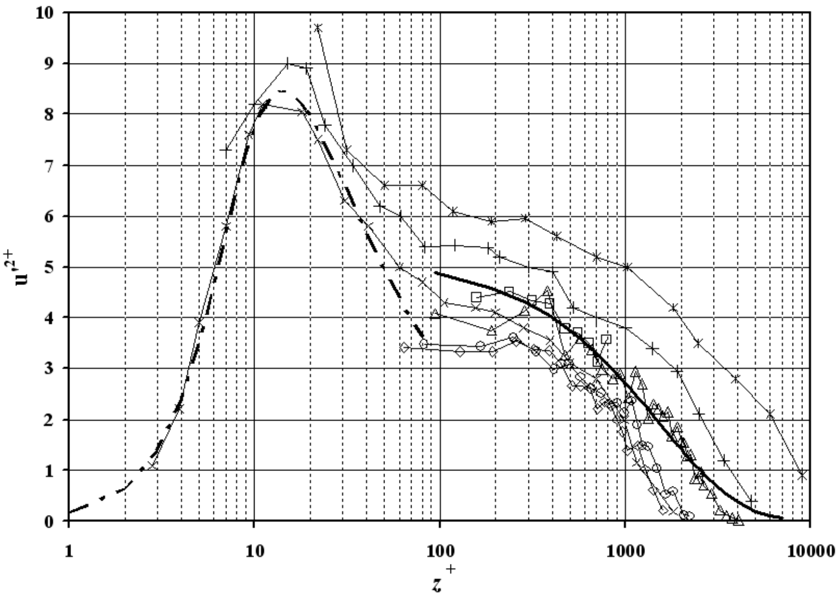

Figure B.1: Normalized turbulent intensity. Symbols and conditions are given in table B.1.

equation (B.11).

References

A , K.K. & M , J. (1995). Effects of cavity dimensions, boundary layer, and temperature on cavity noise with emphasis on benchmark data to validate computational aeroacoustic codes. Tech. Rep. 4653, NASA. 8, 10

A , J.O., K , E.J. & T , A. (2004). A theoretical model for cavity acoustic resonances in subsonic flow. In 10th *AIAA/CEAS Aeroacoustics Conference*, 2004-2845, Manchester, UK. 13

A , S. & S , N. (2003). Hybrid RANS-LES modeling for cavity aeroacoustics predictions. *Int. J. Aeroacoustics*, **2**, 65–93. 22

A , K., K , K., R , S.A. & L , N.J. (2009). Experimental and computational investigation of an open transonic cavity flow. *Proc. IMechE part G: J. Aerospace Engineering*, **223**, 357–368. 11, 12, 23

B , W.P. (2005). *A Time Accurate Computational Analysis of Two-Dimensional Wakes*. Phd thesis, University of Leicester, Leicester, UK. 69

B , A.J. & C , E.E. (1973). Estimation of possible excitation frequencies for shallow rectangular cavities. *AIAA Journal*, **11**, 347–351. 13

B , P.J.W. (1976). Noise response of cavities of varying dimensions at subsonic speeds. TN D-8351, NASA. xi, 7, 8, 10, 13, 14, 105, 117, 128, 129, 130, 133, 135

B , C., B , C. & J , D. (2002). Computation of flow noise using source terms in linearized euler's equations. *AIAA Journal*, **40**, 235–243. 24

B , P., S , J.T. & W , J. (1960). Flow stability in the presence of finite initial disturbances. Tech. Rep. 264, Advisory Group for Aerospace Research and development. 76

B , K.S. & F , F. (1998). An analytical comparison of the acoustic analogy and Kirchhoff formulation for moving surfaces. *AIAA Journal*, **36**, 1379–1386. 135

B ` , G.A. & C , T. (2008). Three-dimensional instabilities in compressible flow over open cavities. *J. Fluid Mechanics*, **599**, 309–339. 23

B , B., C , R., P , D., H , E., D , A., D , D. & R , C. (2007). CFD General Notation System Steering Committee Charter. Tech. rep., NASA Langley. 51

C , J.R. & F , R.A. (1999). *An Engineering Data Book*. Palgrave Macmillan, 2^{nd} edn. 118

C , M., G , M. & R , A. (2006). Towards quieter airframes. In *Aeronautics Days*, Vienna, Austria. 1

C , A.F., R , J.N., D J ., F.G. & H , J.A. (1961). An investigation of separated flows. Part I: The pressure field. *J. Aerospace Sci.*, **28**, 457–470. 8, 22

C , H., H , P.G. & L B , R.P. (2004). Parallel 2D/3D unsteady incompressible viscous flow computations using an unstructured CFD code. In 3^{rd} *International Conference on Computational Fluid Dynamics*, Toronto, Canada. 23

C , W.K. & G , P.Z. (2004). Large eddy simulation of turbulent convective cavity flow. *Int. J. Comp. Fluid Dynamics*, **18**, 641–650. 22

C , D. (1956). The law of the wake in the turbulent boundary layer. *J. Fluid Mech.*, **1**, 191–226. 140, 141

C , T. (2001). An overview of simulation, modeling, and active control of flow/acoustic resonance in open cavities. In 39^{th} *AIAA Aerospace Sciences Meeting & Exhibit*, 2001-0076, Reno, Nevada, USA. 6, 8, 13, 25

C , T. & L , S.K. (2004). Computational aeroacoustics: progress on nonlinear problems of sound generation. *Progress on Aerospace Sciences*, **40**, 365–416. 21, 22, 66, 118, 130

C , T., B , A.J. & R , C.W. (1999). Numerical investigation of the flow past a cavity. In 5^{th} *AIAA/CEAS Aeroacoustics Conference*, 1912, Greater Settle, Washington. 22, 108, 130

C , R., F , K. & L , H. (1928). Über die partiellen differenzengleichungen der mathematischen physik. *Mathematische Annalen*, **100**, 32–74. 49

C , E.E. (1970). An approximate calculation of the onset velocity of cavity oscillations. *AIAA Journal*, **8**, 2189–2194. 13

C -C F , T. (2002). *Hybrid Reynolds-Averaged / Large-Eddy Simulations of Ramped-Cavity and Compression Ramp Flow-fields*. Degree of master of science, Department of Mechanical and Aerospace Engineering, Raleigh, North Carolina. 42

C , D.G. (1975). Boundary conditions for direct computation of aerodynamic sound generation. *Progress on Aerospace Sciences*, **6**, 31–96. 22

C , S., K , R. & D , J. (2007). Aeroacoustics of aircraft cavities. In 16^{th} *Australasian Fluid Mechanics Conference*, Crown Plaza, Gold Coast, Australia. 12

C , M.J., C , J.D., S , R.W., S , M.K. & G , A. (2006). Cavity noise generation for circular and rectangular vent holes. In 12^{th} *AIAA/CEAS Aeroacoustics Conference*, 2508, Cambridge, Massachusetts, USA. 13, 14, 133

D ¨ , S. & D , L. (2003). Hybrid RANS/LES employing interface condition with turbulent structure. In I. Begell House, ed., *Turbulence, Heat and Mass Transfer*, vol. 4, 689–696, K. Hanjalić, Y. Nagano and M. Tummers. 3, 38

D -G , Y., Z -L , F. & X -F , L. (2009). Effect of free-stream boundary-layer thickness on aeroacoustic characteristics of open cavity flow. In 10^{th} *International Conference on Fluid Control, Measurements, and Visualization*, Moscow, Russia. 133

D , W.J. & S , R.L. (1990). Time-dependent and time-averaged turbulence structure near the nose of a wing-body junction. *J. Fluid Mechanics*, **210**, 23–55. 48

D G , D.B. & E , J.K. (2000). Reynolds-number scaling of the flat-plate turbulent boundary layer. *J. Fluid Mechanics*, **422**, 319–346. 141

D F , P. (1997). A new boundary integral formulation for the prediction of the sound radiation. *J. Sound and Vibration*, **202**, 491–509. 135

D , J. & S , E. (2008). An experimental investigation of turbulent boundary layer flow over surface-mounted circular cavities. *Proc. IMechE part G: J. Aerospace Engineering*, **222**, 109–125. viii, 16, 19, 21

D , J., H , T. & S , E. (2006). Turbulent flow over circular cylindrical cavities with varying depth to diameter ratio. In *International Council of the Aeronautical Sciences Congress*, Hamburg, Germany. 9, 21, 77, 90, 117, 132

E -D , M.F.F. (2009). *Analytical and CFD methods investigating shrouded blade tip leakage*. Phd thesis, faculty of science, University of Leicester. 3, 26, 29, 33, 34, 35, 39, 48, 52, 69

E , R. & S ¨ , W. (2004). On the simulation of trailing edge noise with a hybrid LES/APE method. *J. Sound and Vibration*, **270**, 509–524. 24

F , J.L., S , R., C , J.E. & D , W.J. (1993). An experimental study of a turbulent wing-body junction and wake flow. *Experiments in Fluids*, **14**, 366–378. 48

F W , J.E. & H , D.L. (1969). Sound generation by turbulence and surfaces in arbitrary motion. *Proc. Royal Society of London. Series A (Mathematical and Physical Sciences)*, **264**, 321–342. 24, 135

G , L. & W , K.G. (1973). Measurements of the drag of some characteristic aircraft excrescences immersed in turbulent boundary layers. Tech. Memo 1538, Royal Aircraft Establishment, Farnborough, UK. viii, 2, 9, 10, 16, 17, 18, 48, 132

G, M., P, U., M, P. & C, W.H. (1991). A dynamic subgrid-scale eddy viscosity model. *Physics of Fluids A*, **3**, 1760–1765. 136

G, M.B. (1990). Non-reflecting boundary conditions for Euler equation calculation. *AIAA Journal*, **28**, 2050–2058. 30

G, D. (1991). Non-reflective boundary conditions. *J. Comput. Phys.*, **94**, 1–29. 30

G, S.M. (2001). An overview of computational aeroacoustics techniques applied to cavity noise prediction. In 39^{th} *AIAA Aerospace Sciences Meeting and Exhibit*, 2001-510, Reno, Nevada, USA. 13

G, S.M., D, W.G. & W, D.E. (2004). Experimental investigation of the flow characteristics within a shallow wall cavity for both laminar and turbulent upstream boundary layers. *Experiments in Fluids*, **36**, 791–804. 13

G, M. & R, A. (2007a). Noise sources from a cylindrical cavity. In 13^{th} *AIAA/CEAS Aeroacoustics Conference*, 2007-3723, Rome, Italy. 21, 66, 69, 72, 76, 77, 79, 89, 90, 108, 114, 131

G, M. & R, A. (2007b). The role of the inflow momentum thickness in subsonic cylindrical cavity noise generation. In 14^{th} *International Congress on Sound and Vibration*, 165, Cairns, Australia. 21, 69, 70, 84, 131

G, M. & R, A. (2008a). Detached eddy simulation of subsonic cylindrical cavity flow. In S. Monfardini, ed., *Science and Supercomputing in Europe - Report 2008*, chap. Engineering, 364–369, Monograf s.r.l. 134

G, M. & R, A. (2008b). The radiating pressure field of a turbulent cylindrical cavity flow. In 14^{th} *AIAA/CEAS Aeroacoustics Conference*, 2008-2852, Vancouver, Canada. 94, 131

H, T. (2008). Benchmarking the cgns i/o performance. In 46^{th} *AIAA Aerospace Sciences Meeting and Exhibit*, 2008-479, 1–8, Reno, Nevada, USA. 52

H, L.S., T, A.K. & S, P.R. (2002). Detached-eddy simulation over a simplified landing gear. *J. Fluids Engineering*, **124**, 413–24. 22

H , H.H. & B , D.B. (1975). The physical mechanism of flow-induced pressure fluctuations in cavities and concepts for their suppression. In 2nd *AIAA AeroAcoustics Conference*, Hampton, Virginia, USA. 13

H , H.H., H , D.G. & C , E.E. (1971). Flow-induced pressure oscillations in shallow cavities. *J. Sound Vibration*, **18**, 545–545. 11, 13

H , H.L.F. (1895). *On the Sensations of Tone as a Physiological Basis for the Theory of Music*. Aberdeen University Press, 2nd edn., translated by A.J. Ellis. 14

H , T., D , J. & S , E. (2006). Experimental verification of CFD modeling of turbulent flow over circular cavities. In *Canadian Society of Mechanical Engineering Forum*, Kananaskis, Canada. 2, 21, 77, 90, 117

H , C. (1988). *Numerical Computation of INTERAL AND EXTERNAL FLOWS, Vol 2: Computational Methods for Inviscid Flows*, vol. 2. John Wiley and Sons Ltd. 28, 33

H , M., M , I., K , M. & K , T. (1983). Some characteristics of flow pattern and heat transfer past a circular cylindrical cavity. *JSME Bulletin*, **26**, 1744–1752. viii, 2, 9, 16, 19, 20

H , A.S. (1953). *Principle of numerical analysis*. International series in pure and applied mathematics, McGraw-Hill, London. 45

H , M.S. (1997). Edge, cavity and aperture tones at very low mach numbers. *J. Fluid Mechanics*, **330**, 61–84. 13

H , F.Q. (2004). Absorbing boundary conditions. *Int. J. Computational Fluid Dynamics*, **18**, 513–522. 30

ICAO (2002). *Environmental Protection: Aircraft noise*, vol. 1 of *Annex 16*. International Civil Aircraft Organization, Montréal, 4th edn. 135

ICAO (2004). *Environmental technical manual on the use of procedures in the noise certification of aircraft*. International Civil Aircraft Organization, 999 University Street Montréal, Quebec H3C 5H7, Canada, 3rd edn., doc 9501-AN/929. 135

K , A., D P , G. & P , U. (2006). Interface conditions for hybrid RANS/LES calculations. *Int. J. Heat and Fluid Flow*, **27**, 777–788. 50

K , A.N. (1991). The local structure of turbulence in incompressible viscous fluid for very large reynolds numbers. *Proc. Royal Society London Series A (Mathematical and Physical Sciences)*, **434**, 9–13. 126

L , A.M. & C , N. (1999). Control of cavity resonance using steady and oscillatory blowing. Tech. Rep. NAG1-1829, NASA Langley Research Center. 93

L , Z. & H , A. (2008). Effect of sidewall boundary conditions on unsteady high speed cavity flow and acoustics. *Computers & Fluids*, **37**, 584–592. 22

L , M.J. (1961). Review of computational aeroacoustics algorithms. *Proc. Royal Society of London. Series A (Mathematical and Physical Sciences)*, **267**, 147–182. 27

L , D.K. (1966). On the application of the eddy viscosity concept in the inertial sub-range of turbulence. Manuscript 123, National Center Atmospheric Research, Boulder, Colorado, USA. 136

L , D.K. (1992). A proposed modification of the Germano subgrid-scale closure method. *Physics of Fluids A*, **4**, 633–635. 136

L , Y., T , P.G. & K , R.M. (2008). Linear and nonlinear model large-eddy simulations of a plane jet. *Computers & Fluids*, **37**, 439–449. 37

L¨ , R. (2001). *Applied Computational Fluid Dynamics Techniques: An Introduction Based on Finite Element Methods*. John Wiley and Sons Ltd, 2nd edn. 65, 67

L , L.N., M , P.J. & A , A. (2004). A review of parallel computing in computational aeroacoustics. *Int. J. Computational Fluid Dynamics*, **18**, 493–502. 23

M , M. (1992). *A three dimensional high resolution compressible flow solver*. Phd thesis, faculty of applied science, Université Catholique de Louvain. 29

M , O., J , E., S , P., B , C., B , C. & J ´, D. (2008). Investigation of flow features and acoustic radiation of a round cavity. In 14th *AIAA/CEAS Aeroacoustics Conference*, 2008-2851, Vancouver, Canada. 14, 19, 133

M , I. & K , G.J. (2003). Streamwise turbulence intensity formulation for flat-plate boundary layer. *Physics of Fluids*, **15**, 2461–64. 94, 142

M , D.J. & E , L.F. (1963). Three-dimensional flow in cavities. *J. Fluid Mechanics*, **16**, 620–632. 10

M P , A.L. (1993). Evaluation of advances in engine noise technology. *Aircraft Engineering & Aerospace Technology: An International Journal*, **42**, 16–22. 1

M , F.R. (1992). Improved two equation $k-\omega$ turbulence models for aerodynamic flows. Tech. Memo 103975, NASA Ames Research Center, California. 3, 39, 44, 46, 123

M , M. & R , A. (2009). Regressing the size and cost of turbulent cavity flow simulations, under consideration for pubblication on Journal of Algorithms & Computational Technology. 136

N , Y., Y , I. & I , S. (1960). On the acoustic radiation from a flanged circular pipe. *J. Physical Society Japan*, **15**, 510–517. 14

N , A.N. & S , I.C. (1989). Acoustic radiation from a circular pipe with an infinite flange. *J. Sound Vibration*, **135**, 85–93. 14

Ö , J.M. (1999). *Experimental studies of zero pressure-gradient turbulent boundary layer flow*. Phd thesis, Royal Inst. Techn., KTM, Stockholm. 45

P , Y. & B , L. (2007). Turbulent boundary layer characterization at the ENEA wind tunnel. Technical report, Università degli studi of Roma Tre. 71, 141

P , U., S , C.L. & S , S. (1997). On the computation of sound by large-eddy simulations. *J. Eng. Math.*, **32**, 217–236. 22

P , E.B., S , R.L. & T , M.B. (1993). Experimental cavity pressure measurements at subsonic and transonic speeds. Tech. Paper TP-3358, NASA Langley, Hampton, Virginia, USA. 11

P , A. (1964). Theory of vortex sound. *J. Acoustical Society of America*, **36**, 177–195. 79, 106, 110

R , J.W.S. (1894). *The theory of sound*. Macmillan, London, 2^{nd} edn. 14, 15, 105, 130, 133

R , D. & N , E. (1978). Review on self-sustaining oscillations of flow past cavities. *Transactions of ASME. J. Fluids Engineering*, **100**, 152–165. 11, 13

R , P.L. (1981). Approximate riemann solvers, parameter vectors and difference schemes. *J. Comput. Phys.*, **43**, 357–372. 3, 28

R , W.D., D , W., B , M. & S , P. (2004). On the prediction of near-field cavity flow noise using different caa techniques. In *International conference of noise and vibration engineering: ISMA Conference*, 369–388, Leuven, Belgium. 6, 9, 25

R , A. (2006). Self-excited supersonic cavity flow instabilities as aerodynamic noise sources. *Int. J. Aeroacoustics*, **5**, 335–360. 22, 117

R , A. (2007). The acoustic resonance of rectangular and cylindrical cavities. *J. Algorithms & Computational Technology*, **1**, 329–355. 14, 15, 81

R , A. & B , E.J. (2002). Injection parameters for an effective passive control of the cavity flow instability. In 40^{th} *AIAA Aerospace Sciences Meeting & Exhibit*, Reno, Nevada, USA. 46

R , A., G , M., M , M., A , C. & G , T. (2009). Generation of a turbulent boundary layer inflow for RANS simulations. In 15^{th} *AIAA/CEAS Aeroacoustics Conference*, 2009-3272, Miami, Florida, USA. 72, 94, 141

R , J.E. (1964). Wind-tunnel experiments on the flow over rectangular cavities at subsonic and transonic speeds. Tech. Rep. 3438, Aeronautical Research Council Reports and Memoranda. 12, 13, 14, 21, 130

R , C.W. & W , D.R. (2006). Dynamics and control of high-reynolds-number flow over open cavities. *Annual Rev. Fluid Mechanics*, **38**, 251–276. 13

R , C.W., C , T. & B , A.J. (2002). On self-sustained oscillations in two-dimensional compressible flow over rectangular cavities. *J. Fluid Mechanics*, **455**, 315–346. 22, 108, 130

S , M., D , M., C , E., M , J., L , J., Ö , H., E , M.O., Y , P., Y , X., D B , J., M , J.H. & C , R.C. (2004). Exploring strategies for closed-loop cavity flow control. In 42^{nd} *AIAA Aerospace Sciences Meeting and Exhibit*, 2004-0576, Reno, Nevada, USA. 13

S , V. (1977). Experimental investigation of oscillations in flows over shallow cavities. *AIAA Journal*, **15**, 984–991. 11

S , H. (1968). *Boundary layer theory*. McGraw-Hill, London, 6^{th} edn. 46

S ¨ , W. & E , R. (2005). Some concepts of LES-CAA coupling. In W. Huttl & Delfs, eds., *LES for Acoustics*, Cambridge Aerospace, Cambridge University Press. 22, 24

S , C., S , P., B , C. & J ´, D. (2001). On the radiated noise computed by large-eddy simulation. *Physics of Fluids*, **13**, 476–487. 22

S , M.L., S , P.R., S , M.K. & T , A.K. (2003). Towards the prediction of noise from jet engines. *Int. J. Heat and Fluid Flow*, **24**, 551–561. 67

S , B.A. & G , Y. (2004). Development of computational aeroacoustics tools for airframe noise calculations. *Int. J. Computational Fluid Dynamics*, **18**, 455–469. 22

S , J. (1963). General circulation experiments with the primitive equations. I. the basic experiment. *Monthly Weather Review*, **91**, 99–164. 136

S , P.R. (2000). Strategies for turbulence modelling and simulations. *Int. J. Heat & Fluid Flow*, **21**, 252–263. 22

S , D.B. (1961). A single formula for the law of the wall. *Transactions of ASME, J. Appl. Mech.*, **28**, 444–458. 45

S , I. & R , A. (2007). A selective overview of high-order finite difference schemes for aeroacoustic applications. In 14^{th} *International Conference on Sound and Vibration*, 432, Cairns, Australia. 136

S , I., R , A. & G , H.M. (2009). Towards a monotonicity-preserving inviscid wall boundary condition for aeroacoustics. In 15^{th} *AIAA/CEAS Aeroacoustics Conference*, Miami, Florida, USA. 136

S J ., R.L. & W J ., F. (1987). Experimental cavity pressure distributions at supersonic speeds. Tech. Paper 2683, NASA Langley, Research Centre Hampton, Virginia, USA. 11, 12

S , P.K. (1984). High resolution schemes using flux limiters for hyperbolic conservative laws. *SIAM Journal of Numerical Analysis*, **21**, 995–1011. 29

T , C.K.W. (2004). Computational aeroacoustics: an overview of computational challenges and applications. *Int. J. Computational Fluid Dynamics*, **18**, 547–567. 22

T , C.K.W. & B , P.J.W. (1978). On the tones and pressure oscillations induced by flow over rectangular cavities. *J. Fluid Mechanics*, **89**, 373–399. 13, 130

T , E.F. (1999). *Riemann solvers and numerical methods for fluid dynamics: A practical introduction*. Springer, Berlin, 2^{nd} edn. 33

T , A.A. (1976). *The Structure of Turbulent Shear Flow*. Cambridge University Press, Cambridge, U.K., 2^{nd} edn. 37

V , A.D. & G , C. (1991). Control of cavity flow by upstream mass injection. In 22^{nd} *Fluid Dynamics, Plasma Dynamics and Lasers AIAA Conference*, Honolulu, HI. 93

V L , B., T , J.L., R , P.L. & N , R.W. (1987). A comparison of numerical flux formulas for Euler and Navier-Stokes equation. In 8^{th} *AIAA Computational Fluid Dynamics Conference*, 87-1104, 36–41. 3, 28

V , F.R., G , A., C , R. & G , M. (2009). Experimental investigation of a cylindrical cavity. In 15^{th} *AIAA/CEAS Aeroacoustics Conference*, 2009-3207, Miami, Florida, USA. 71, 95, 126, 132, 133

V , M.R. & G , D.V. (1999). High-order accurate methods for unsteady vortical ows on curvilinear meshes. *AIAA Journal*, **37**, 1231–1239. 136

V , M.R. & R , P. (2002). Large-eddy simulation on curvilinear grids using compact differencing and filtering schemes. *Transactions of ASME, J. Fluids Engineering*, **124**, 836–847. 136

V K´ ´ , T. (1954). *Aerodynamics: selected topics in the light of their historical development*. Cornell U. Press, Ithaca, NY. 47

W , M., F , J.B. & L , S.K. (2004). Computational prediction of flow-generated sound. *Annual Review of Fluid Mechanics*, **38**, 483–512. 9, 22

W , F.M. (1991). *Viscous fluid flow*. McGraw-Hill Series in Mechanical Engineering, 2*nd* edn. 94, 137, 141

W , D.C. (2002). *Turbulence modeling for CFD*. DCW Industries, 2*nd* edn. 38, 39, 46

Y , H., C , R.K. & R , S. (2004). Numerical simulation of incompressible laminar flow over three-dimensional rectangular cavities. *J. Fluids Engineering*, **126**, 919–927. 108

Y , A. (1986). Statistical theory for compressible shear flows with the application of subgrid modelling. *Physics of Fluids A*, **29**, 2152–2163. 3, 36, 38, 123, 136

Y , D., M , R., W , M. & M , P. (2006). Analysis of stability and accuracy of finite-difference schemes on a skewed mesh. *J. Comp. Physics*, **213**, 184–204. 69